CONFIGURATION OF MICROGRIDS CONSIDERING STATE ESTIMATION, SERVICE RESTORATION, AND INTEGRATION WITH NATURAL GAS SYSTEMS

MOHAMED ZAKI ABDELHAMED MOHAMED

A DISSERTATION SUBMITTED TO
THE FACULTY OF GRADUATE STUDIES
IN PARTIAL FULFILMENT OF THE REQUIREMENTS
FOR THE DEGREE OF
DOCTOR OF PHILOSOPHY

GRADUATE PROGRAM IN ELECTRICAL ENGINEERING AND
COMPUTER SCIENCE
YORK UNIVERSITY
TORONTO, ONTARIO

OCTOBER 2019

Abstract

The interest in the adoption of smart grid technologies as a means for digitalization and automation of power distribution systems has increased rapidly in the last few years. This interest can be explained by the common belief that smart grid technologies greatly enhance the system reliability, power quality, overall efficiency, and most importantly the accommodation of distributed generations (DGs). As DG penetration levels increase, distribution networks are divided into a new set of management layers based on a microgrid structure. A typical microgrid is formed of a cluster of DG units feeding a group of loads that operates in parallel to or isolated from the main grid. Microgrids are the building blocks of smart distribution grids (SDG). The concept of microgrid brings numerous benefits; among which, the improvement of system reliability is the most salient. However, the realization of such benefit is strongly dependent on the implementation of appropriate design and operation methodologies that take into account the special philosophy and operational characteristics of microgrids.

Accordingly, this thesis introduces new methodologies to enhance the operation and reliability of SDGs clustered into microgrids. In particular, three main functions are dealt with in this research work: optimum configuration, self-healing restoration, and the integration between power and natural gas microgrids. First, an optimal zone clustering (i.e. configuration) algorithm is proposed for dynamic state estimation in islanded microgrids (IMG) considering the supply adequacy of each zone. Second, a centralized-based optimization model with multi-objective functions is formulated to perform the service restoration process for microgrids operating in both grid-connected and islanded modes of operation. Further, to obviate the need for a central unit and reduce the problem complexity, the optimization problem is reformulated using distributed automated agents. Third, a new model is proposed for optimal scheduling of power-to-gas (PtG), gas-fired generation (GfG), and gas storage units in a multi-carrier energy system (MCES)-based microgrid. The model aims to facilitate the integration of renewable DGs, utilize gas and power price arbitrage, provide regulation services to the real-time market, and contribute to the restoration of power and gas loads during unplanned outages.

Dedicated to:

My beloved parents in heaven, and to my dear wife and kids.

I hope you are proud of me

Acknowledgements

All praise to Allah, the almighty, the most gracious and the most merciful, whose countless bounties enabled me to accomplish this thesis successfully. Alhamdulillah.

I would like to express my sincerest gratitude to my supervisor **Prof. Hany Farag** for his professional guidance, valuable advice, continual support and encouragement. My favorite part of this whole process will always be sitting in your office during our weekly meetings. I had some difficulties during my research period but you never gave up on me, and I'll always remember that. Your endless patience, good faith and work ethic always inspired me to put my head down and keep working harder everyday. Thank you for giving me your time and knowledge. You are more than a supervisor to me, never came to you and let me down. I hope I have honored your support and knowledge and made you proud.

My appreciation and thanks are also extended to my PhD committee members: **Prof. John Lam** and **Prof. Ebrahim Zadeh**, for their patience and guidance during the research period, your valuable questions and concerns in our meetings added a lot to this thesis. This contribution of yours is something I will always value forever.

I wish also to thank my parents in heaven; **Dr. Zaki El-Sharafy** and **Dr. Hanaa Abduallah**, who share credit in every goal I achieved or may achieve in my life. You taught me so much over the years, but the number one thing you've taught me is how to respond to challenges. To always give it my best, no matter what the circumstances. To always fight hard no matter what I am up against. Most importantly, to do so with respect and honor. I will never forget how hard you worked for me and believed in me. Hoping that I'm making you proud all the way up there in heaven.

My deep appreciation and thanks to my wife **Reham Farouk**, I would be nowhere without your relentless positive energy, understanding, patience, encouragement, optimism, and support. Thank you for sacrificing so much for all of us - you work so hard, keep our lives organized and give us everything you have. Specially with our beloved kids **Talia** and **Yussif** who added lots of joy and meaning to our life.

I would really like to take time to appreciate and acknowledge my colleagues in Lassonde school of engineering at York University. Special thanks to **Nader Eltaweel**, **Abduallah Alobaidi**, **Abdullah Sawas**, **Shivam Saxena**, and **Sanjida Moury**. As well as my friends especially **Omar Eldeeb**, **Abdelaal Brothers**, **Ahmed Fergala**, **Ahmed Alsayed**, and **Moomen Soliman**.

Table of Contents

List of Figures

Abbreviations

ACO	Ant Colony Optimization
CIC	Cost of Customer Interruption
DG	Distributed Generation
DGT	Distributed Generation Transfer
DNO	Distribution Network Operator
DOR	Distributed Optimal Reconfiguration
DPF	Distributed Particle Filter
DQ	Direct and Quadrature Frames
DSAA	Distributed Supply Adequacy Assessment
DSE	Distributed State Estimation
EMS	Energy Management System
FIPA	Foundation for Intelligent Physical Agent
GfG	Gas Fired Generator
IID	Island Interconnection Device
IMG	Islanded Microgrid
LOG	Level of Gas

LT	Load Transfer
MAS	Multi–agent System
MC	Monte–Carlo Simulation
MCES	Multi–Carrier Energy System
μA	Microgrid Control Agent
NO	Normally Open Switch
ODE	Ordinary Differential Equation
OPTAPO	Optimal Asynchronous Partial Overlay
PCC	Point of Common Coupling
PMU	Phasor Measurement Unit
PtG	Power to Gas
RMSE	Root–Mean Square Error
RTU	Remote Terminal Units
$\mathrm{RTCI}^{\mathrm{GfG}}$	Contribution Index of GfG in Real–time
$\mathrm{RTCI}^{\mathrm{PtG}}$	Contribution Index of PtG in Real–time
SDG	Smart Distribution Grid
SNR	Signal to Noise Ratio
$\mathrm{SRCI}^{\mathrm{GfG}}$	Contribution Index of PtG in Service Restoration
$\mathrm{SRCI}^{\mathrm{PtG}}$	Contribution Index of PtG in Service Restoration
VSI	Voltage Source Inverters
ZSE	Zone State Estimator

Chapter 1 - Literature Survey and Thesis Overview

1.1 Legacy of Conventional Power Systems

Figure 1.1 shows the conventional structure of power systems from generation to loads, where sub-transmission systems represent the portion that connects the high voltage transmission systems to the distribution system. When power demands from different types of loads (i.e., residential, commercial, and industrial) are projected to increase, new centralized generation plants in conjunction with expansion in bulk transmission systems are installed to meet the expected load growth. Given that most of the generation plants are fossil fuel based, such conventional mechanism for meeting the growth in power demand is facing serious challenges as many countries are setting initiatives and aggressive targets to reduce their greenhouse gas emissions from the electricity sector.

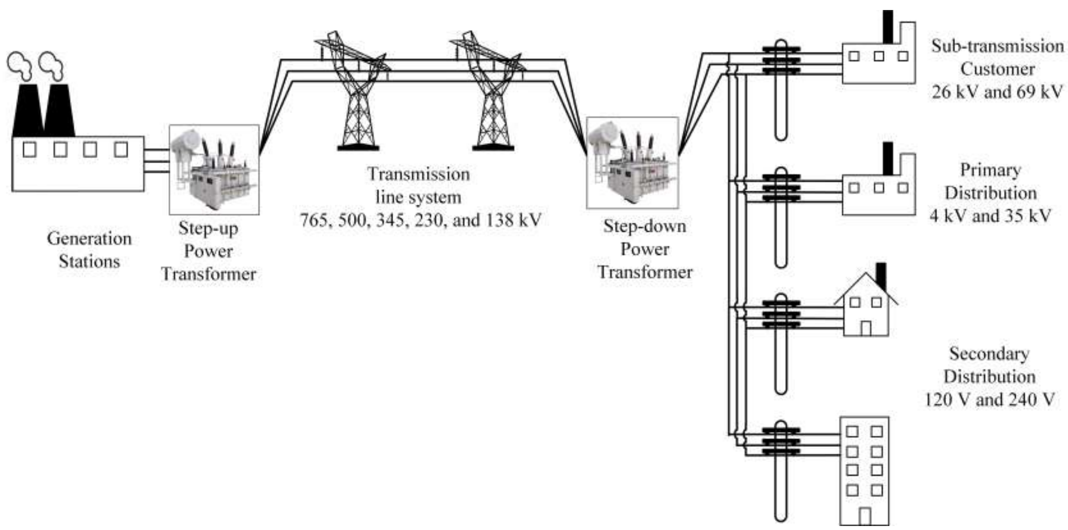

Figure 1.1: Legacy of Power Network Structure

Typical power system structure consists of the following basic subsystems:

- Generation subsystem: 1kV-30 kV
- Transmission subsystem:
  - Extra high voltage Transmission: 500kV-765kV
  - High voltage Transmission: 230kV-345kV
  - Sub-transmission system: 69kV-169kV
- Distribution subsystem

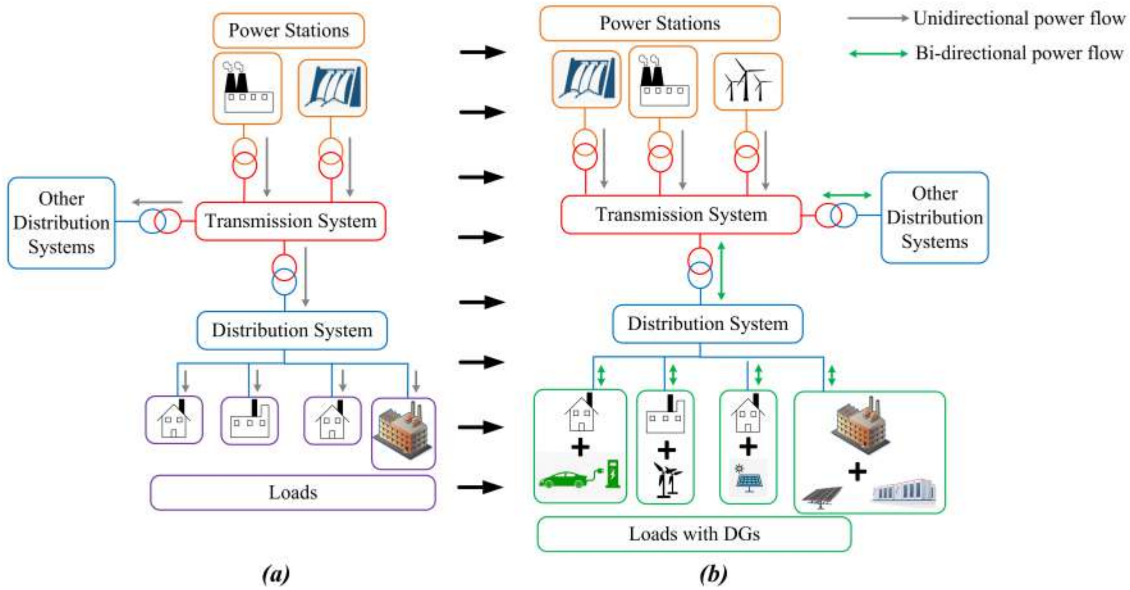

Figure 1.2: Schematic diagram for the evolution of conventional power grid to active power grids. a) Conventional distribution system, b) Active distribution system.

1.2 Distributed Energy Resources

Over the past few years, the interest in the integration of distributed energy resources into power distribution systems has increased rapidly [1]. The integration of these resources has changed the legacy of power distribution networks from being conventional with unidirectional power flow (i.e., from substations to customers) towards active networks with multi–directional power flow. Figure 1.2 shows a comparison in the power flow direction between conventional and active distribution networks. These resources can be classified as distributed generations (DG)s, battery storage, and electric vehicles (EV)s.

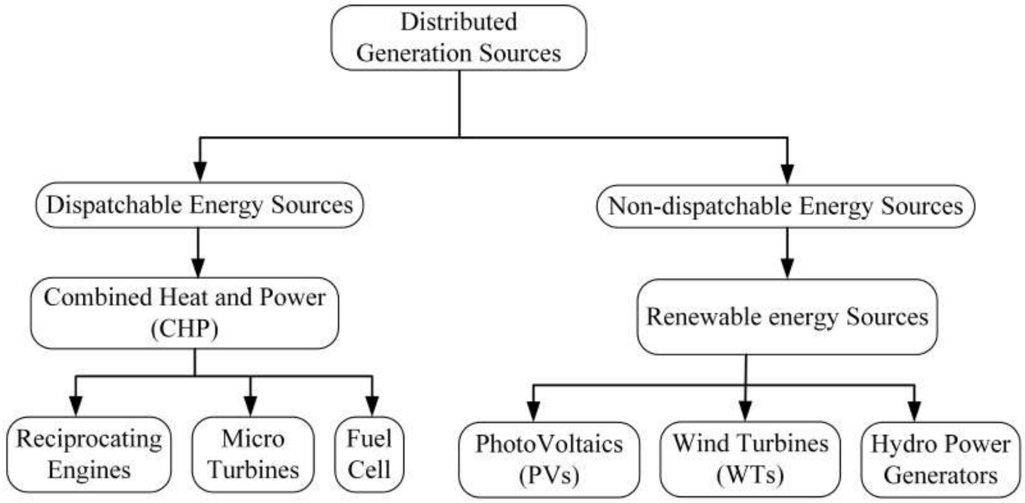

Figure 1.3: Types of dispatchable and renewable DGs and energy storage devices

1.2.1 Integration of Distributed Generations (DGs)

DG can be defined as small-scale electricity generation fuelled mainly by renewable energy sources (i.e. wind and solar), or by low-emission energy sources (i.e., fuel cells and micro-turbines). DG units are typically connected parallel to the utility grid, and are mostly situated in close proximity to the load.

The research disclosed two main types of DG sources that are used in distribution systems: dispatchable and non–dispatchable, as shown in Fig. 1.3. Dispatchable generation is defined and not limited to Combined Heat and Power (CHP): These are power plants which can generate electricity as a primary product and also generate heat as a secondary product, and vice versa. Many DG technologies, such as reciprocating engines, micro-turbines and fuel cells can be used as CHP plants. While the most popular non–dispatchable DG types can be classified as wind turbines, photovoltaic systems, and hydro power generators.

IEEE [2] defined DG as "the generation of electricity by facilities that are sufficiently smaller than central generating plants so as to allow interconnection at nearly any point in a power system." IEEE compared the size of the DG to that of a conventional generating plant. Another definition is provided by the International Council on Large Electric Systems (CIGRE): "all generation units with a maximum capacity of 50 MW to 100 MW, that are usually connected to the distribution network and that are neither centrally planned, nor dispatched." The interconnection of additional DG units with distribution systems is motivated by several factors, such as the continuous growth in electricity demand. In addition, DG units are located closer to load centres; hence, transmission and distribution losses are reduced. From the environmental point of view, there is a strong need for integrating more renewable energy sources in power systems because these renewable sources are inexhaustible and non-polluting. In [3] the advantages of installing a DG in distribution systems are discussed. With the continuous proliferation of DGs, power systems are undergoing significant restructure from centralized to decentralized [4].

1.2.2 Integration of Energy Storage in distribution grids

The forecast for power production of all renewable DGs is challenging because their natural behavior needs to be considered. DGs are going to be connected into grid locations and their generated power could be sold in a competitive market, based on prespecified guidelines and contracts, which are settled in advance. This means that a DG owner should know how much power its DG is capable of producing during every hour of the following day. Storage is then required to compensate for this fluctuating output power. Based on the literature, the main types of utility-scale energy storage devices used are found in [5, 6, 7, 8] and depicted in Fig. 1.4.

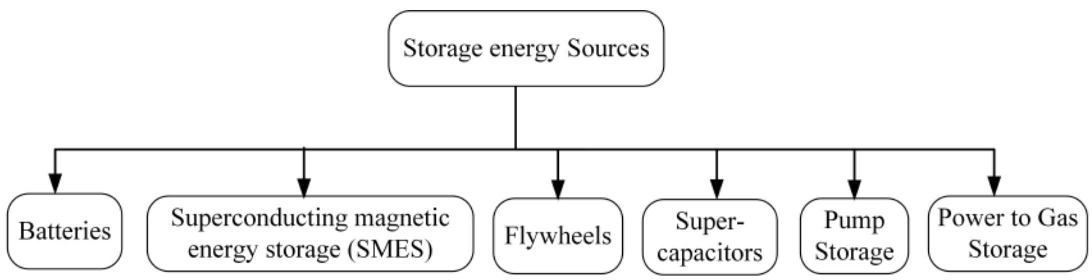

Figure 1.4: Types of energy storage devices

1.3 Challenges Facing the Integration of Distributed Energy Resources

The insertion of distributed energy resource units into power distribution systems has changed the way their are designed and operated. In particular, there are several technical challenges accompany the integration of DG units into distribution systems. Examples of these challenges include but not limited to: the steady-state voltage rise, the complexity of the protection system in the presence of DG units (i.e., the increased short circuit fault current and coordination), voltage flicker due to variable power output from non–dispatchable sources, and reverse power flow. For example, with respect to faults, several utility interconnection standards mandate the disconnection of DG units once a fault is detected [9]. Such disconnection is performed primarily in order to nullify the effects of the DG units on protection practices and to restore the typical system topology. However, with a high penetration level of DG units, the utility system cannot operate effectively with respect to overload, power adequacy, and voltage level, without the support of the DG units' capacity. Therefore, the automatic disconnection of the DG units during faults drastically reduces the expected benefits associated with DG units (i.e., maintaining power quality and reliability, improving system security, and providing a variety of ancillary services) [10].

1.4 Evolution towards Smart Distribution Grids

Smart distribution grids (SDG) have been recently introduced in order to enhance the operation practices of power distribution systems, facilitate seamless integration for high DG penetration levels, and increase the interaction between customers and power utilities. Operation practices include but are not limited to a higher reliability for the system, enhancing the system state estimation, outage management process during abnormal conditions, and minimization of the overall system losses and the total cost [11]. Under SDG paradigm, many utility owned devices (e.g., substations, voltage regulators, shunt capacitors, and reclosers) will be fully coordinated with controllable loads, smart inverters of DGs, and energy storage devices via appropriate information and operation technology platforms. As such, distribution network operators (DNOs) will be able to autonomously control the system under different operating conditions.

Realization issues of SDGs can be categorized as procedural and technical [12]. Procedural issues range from the complexity of the SDG to unified SDG standards. Furthermore, SDG implementation has to be gradual. The fully automated power grid, including every customer and node, is the trend for future electric systems, as presented in the "Grid 2030" vision [13]. A realization of this vision requires the ability to respond to any disturbance in the system with a minimization of impacts, and this will lead to the self–healing ability of the SDG [14, 15]. In addition, SDG has to undertake continuous analysis in order to predict the possibility of any problem, and then take the appropriate action [16]. Advanced information and communication technologies motivate the search for appropriate process to achieve the objective of the self–healing, which means an accurate detection and isolation of the fault and restoration of as many parts of the affected network as possible

[17]. This process requires an advanced intelligence, via modern technologies, that can collect data, execute decision support algorithms, limit interruptions, and dynamically control the flow of the power to overcome problems caused by storms, catastrophes, or human error [18]. Integrating advanced metering infrastructure will add values to the monitoring and diagnostic capability of the self–healing systems. Deploying a large number of smart metering, however, imposes the challenge of managing large amounts of data, which, in turn, leads to storage capacity issues, increased data transfer bandwidth requirements, and cyber security challenges [12].

1.4.1 Control Schemes in SDG

There are three main schemes that have been reported in the literature to manage the operation of SDGs: centralized, distributed through local controllers, and distributed through system partition [15, 19]. Details of the three control schemes can be found in [20, 21, 17]. Figure 1.5 shows the difference between centralized and distributed control schemes in SDG. A brief summary of the advantages and disadvantages of the these control schemes is given here under.

1.4.1.1 Centralized Control in SDG:

In the centralized scheme, a single control unit collects all system measurements, estimates the system state, and then executes a built–in optimization model to

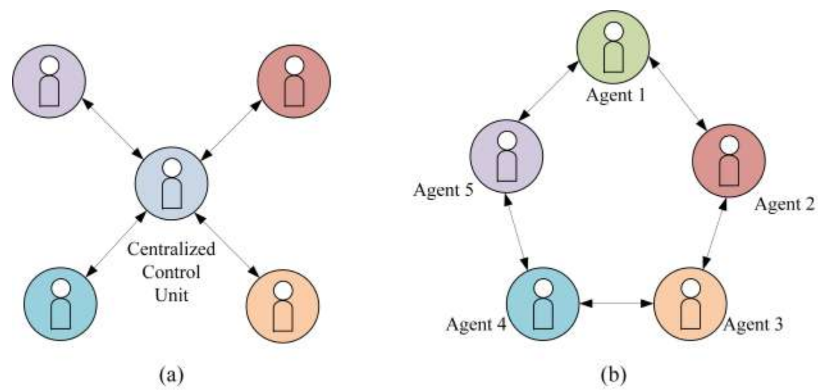

Figure 1.5: Different SDG control schemes; (a) Centralized, (b) Distributed.

determine the optimal settings for the controlled devices [4, 1]. The main advantage of this control is that it may achieve the best solution to the optimization problem, especially for small–scale systems. It has been noted, however, that SDGs are faced with a high degree of complexity and uncertainty due to emerging factors, such as variable power generation from wind and solar, charging of electric vehicles, an increase in the adoption of different energy storage devices, variable demand, and demand response programs. Therefore, implementing centralized control in SDGs will be challenging due to the exponential increase of size of the system, and the large amount of data to be collected and processed by the centralized control unit. In addition, centralized control schemes are subjected to a single point of failure risk, where the failure of the control centre may cause a system collapse [20].

1.4.1.2 Distributed Through Local Controllers:

This approach is based on direct peer–to–peer communication between the controllable devices in the system (i.e., substations, regulators, capacitors, and smart inverters) [21, 17]. Where local data is acquired via local sensors and remote data is acquired via communication with other adjacent controllers. In this case, the local device controllers (e.g., smart inverters) processes the data locally without supervisory control. An example is the peer–to–peer control between adjacent substations during an outage. Where each substation is responsible for controlling and analyzing its own distribution feeders. Each substation exchanges information with neighboring substations to reconfigure the network after clearing the fault(s) [22], This control scheme can be also achieved among control agents in one feeder (e.g., DGs, voltage regulators, and shunt capacitors) [23] to achieve various objectives such as voltage regulation.

1.4.1.3 Distributed Through System Partition:

This control scheme is more popular for distribution networks that can be clustered into sub–systems (referred to as zones or microgrids). Each sub-system has a supervisory control unit that manages the operation of a group of controllable devices (e.g., loads and DGs) using master–slave. Each sub–system has its own local objective and operation constrains. The sub–system control units communicate with each other via two–ways communication. A distributed optimization algorithm is implemented among the sub–system controllers to ensure that these controllers will reach a consensus and satisfy the overall system requirements.

In previous works, distributed control schemes in SDGs are collectively introduced as multiagent systems [20, 24]. Multi–agent systems are composed of multiple interacting computing elements, known as agents. These agents react to changes in the environment and are also capable of acting to achieve specific local goals. Multi–agent is, therefore, a platform of distributed processing, parallel operations and autonomous solving. Coordination among the processors is done using two–way communication, where the timing and contents of the messages among processors are chosen by the system operator, which varies according to the task. In consistency with the literature, distributed control schemes will be referred to as "multi–agent" throughout this thesis. The main features of multi-agent systems are:

- No one agent houses all the information about the whole system.
- Agents make decisions based on local information.
- Failure of an agent to operate do not cause the entire system algorithm to fail.

Based on the above features, multi–agent control schemes have the following advantages over centralized ones [24, 25]:

- Performance/cost ratio: Using multiple inexpensive machines provides a better performance/cost ratio versus using one expensive "super" machine.
- Multi-agent systems provide enhanced reliability (no single point of failure) [26]. If one agent fails, the whole system will survive, albeit with reduced performance.
- Incremental expansion is possible; this increases the modularity of the system.
- Reduction of the complex communication system of the centralized control to cover long distance areas.
- Distribute the large number of tasks over a number of agents, which prevents the overloading of a centralized controller.

On the other hand, centralized control schemes have the following advantages over multi-agent systems:

- Coordination among distributed machines requires appropriate exchange of messages in order to reach a consensus.
- Cyber security of data in distributed algorithms can be problematic.

1.4.2 Microgrids

Microgrids can be formed in electric power systems that have sufficient distributed energy resources to supply the local demand. Intentionally planned microgrids are capable of operating in both grid-connected and islanded modes of operation. To that end, each predefined microgrid has an island interconnection device (IID) that allows the microgrid to switch back and forth between the two modes of operation [27]. Figure 1.6 shows an example of a SDG clustered into four microgrids adjacent to each other through normally open (NO) tie lines. Microgrids offer multiple potential benefits to power utilities and their customers. Among these benefits, the most salient are [28]:

- Improvement of customer reliability, by supplying an islanded area of loads.
- Reduction of the overloading by dividing the system into small systems.
- Isolation of an area in the event of power quality problem occurrence.
- Allowing ease of system maintenance, while providing service to other, isolated microgrids.

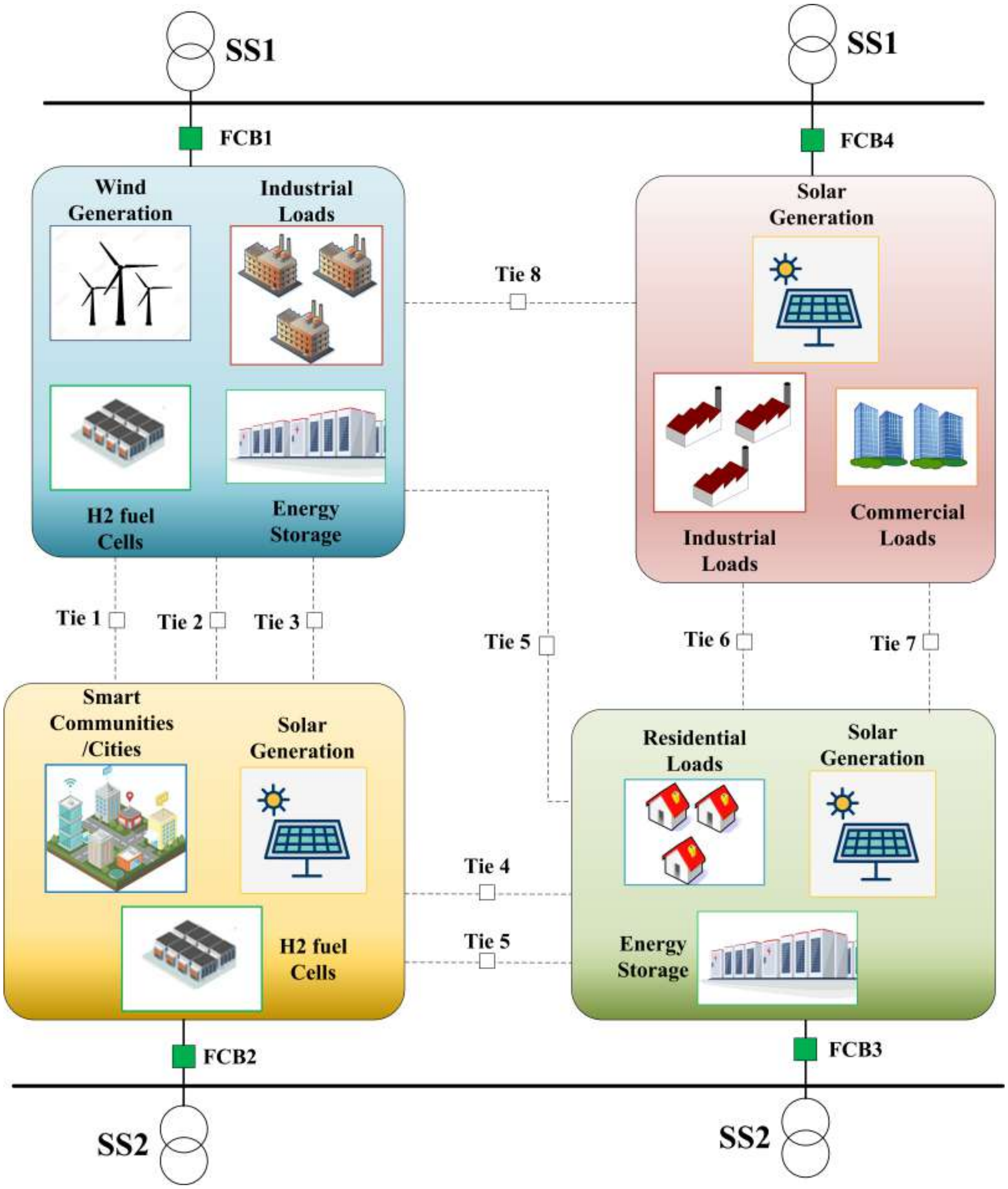

Figure 1.6: SDG clustered into four microgrids

In grid–connected mode, DGs operate in constant power mode, while the main grid holds the system frequency and regulates the substation voltage. In particular, the main grid is defined as the slack bus to maintain the power balance in the microgrid (i.e., the main grid supplies any shortage of power in the microgrid and/or absorbs the surplus power).

In islanded microgrids (IMGs), the absence of the slack bus presents a major issue in terms of balancing the supply and demand of microgrids. DG units assume the responsibility of satisfying the system active/reactive power demand and maintaining the voltage and frequency of the system. DGs typically interface with the microgrid via power converter based voltage source inverters (VSI), which lack the physical inertia available in large synchronous generators present in traditional power systems. Given this fact, the power control mechanisms are implemented in the inverter itself, along with the droop parameters that allow the DGs to share the load among themselves in proportion to their respective capacities [29]. In droop control, DGs mimic the characteristics of conventional synchronous generators to regulate the system frequency and local voltages of the microgrid. The droop control is the best–fit control option in this situation, The droop control enables active and reactive power sharing through the introduction of droop characteristics to the output voltage frequency and magnitude of the DG units. The theory of droop control is derived from the synchronous generator droop characteristics, shown in Fig 1.7. When there is an increase in real power demand, the frequency decreases, and the local droop controller injects more active power. Similarly, when the reactive power demand increases, the voltage magnitude decreases. Consequently, the droop controller injects more reactive power to supply the increase in the reactive power demand.

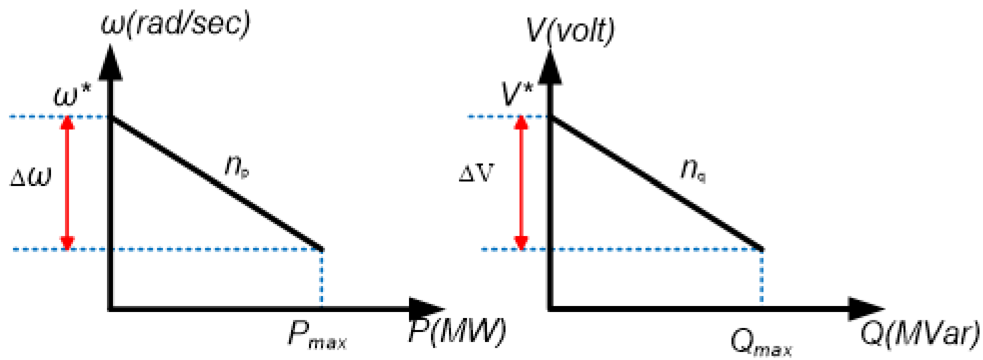

Figure 1.7: Droop control Characteristics

Further details about the dynamic and static models of droop control can be found in Chapters 2 and 3, respectively. Previous findings have found that local droop control is inadequate in IMGs due to the inability to perform adequate reactive power sharing and voltage regulation [30], as well as the inability to maintain system frequency within prescribed limits in all loading conditions [31]. To address these challenges, energy management systems (EMS) are used to dynamically adjust droop parameters in real-time to optimize the performance of the overall microgrid.

1.5 Research Gaps in SDGs Clusterd into Microgrids

The realization of SDGs clustered into microgrids that are capable of switching back and forth between grid–connected and islanded modes is strongly dependent on the implementation of appropriate design and operation methodologies that take into account the special philosophy and operational characteristics of such systems. The research in SDGs and microgrids is numerous. This thesis focuses on aspects related to the optimal configurations of microgrids with consideration of state estimation, service restoration, and integration between power and natural gas systems. As such, three main research items, within the context of this thesis, are fully surveyed to identify research gaps and issues.

1.5.1 State Estimation in Microgrids

State estimation is the first software layer within the EMS and is used to assist system operators in predicting the overall state of the system despite potentially noisy and corrupted measurements. Measurement units such as remote terminal units (RTU)s or Phasor Measurement Units (PMU)s are placed at strategic locations within the power system to measure active/reactive power injections and are then transferred to the EMS fusion center at irregular intervals [32],[33]. The EMS gathers the measurements from the fusion center and executes a state estimation algorithm to obtain the latest estimate of all states within the power system [34]. Previous works in the state estimation of microgrids assume the existence of a centralized EMS. In many cases, however, this assumption is not viable, and only local and/or distributed secondary controls are implemented in microgrids [35]. Recent studies showed that centralized state estimation is not suitable for highly dynamic microgrids that are in need of fast, accurate, and reliable updates to perform near real–time adjustments of droop parameters [36].

In order to address the challenges associated with centralized state estimation, there is great interest in developing distributed state estimation (DSE) techniques within microgrids [37]. The central fusion centre is disbanded, and instead, the network is partitioned into subsystems, referred to as zones, where each zone is given some processing resources and is responsible only for computing estimates for the state variables within its zone. For overlapping zones that may share state variables, a consensus step is required to maintain consistency for the overall state estimate. This approach improves the reliability of the state estimation process as there is no singular point of failure, is fault-tolerant to latency, and is less computationally complex than a centralized state estimation as information exchanges are limited to neighboring zones [35]. DSE techniques in power systems using this approach can be found in [38, 39, 40, 41, 42, 43, 44]

However, the aforementioned work allocates the zones arbitrarily, and does not consider the optimal placement of zonal boundaries within the overall system. The number of zones, as well as the positioning of their virtual boundaries, are key design parameters for any distributed control/estimation technique as they have a direct impact on system cost and its overall performance. In [45], boundaries are chosen to balance the computational burden of each zonal system operator, while [46, 47, 48] seek to minimize both the power imbalance and number of information exchanges within each zone. In [49], a Brute Force Search algorithm is proposed to identify optimal zonal boundaries that would decrease the vulnerability of the overall system to cyber-attacks. Yet, the method of allocation is static and is only used at the initialization of the state estimation process, which reduces the robustness of the overall state estimation process as it cannot dynamically reconfigure to adapt to system contingencies (such as loss of generators, lines, loads).

1.5.2 Self–healing Restoration in Microgrids

The necessity for implementing new solutions in distribution networks using advanced technologies, such as sensing, data processing, automatic control, and communications is growing rapidly due to a continuous shift toward distributed and variable power generation sources (i.e.DGs). In emergency conditions, microgrids can be isolated from the main grid in order to maintain the continuity of electric power service [50, 51]. While most distribution utilities shave implemented stringent regulation requirements to install DGs and allow creation of islands, several outages and failures have been recently observed due to natural disasters, such as storms and floods. These catastrophes provide a solid case for distribution utilities to explore innovative solutions for enhancing distribution automation, and facilitating the seamless integration of DGs and microgrids [52].

SDGs aim to provide the insight and controllability required to ensure the delivery of reliable, efficient and high quality power to end–users; taking into account, accommodating DGs, and the creation of microgrids as their building blocks [53]. SDG technologies are expected to provide: 1) automated switching to promptly detect and isolate faults, and then reconnect customers during unplanned outages (i.e. self-healing); and 2) accurate monitoring and forecasting, operation scheduling, and intelligent control for real time optimization of the grid to improve reliability and efficiency [54, 55].

The optimization problem of service power restoration in SDGs has been recently reformulated to incorporate different types of DGs. Numerous methods have been proposed in the literature to solve the formulated optimization problem(s). Based on the control structure and communication links, these methods can be classified into "centralized" and "distributed." The works in [56, 57, 58, 59] have proposed optimization algorithms, such as branch and bound, heuristic and meta-heuristic techniques, expert systems and weighted graphs. The authors in [60] proposed the genetic algorithm for distribution systems restoration with microgrids. The authors in [61] developed a mixed integer linear programming algorithm to operate IMGs as a black start after a disaster had occurred. In [62], a comprehensive planning algorithm for an optimal self–healing strategy was proposed. The algorithm takes into consideration all possible faults that may occur in the future. Solving optimization problems in SDGs using a centralized controlling unit (having complete knowledge of the input and an ability to implement decisions), may yield a global optimal solution for the restoration problem. However, centralized control is expected to present numerous issues for smart DGs, due to:

- Undesirable properties, with respect to reliability and scalability, due to single point-of-failure;
- Complex communication requirements and computation burdens, especially in large–scale SDGs with a high penetration of intermittent and small–sized DGs; and
- The transformation of distribution networks into distributed systems with multiple autonomous microgrids, each having limited local knowledge of the system.

Decisions, therefore, have to be implemented by the autonomous microgrids in a decentralized way.

Distributed optimization represents an analogue of centralized control, in which the variables and constraints are shared among automated agents. Using a distributed scheme, it is much easier to modify and upgrade the control of SDG components, without disturbing other parts of the control process [63]. In [64], a simple *Belief–Desire–Intention* distributed restoration algorithm was proposed. In [65], the authors proposed a fully distributed restoration process without considering DGs. In [65], a power restoration multi–agent system (MAS) was proposed for active distribution grids with DGs. The MAS contains three different types of agents: Switch, Load, and DG Agents. A heuristic algorithm was developed to solve the restoration problem among the defined agents; such an algorithm is system–dependent; it has no mathematic background, and it cannot be applied for large scale DGs. In [66], a 2-level MAS, i.e., zone and feeder agents, has been proposed. Each zone agent, in the lower layer, monitors the state within its zone and implements the assigned switching actions. The feeder agents in the higher layer run cooperative heuristic rules to determine optimal switching actions for the restoration. A scalability issue, however, is expected to arise for the defined zone agents in [66], when it is applied to large scale DGs. In [67], a MAS was proposed to optimally control the DGs to guarantee power adequacy. Yet, the work in [65, 66, 67] falls short in considering:

- The formation of self–sufficient IMGs; and

- The ability of DG transfer as an alternative means of supply adequacy.

The formation of self–supplied IMGs for a group of DG units in the restoration process might increase the number of restored loads, while reducing the required number of switching operations. The efficient way to manage a power system with significant level of DGs is to break the distribution system into small clusters or microgrids. Therefore, authors in [50, 61, 68, 69, 70] use microgrids powered by the DGs, the supply to the customers can still be guaranteed, and proved the sustainability of the isolated areas.

For this reason, a consensus–based MAS was proposed in [71], which considered the creation of IMGs, where each bus is assigned an agent. In [72], a MAS has been developed which considers the allocation of higher layer agents responsible for the loads, switches and DGs. The authors in [73] proposed a MAS for both normal and self–healing operating conditions. In the self–healing mode, the SDG is sectionalized into self–supplied microgrids in order to maximize the restored loads. In order to account for extreme outage conditions, a MAS approach was investigated in [74] to study the impact of controlled DG islanding and electric vehicles in the restoration of both single and multiple fault situations. The proposed MAS in [74] assumes four different types of agents: switch, DG, load, and an aggregator. Similar to [74], the authors in [75] considered the creation of IMGs via a group of DGs, to restore the load after a major outage. The developed distributed restoration algorithms presented in [75, 76], however, have common shortfalls:

- They are expected to face serious scalability issues, where a significant number of control agents are assumed to be installed. This, in turn, will increase the complexity of the communication and negotiation process among the agents, and thus upsurge overall execution time;
- The algorithms are not generalizable, where they are derived, based on heuristic system-dependent rules;
- Technical constraints, such as the limits of DG power transfer, were not taken into consideration;
- When microgrids operate in islanded mode, a droop control is usually applied to regulate the system frequency and voltages by providing appropriate power sharing among the DGs [77]; the model for droop–controlled power flow of IMGs has not been previously incorporated into power restoration problem.

1.5.3 Integration between Power and Natural Gas Microgrids

While most distribution utilities have implemented stringent regulation requirements to install DGs and allow local support to loads, power grids are still vulnerable to failures. As such, distribution utilities should explore innovative solutions for enhancing the distribution system resiliency and facilitate the seamless integration of DGs and microgrids. Service restoration after outages is one of the most imperative services that a microgrid can provide [78].

Energy conversion from one form to the other is one of the solutions that would contribute to more efficient load restoration. The energy conversion using power–to–gas (PtG) and gas–fired generation (GfG) units adds a new path to the energy flow and significantly enhances the system capacity. The authors in [79] present an idea for system planning while combining various energy infrastructures and the interdependency among multiple subsystems. Recently, integrated gas and power systems have attracted the attention of several researchers in order to eliminate and manage the surplus renewable generation from the power network [80, 81, 82]. In [83], a real–time scheduling model is presented for distributed system congestion management; the model also aims to utilize the price arbitrage opportunities in both the electrical and natural gas markets. In [83], the authors aim to address the issues associated with the exponential penetration of renewable generation in an integrated system via controlling the reverse power flow. In [84], a method is proposed to assess the risks associated with system outages in an integrated gas and power systems. while a limitation of the gas network and the demand side response was not taken into account. Yet, the existing studies on the integrated power and gas systems do not consider the possibility for PtG and GfG units to participate and provide restoration services to neighboring microgrids. These units will add more encouragement investment to participate in the restoration for the faulted areas.

In conclusion, this thesis is focused on the evolution of microgrids from different perspective. Table 1.1 shows the highlighted area of research in microgrids in three different areas as follow: dynamic state estimation, self-healing service restoration, and the integration with another energy form such as natural gas grids.

Table 1.1: Major challenges tackled in SDG clustered into microgrids in this thesis

Points of research	Highlighted challenges in this thesis
Dynamic State Estimation	1- While centralized state estimation is more accurate than distributed state estimation, the reliability of distributed state estimation is way higher. Therefore, an improvement in the distributed state estimation needs to be performed to enhance its accuracy. 2- Multiple objectives need to be considered in developing the distributed state estimation techniques, to enhance the performance under different operating conditions and improve the supply adequacy within the designed IMG.
Self-healing service Restoration	1- The well known optimization problem of the back-feed automatic service restoration between feeders needs to be reformulated and modified in order to consider the optimal setting of drooped DGs in IMGs, different types of energy transfer between adjacent microgrids, and the creation of a new, not predefiened IMGs. 2- The multi-agent service restoration scheme shows superiority over centralized execution. Therefore, a new algorithm based on multi-agent control needs to be optimally designed to obviate the need for a central unit and reduce the restoration complexity problem by decomposing into different optimization stages.
Integration with Natural gas grids	1- The development of the bidirectional energy conversion units between electrical microgrids and natural gas distribution grid needs to be considered. PtG and GfG are the conversion units between power and natural gas systems in order to provide several benefits, such as: energy shifting, arbitrage, and power and gas service restoration support. Therefore, an optimal scheduling for the energy conversion units needs to be developed to obtain maximum support and increase total revenue of the third party owner of the conversion units.

1.6 Thesis Overview

Under the SDG paradigm, active distribution networks are going to be clustered into small and manageable sub–systems defined as microgrids [85]. According to IEEE 1547-2018 standard, each microgrid has its own DGs and loads and capable of operating back and forth in grid–connected and islanded modes. When microgrids operate in islanded mode, DG units become fully responsible for maintaining the system frequency and regulating the voltage within the prescribed limits under all operating conditions. As such, the operation practices of these microgrids need to be carefully designed and evaluated taking into consideration the different modes of operation and integration with the entire SDGs [86]. Numerous research works have been proposed in the last few years to asses and resolve the operation challenges of SDGs clustered into microgrids with consideration of islanded mode. The vast majority of previous works focused on enhancing the secondary control (i.e., frequency and voltage regulation) and development of optimization models for microgrid EMS. Three main gaps have been identified in the literature with respect to SDGs clustered into microgrids: 1) previous research in IMGs ignored the dynamic state estimation process, which is a prerequisite and integral component in EMS to ensure stable and reliable operation under different conditions, 2) lack of optimization models for automated service restoration of SDGs considering IMGs and technical constraints of DG and load transfer between distribution feeders, and 3) integration of power and natural gas distribution systems to enhance the operation and reliability of microgrids under both normal and abnormal operating conditions.

1.6.1 Thesis Objectives

Based on the above discussions, three main objectives have been identified for this thesis to enhance the operation of SDGs clustered into microgrids as follows:

- Optimal configuration of IMGs observation boundaries considering dynamic state estimation.
- Optimal service restoration of microgrids considering islanded mode and DG and load transfer within a specific microgrid or between neighbor microgrids.
- Optimal operation scheduling of integrated power and natural gas microgrids during both normal and abnormal conditions.

1.6.2 Thesis Layout

The organization of this thesis is structured as follows:

- **Chapter 1**: Presents the state of art and critical literature survey on SDGs and microgrids.
- **Chapter 2**: Investigate the impacts of zoning choice on the performance of distributed dynamic state estimation of droop-controlled IMGs under different operation conditions. Furthermore, A multi–objective optimization model is formulated to configure the IMG into a number of zones. The objectives of the optimization model are to enhance the supply adequacy of each identified zone and minimize the state estimation error.
- **Chapter 3**: A centralized service restoration algorithm is developed for microgrids considering both grid–connected and islanded modes of operation. The proposed algorithm presented a multi–objective optimization model formulation to include different aspects in the restoration process. Different energy transfer options is introduced between adjacent microgrids: DG transfer, load transfer, and a combination of DG and load transfer. The proposed algorithm considers the creation of a new, not predefined, IMG(s) with optimal sharing of droop control parameters between DGs.

- **Chapter 4**: A novel multi–agent algorithm is presented for the automatic self–healing service restoration of SDGs clustered into microgrids. The proposed algorithm decomposes the service restoration process into two sequential stages to perform a supply adequacy assessment and perform the optimal reconfiguration between the microgrids.

- **Chapter 5**: Presents an optimal scheduling algorithm for bidirectional energy conversion units (i.e., gas-fired generators and power-to-gas units) in energy and ancillary service markets within multi–carrier microgrids. The proposed algorithm presents new contribution indices to measure the participation of energy utilities for the services, in which a motivation for the utility owners is granted. The proposed algorithm considers both normal and abnormal operating conditions of power and natural gas microgrids.

- **Chapter 6**: Presents the thesis summary, contributions, and directions for future work.

Chapter 2 - Optimum Design of IMGs Considering Dynamic State Estimation

2.1 Introduction

Due to the absence of the main grid, dispatchable DGs are responsible for holding the system voltage amplitude and frequency in IMGs [87]. Most of these DGs are interfaced with the grid via static VSI. This kind of interface lacks the physical inertia, which is available in synchronous generators rotating masses. This would, in turn, introduce a high level of susceptibility in the IMG systems to parameter variations, system disturbances and load/generation variability. State estimation is a vital tool that is deployed in EMS to aid operation decisions such as voltage and reactive power (Volt/Var) control, faults detection and isolation, and outage management. To that end, monitoring devices such as RTUs are typically mounted along distribution feeders to measure the injected active and reactive powers and then transfer these measurements with irregular intervals i.e., 10-15 minutes, [88] to the EMS for the steady–state fusion process [89]. Such paradigm shift in distribution systems calls for timely knowledge of the system states based on real–time and synchronized observations by deploying synchrophasors or micro phasor measurement units (microPMUs) [90]. In this chapter, both centralized and distributed dynamic state estimation algorithms are adopted and compared for droop–controlled IMG systems based on particle filter techniques. In the distributed approach, the IMG is clustered into couples zones to reduce the complexity and computation time of the dynamic state estimation process. Each zone is assigned with a zone state estimator (ZSE). In each iteration, each ZSE calculates its local state variables and share with its adjacent zones the state variables at the points of zone coupling until they reach a consensus. The contribution of this chapter is twofold. First, both centralized and distributed estimation algorithms are formulated for droop–controlled IMGs. The impacts of selecting the number of zones and boundaries between adjacent zones on the performance of the state estimation algorithm are investigated. Second, a new optimization problem is formulated to determine the optimum number and boundaries of zones for the distributed state estimation. Two objective functions are defined: (1) minimization of the state estimation error, and (2) minimization of the power exchange between coupling zones to make them self–sufficient. Several case studies have been conducted to validate the efficacy of the proposed optimization model.

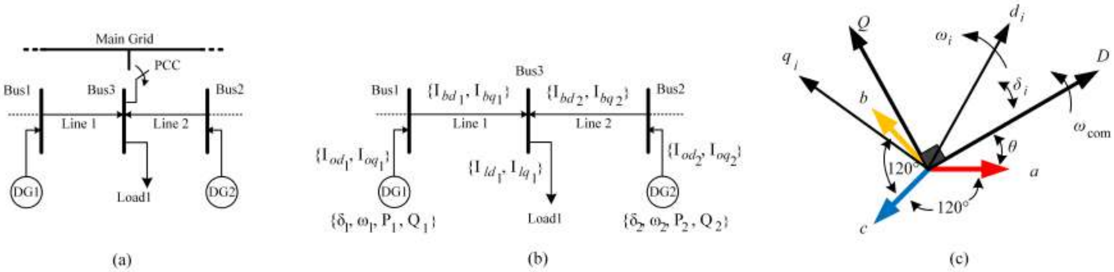

Figure 2.8: (a) An example of IMG; (b) equivalent network for the IMG in (a); (c) transformation from ABC to DQ frame

2.2 Dynamic Modeling of Droop–Controlled IMG Systems

In this section, a nonlinear time domain model is presented for the representation of the main IMG components, which are primarily DGs, lines, and loads. In IMGs, each DG rotates at its own angular frequency ω_i leading to several individual direct and quadrature (DQ) frames. As such, all state variables for the DGs, lines, and loads are transformed from their individual reference frames to a main DG reference frame that is aligned to the DQ axis defined by an angle δ_i; where δ_i represents the difference between the individual frame and the reference DQ frame [34], [91]. Fig 2.8(a) shows a single line diagram of describing the main physical components of IMG systems. Fig 2.8(b) shows the corresponding state variables for each component, while Fig 2.8(c) shows the transformation from ABC to DQ frame. By setting δ_i of the reference DG to zero, the rotating frequency can be calculated as ω_{com}, which can be used to calculate the angles of other DG units in the IMG. All state variables of the DGs f_{d_i},f_{q_i} can be mapped to (f_D,f_Q) in the reference DQ frame using the following transformation [34], [91] as in (2.1).

$$\begin{bmatrix} f_D \\ f_Q \end{bmatrix} = \begin{bmatrix} cos\delta_i & -sin\delta_i \\ sin\delta_i & cos\delta_i \end{bmatrix} \begin{bmatrix} f_{d_i} \\ f_{q_i} \end{bmatrix}. \tag{2.1}$$

According to (2.1), all IMG states can be tracked on the DQ frame and modeled based on the states defining the element. As shown in Fig 2.8, each DG unit injects its output currents I_{od_i} and I_{oq_i} to its connected bus i. It is worth noting that the representation of the DG variable states are the injected currents in addition to its rotational angle with the active and reactive power injected at bus i P_{G_i} and Q_{G_i}. Each load is specified by I_{ld_i} and I_{lq_i} representing the absorbed current at each bus i. Finally, I_{bd_j} and I_{bq_j} represent branch current flows in feeder j.

2.2.1 Dynamic Modeling of Droop–Controlled DGs

Each droop-controlled DG unit connected to bus i can be described with five state variables given as (2.2)-(2.6) using (2.1).

$$\dot{\delta}_i(t) = \omega_i^* - \omega_{com} - m_{P_i} \,.\, P_{G_i} \qquad \forall i \in \mathbb{B}, \tag{2.2}$$

$$\frac{\dot{P}_{G_i}(t)}{\omega_{c_i}} = 1.5\,(|V_i^*|\,.\,I_{od_i} - n_{q_i}\,.\,Q_{G_i}.\,I_{od_i}) - P_{G_i} \qquad \forall i \in \mathbb{B}, \tag{2.3}$$

$$\frac{\dot{Q}_{G_i}(t)}{\omega_{c_i}} = 1.5\,(n_{q_i}\,.\,Q_{G_i}.\,I_{od_i} - |V_i^*|\,.\,I_{oq_i}) - Q_{G_i} \qquad \forall i \in \mathbb{B}, \tag{2.4}$$

$$L_{C_i} \,.\, \dot{I}_{od_i}(t) = |V_{od_i}| - \sum_{i' \in \mathbb{B}} |V_{bd_{i'}}| - R_{C_i} \,.\, I_{od_i} + \omega_{com} \,.\, I_{oq_i} \,.\, L_{C_i} \qquad \forall i \in \mathbb{B}, \quad (2.5)$$

$$L_{C_i} \,.\, \dot{I}_{oq_i}(t) = |V_{oq_i}| - \sum_{i' \in \mathbb{B}} |V_{bq_{i'}}| - R_{C_i} \,.\, I_{oq_i} - \omega_{com} \,.\, I_{od_i} \,.\, L_{C_i} \qquad \forall i \in \mathbb{B}, \quad (2.6)$$

where, $\mathbb{B}$ is the set of IMG buses and feeders, respectively. The "dot" notation over a given parameter indicates the parameter's next time step estimation, i.e., $\dot{I}_{oq_i}$ is the next estimation of I_{oq_i}. $\dot{\delta}_i$ is the deviation angle associated with the DG at bus i. Since there is neither slack generator nor physical inertia to maintain the system frequency and voltage magnitudes during disturbances, primary local power controllers are usually implemented for the DG units during the islanded mode of operation to mimic the droop characteristics of synchronous generators operating in parallel [30], m_{P_i} and n_{q_i} are the operating droop parameters of the DG for active and reactive generated power, respectively. The operating drooped DG requires its no load voltage magnitude and frequency as V_i^* and ω_i^*, respectively. The control structure for any drooped DG requires an output LC filter to remove the switching harmonics produced by the inverter [92], [34]. R_{C_i} and L_{C_i} are the resistance and the inductance of the output filter, respectively. ω_{C_i} is the cutoff frequency of the output filter connecting the DG to the bus i. $|V_{od_i}|$ and $|V_{oq_i}|$ are the magnitude of the output voltage of DG at bus i in the DQ frame. $|V_{bd_i}|$ and $|V_{bq_i}|$ are the voltages at bus i which is based on Kirchhoff current law. By assuming a sufficiently large virtual resistor R_i between bus i and the ground, $|V_{bd_i}|$ and $|V_{bq_i}|$ is presented as:

$$V_{bd_i} = R_i\big[I_{od_i} - I_{ld_i} + \sum I_{bd_j}\big] \quad \forall i \in \mathbb{B} \wedge j \in \mathbb{F}, \tag{2.7}$$

$$V_{bq_i} = R_i\big[I_{oq_i} - I_{lq_i} + \sum I_{bq_j}\big] \quad \forall i \in \mathbb{B} \wedge j \in \mathbb{F}. \tag{2.8}$$

In (2.7) and (2.8), each DG injects output currents I_{od_i} and I_{oq_i} to bus i. Additionally, the currents flow between buses are a presentation for the branch states as I_{bd_j} and I_{bq_j}, where $\mathbb{F}$ is the set of the feeders number. Also, I_{ld_i} and I_{lq_i} are the states for the load currents at bus i in the DQ frame, respectively.

2.2.2 Dynamic Modeling of Branch Lines and System Loads

Branch lines and loads in the IMG are modeled in their dynamic behavior in the DQ frame. Starting with the loads in the IMG, I_{ld_i} and I_{lq_i} are presented in (2.9) and (2.10), where R_{L_i}, L_{L_i} are the resistance and the inductance of the load connected to bus i, respectively [29]. The branch lines, I_{bd_j} and I_{bq_j} are presented in (2.11) and (2.12), where R_{b_j}, L_{b_j} are the resistance and the inductance of the branch j.

$$L_{l_i} \,.\, \dot{I}_{ld_i}(t) = |V_{bd_i}| - R_{l_i}.I_{ld_i} + \omega_{com}.I_{lq_i} \,.\, L_{l_i} \;\; \forall i \in \mathbb{B}, \tag{2.9}$$

$$L_{l_i} \,.\, \dot{I}_{lq_i}(t) = |V_{bq_i}| - R_{l_i}.I_{lq_i} + \omega_{com}.I_{ld_i} \,.\, L_{l_i} \;\; \forall i \in \mathbb{B}, \tag{2.10}$$

$$\begin{aligned} L_{b_j} \,.\, \dot{I}_{bd_j}(t) = |V_{bd_i}| - \sum_{i' \in \mathbb{B}} |V_{bd_{i'}}| - R_{b_j} \,.\, I_{bd_j} \\ + \omega_{com} \,.\, I_{bq_j} \,.\, L_{b_j} \quad \forall i \in \mathbb{B} \wedge \forall j \in \mathbb{F}, \end{aligned} \tag{2.11}$$

$$L_{b_j} \, . \, \dot{I}_{bq_j}(t) = |V_{bd_i}| - \sum_{i' \in \mathbb{B}} |V_{bq_{i'}}| - R_{b_j} \, . \, I_{bq_j}$$
$$+\omega_{com} \, . \, I_{bd_j} \, . \, L_{b_j} \qquad \forall i \in \mathbb{B} \wedge \forall j \in \mathbb{F}. \tag{2.12}$$

2.2.3 Dynamic Modeling of Overall State and Observation Vectors

The overall state vestor can be formed by stacking together the state variables described in (2.2)–(2.6) and (2.9)–(2.12):

$$\boldsymbol{X}(t)=\{\delta_i(t), P_{G_i}(t), Q_{G_i}(t), I_{od_i}(t), I_{oq_i}(t), \tag{2.13}$$
$$I_{bd_j}, I_{bq_j}(t), I_{ld_i}(t), I_{lq_i}(t)\}$$

which leads to the set of nonlinear ordinary differential equations (ODE) with $\boldsymbol{\xi}(t)$ as the state noise vector.

$$\dot{\boldsymbol{X}}(t) = \boldsymbol{f}(\boldsymbol{X}(t)) + \boldsymbol{\xi}(t). \tag{2.14}$$

In state estimation, the comparison of the predicted states with the ground truth requires observations from measurement units dispersed throughout the network. This can be represented as:

$$\boldsymbol{Y}(t) = \boldsymbol{g}(\boldsymbol{X}(t)) + \boldsymbol{\zeta}(t), \tag{2.15}$$

where $\boldsymbol{\zeta}(t)$ is the observation noise vector and for the purposes of this work, the observations are considered to be the nodal voltages in (2.7) and (2.8).

2.3 Centralized and Distributed Particle Filter for Dynamic State Estimation

The particle filter is a popular choice for state estimation due to its capability of handling non–linear state and observation models [93]. Particle filter uses Monte Carlo methods in order to approximate the posterior probability distribution function by constructing it using random samples known as particles. In the very first iteration of the estimation process, each particle is created by generating N_P random state vectors based on the initial state value. These particles are then propagated through time t using the state model in (2.14) to obtain the resultant state vector for each particle p as in (2.16). Where, N_{sv} is the total number of states in vector X.

$$X_p = \begin{bmatrix} X_{p,1}^1 & \dots & X_{p,t}^1 & \dots & X_{p,T}^1 \\ X_{p,1}^2 & \dots & X_{p,t}^2 & \dots & X_{p,T}^2 \\ \vdots & \dots & \vdots & \dots & \vdots \\ X_{p,1}^{N_{sv}} & \dots & X_{p,t}^{N_{sv}} & \dots & X_{p,T}^{N_{sv}} \end{bmatrix} \forall t \in \mathbb{T} \wedge p \in N_P, \qquad (2.16)$$

The accompanying observations for each particle are found using (2.15). Once the actual measurements from PMUs at time t are obtained (2.7)–(2.8), a weighting factor W_p is generated for each particle p by comparing the actual measurements with the obtained observations. In this work, $\overline{W}_p$ is presented as a generalized weighting equation which gives a weighting factor for particle p at each time step t. Equation (2.17) is a normalization of the obtained weights to unit value of 1.

$$\overline{W}_p(t) = W_p(t) \, . \left(\sum_{p \in N_P} W_p(t) \right)^{-1} \forall \, t \in \mathbb{T} \wedge \forall \, p \in N_P. \tag{2.17}$$

The degeneracy of the particles is a main issue that needs to be considered in the particle filter where a small number of particles becomes dominant with time and have relatively higher weights than others. Therefore, a residual resampling process is added to the proposed particle filter, which update and generate random particles based on the weight distribution of the particles [94], [95]. The resampling process starts by generating vector $\widehat{Y}_p(t)$ for each particle based on its $\overline{W}_p(t)$ as in (2.18). In (2.19) the number of residual particles $N_r(t)$ to be sampled can be calculated based on $\widehat{Y}_p(t)$.

$$\widehat{Y}_p(t) = N_P \, . \, \overline{W}_p(t) \qquad \forall \;\; p \in N_P \wedge \forall t \in \mathbb{T}, \tag{2.18}$$

$$N_r(t) = N_P - \sum_{p \in N_P} \widehat{Y}_p(t) \qquad \forall \;\; t \in \mathbb{T} \wedge p \in N_P, \tag{2.19}$$

By sorting the generated vector from (2.18) to the lowest integer value, vector $Y_r(t)$ is generated, which is used to obtain a weighting vector $\widetilde{w}(t)$ as in (2.20). The cumulative sum of $\widetilde{w}(t)$ is used to sort a random variable vector U_i of dimension $N_P \times 1$ and uniformly distributed in [0, 1]. Finally, new particles are generated based on the remaining elements after sorting.

$$\widetilde{w}(t) = \widehat{Y}_p(t) - [Y_r(t)/N_r(t)] \quad \forall \;\; p \in N_P \wedge \forall t \in \mathbb{T}. \tag{2.20}$$

It is worth noting that the computational complexity of a centralized implementation of the particle filter is $\mathcal{O}(k^2 N_P)$, where k is the number of states and N_P is the number of particles [96]. In order to reduce the complexity of centralized particle filter, the mathematical formulation of a distributed implementation of the particle filter is adopted in this work. To that end, the overall IMG is decomposed into a set of N_{Sc} zones, where each zone is allocated computational resources in the form of ZSEs. Each ZSE maintains a local state vector for each particle $\boldsymbol{X_p^s}$ and an accompanying local observation vector $\boldsymbol{Y_p^s}$, which can be described as in (2.21) and (2.22).

$$\dot{\boldsymbol{X}}_{\boldsymbol{p}}^{\boldsymbol{s}}(t) = \boldsymbol{f}^{(s)}\big(\boldsymbol{X}^s(t), \boldsymbol{d}_r^s(t)\big) + \boldsymbol{\xi}^s(t) \qquad \forall s \in N_{Sc} \wedge s \neq r \wedge \forall p \in N_P, \tag{2.21}$$

$$\boldsymbol{Y}_{\boldsymbol{p}}^s(t) = \boldsymbol{g}^{(s)}\big(\boldsymbol{X}_{\boldsymbol{p}}^s(t)\big) + \boldsymbol{\zeta}^s(t) \qquad \forall s \in N_{Sc} \wedge \forall p \in N_P, \tag{2.22}$$

where $\boldsymbol{d}_r^s(t)$ is the coupling forcing term between sending (s) and receiving (r) zones, which is a vector denoting a collection of state variables that are not *directly* observed by a given ZSE, however, they are required because they are part of the local model of the zone. It is also worth noting that the computation of the local set vector $\boldsymbol{X_p^s}$ may also contain shared states with an adjacent zone. The presence of the forcing terms and shared states necessitate two–way communication between

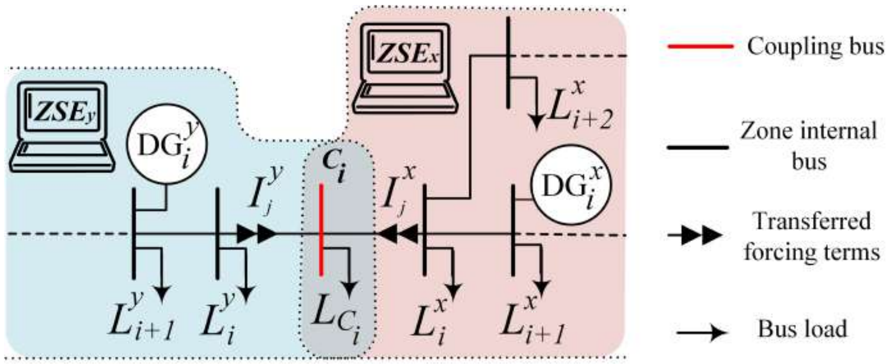

Figure 2.9: Forcing terms transactions between ZSEs at the coupling buses

adjacent ZSEs to compute the local state model and arrive at consensus for the value of the shared states.

As an example, the communication of forcing terms between adjacent ZSEs is presented in Fig 2.9. As depicted in the figure, two ZSEs are operating in a distribution system and the number of state variables varies based on the elements included in each zone i.e., the number of DGs, loads and buses. The ZSEs shared coupling bus is C_i, which is not fully observed to estimate the state variables since some information is observed from another ZSE. Therefore, forcing terms are sent between the adjacent operating ZSEs in order to fully observe and estimate the state variables of the coupling bus(es). As illustrated in Fig 2.9, the forcing term from ZSE y to x is the current flowing from each zone y to the coupling buses $d_x^y(t) = [I_j^y]$. Similarly, the forcing term from ZSE x is $d_y^x(t) = [I_j^x]$, where j is an index for the coupling feeder number between x and y ZSEs.

In order to address the aforementioned notion of shared states between ZSEs, a fusion rule is applied to arrive at consensus for their values. For each shared state $\boldsymbol{X}^k$ in ZSE s at time t, the ZSE estimates its mean μ_s^k and variance ϑ_s^k from its weighted particles and applies the fusion rule using (2.23). The summation in (2.23) is computed using average consensus [91] in the adjacent zones.

$$\dot{X}_{fu}^k(t) = \sum_{s \in N_{Sc}} \frac{\mu_s^k(t) \,.\, \vartheta_s^k(t)}{\vartheta_s^k(t)} \quad \forall\, k \in N_{sv} \wedge \forall\, t \in \mathbb{T}. \tag{2.23}$$

Now that consensus is achieved for the shared states, each ZSE may request the forcing terms from each adjacent ZSE for the next iteration and compute the final state estimate. If the IMG is partitioned into N_{Sc} zones, the average number of state variables per ZSE is roughly N_x/N_{Sc}. Assuming the use of N_P particles, the complexity of the proposed algorithm is $N_{Sc} \times \mathrm{O}((N_x/N_{Sc})^2 N_P) \approx \mathrm{O}(N_x^2 N_P/N_{Sc})$ leading to a computational saving of a factor of N_{Sc} in favour of the DPF.

2.4 Design of ZSEs Based on DPF

The design of DPF aims to select the number and boundaries of the ZSEs to minimize the root mean square estimation error (RMSE) for each state k. Equation (2.24) illustrates the main objective function. The calculated $X_{Err}^{s,k}$ is subject to the total number of the assigned Monte Carlo (MC) iterations N_{MC}. It is noteworthy that MC simulations are conducted to verify that the DPF accurately tracks the

IMG state variables despite using significantly corrupted state and observation values as will be illustrated in the case studies.

$$X_{Err}^{s,k} = \sqrt{\frac{1}{N_{MC}} \sum_{m} \sum_{t} (X_t^{k,m} - X_T^{k,m})^2} \quad \forall k \in N_{sv} \wedge m \in N_{MC} \wedge \forall t \in \mathbb{T}, \quad (2.24)$$

$$X_{Err}^{s,k} \leq \varepsilon \qquad \forall k \in N_{sv} \wedge \forall s \in N_{zc}. \quad (2.25)$$

The $X_{Err}^{s,k}$ is tested to an inequality constraint limited to certain threshold (ε), which is assigned by the system operator based on the required accuracy [97],[98] as in (2.25). The *RMSE* is tested for possible operating scenarios that might occur in the system, in which a violation of the ε, will lead to another search for the virtual boundaries. If the ε is within the acceptable limit, another scenario i_S will be tested on the assigned virtual boundaries until the algorithm reaches N_{Sc}. The most acceptable configuration of the virtual boundaries with the total N_{Sc} will be set as the optimal designed solution for the operating ZSEs. Flowchart of the proposed solution is shown in Fig 2.10.

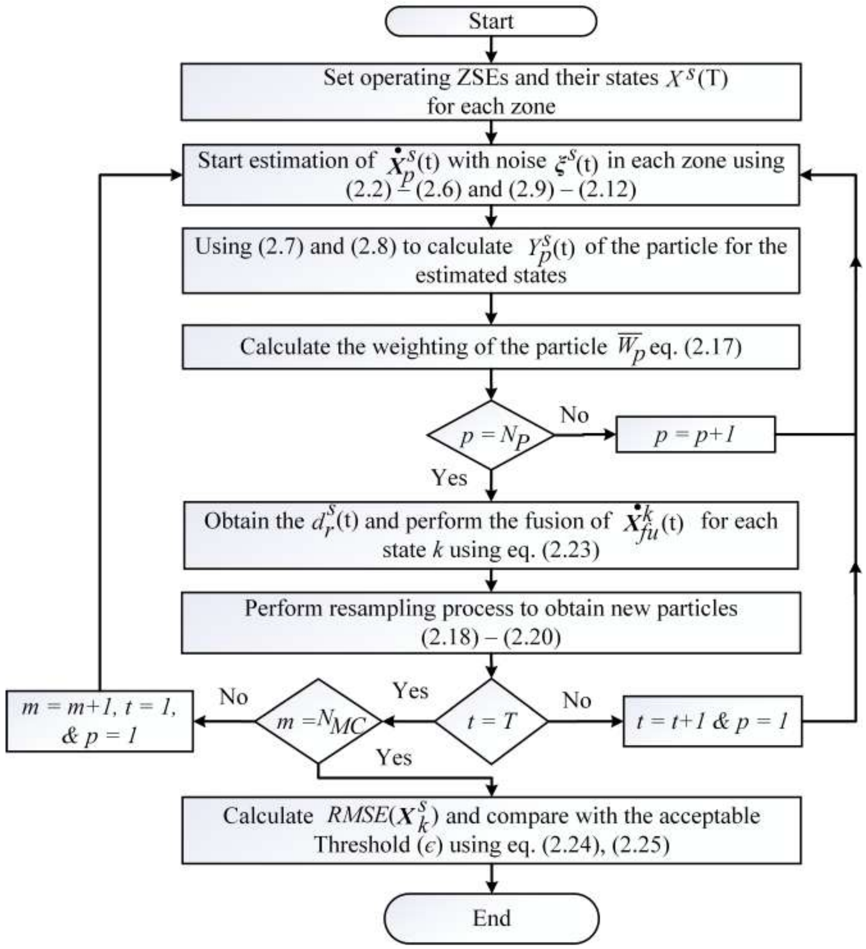

Figure 2.10: Flowchart for each ZSE

2.5 Case Study for Designing ZSEs

The IEEE 33–bus distribution feeder [30] has been used in this work to test the effectiveness of the proposed algorithm for distributed and dynamic state estimation in IMG systems. As shown in Fig 2.11, the 33–bus distribution feeder is simulated as

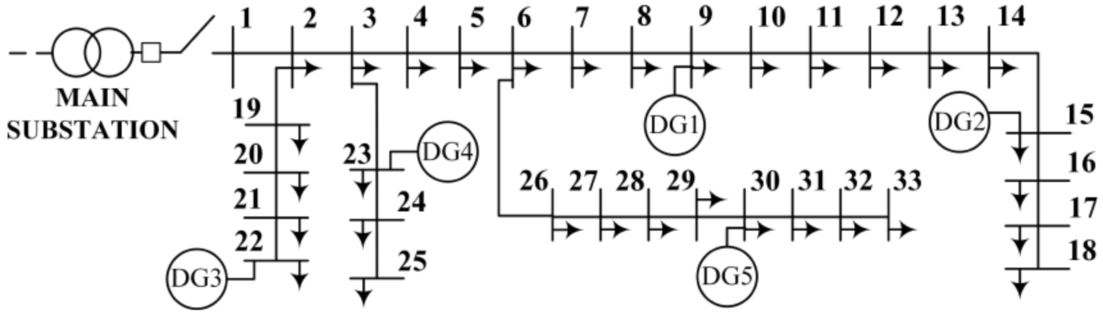

Figure 2.11: Typical IEEE-33 distribution bus system

an IMG, which operates at 12.66 kV. Without loss of generality, it is assumed that 5 dispatchable and equally sized DG units are installed in this system with a capacity of 500 KVA for each unit. The DGs are located at bus 9, 15, 22, 23, and 25. All DGs are droop–controlled, where the active and reactive power droop parameters m_P and n_q, are selected to be 30.4×10^{-5} and 1.3×10^{-3} per unit, respectively. ω^* is set at 1 per unit for all DGs with a base value of 60 Hz. The output filters connected to the DGs have the R_C and L_C of 0.747 ohm and 0.001273 H, respectively. The IMG dynamic state model has been implemented in the MATLAB environment, in which the ODE routine given in the MATLAB was used to estimate and solve the dynamic parameters of the IMGs. A discretized time state space model with fixed time step has been developed using the solution of the ODEs, in which the discretized model adopts the proposed DPF algorithm in MATLAB. For the purposes of simulation, the state values are augmented with state noise to reflect the inaccuracy of the mathematical modeling of the IMG. The resultant state vector is established as the ground truth. A similar process occurs with the output of the observation model, which is augmented with observation noise to reflect the inaccuracies of the measuring units. The metric to measure the noise is the signal to noise ratio (SNR), and is set differently for each case study to test the reliability of the proposed DPF, where a higher SNR represents a more accurate signal. Due to the high dynamic change of IMG, the simulation is performed with a time step of 0.083sec. The accuracy of the centralized particle filter and DPF increases with the number of particles used in the estimation process, therefore in this chapter a significant trials have been made to achieve the optimal number of particles considering the computational complexity. A total of 100 particles have been selected in this work, in addition to MC iterations used to evaluate the RMSE. The time of simulation is set to be 20 sec. Starting from the black start of the DGs, equal active power sharing reached after 2.5 sec. This periodic time might vary based on the droop parameters of the installed DGs. In the IMG, the frequency of the system is constant while the voltage at each node is different. Since the installed DGs are assumed to be equal in size and have the same droop settings, they will share the same active power generation of 65KW which is depending on the frequency of the system, while they will not share the same reactive power since the voltage is different. Fig 2.12 shows the output power sharing of the DGs in the IMG, where (a) and (c) show the sharing power without any noise while (b) and (d) show the same sharing

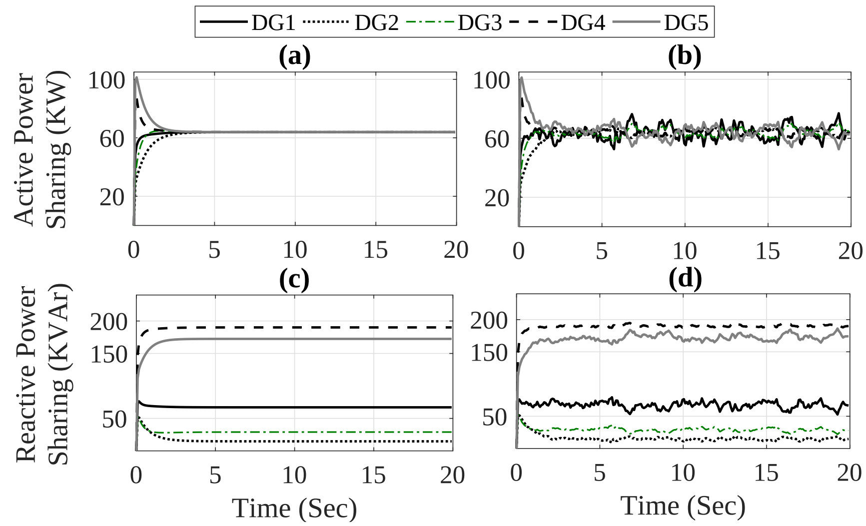

Figure 2.12: Active and reactive powers for the droop-controlled DG (a) and (c) without, and (b) and (d) with Gauissen noise, respectively

power with Gauissen noise.

The proposed DPF is tested under different number and boundaries of zones as shown in Table 5.14. Multiple system disturbances are assumed to occur to test the robustness of the selected number of zones under different operating conditions. The first event is a sudden load increment of the loads located in L2–L5 for a short time from the 6^{th} to the 8^{th} seconds. In the second event, a load decrement is assumed in load points L2–L11 at the 11^{th} sec until the end of the simulation at the 20^{th} sec. To complicate the ground truth of the IMG, a third event is assumed with a sudden load increment in L6–L11 taking place during the second event at the 17^{th} sec until the 20^{th} sec.

Table 2.2: Selected boundaries for each zone in DPF

Estimation Zones	Buses included in the zones				
	ZSE_1	ZSE_2	ZSE_3	ZSE_4	ZSE_5
DPF-2Z	1-5, 19-25	5-18, 26-33	—	—	—
DPF-3Z	1-5, 19-25	5-8, 26-33	8-18	—	—
DPF-4Z	1-3, 19-22	3-6, 23-33	6-12	12-18	—
DPF-5Z	1-3, 19-22	3-5, 23-25	5-12	12-18	6, 26-33

Figures 2.13 and 2.14 show the ground truth with the estimated values for the generated active and reactive powers of DG1 located at bus 9, respectively. The figures are plotted at SNR of 25 dB and at different number of zones as described in Table 5.14. As shown in the figures, the track of DPF to the ground truth of the IMG states is improved when the number of zones increases. It can be shown that the solution converges with a minimum RMSE at DPF-4Z, since DPF-5Z gives the same state estimation as the DPF-4Z. The number of states in the DPF-4Z are equally distributed among the assigned zones based on the number of DGs, loads and the forcing terms from the neighbour zones.

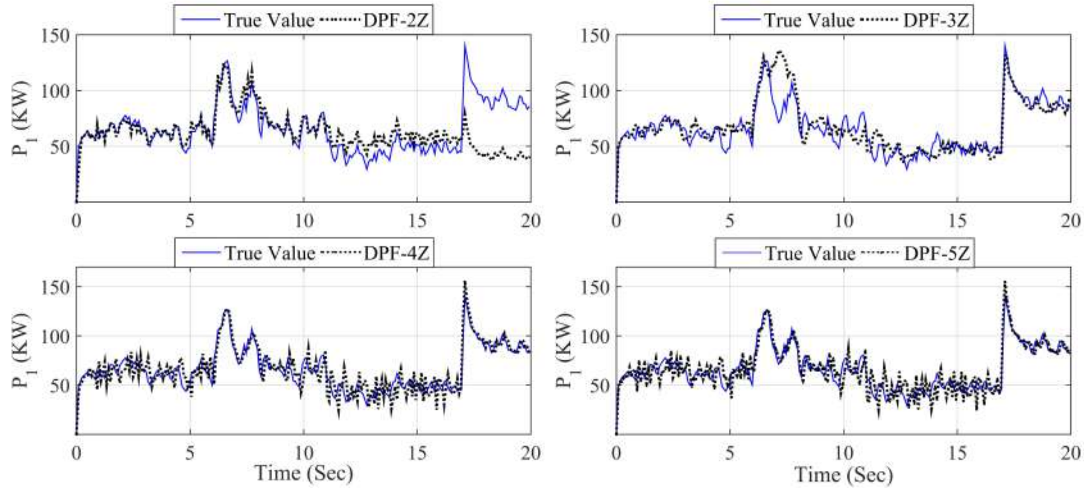

Figure 2.13: DG1 Active power state with Gaussien noise and 25dB SNR

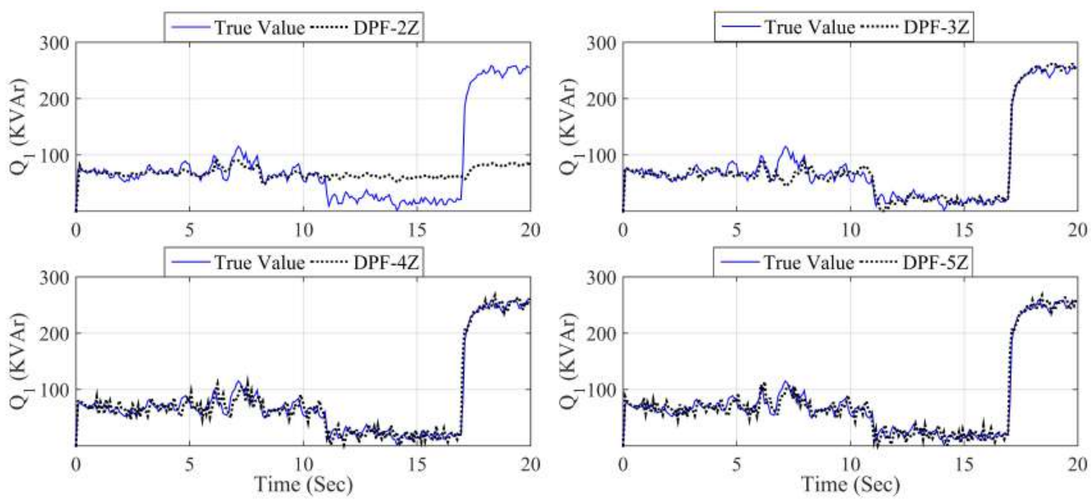

Figure 2.14: DG1 Rective power state with Gaussien noise and 25dB SNR

Figure 2.15 presents the maximum RMSE for the estimated states occurred between the DPF-3Z and the DPF-4Z using different types of noises with different SNR. The state and observation models are corrupted with different types of ad-

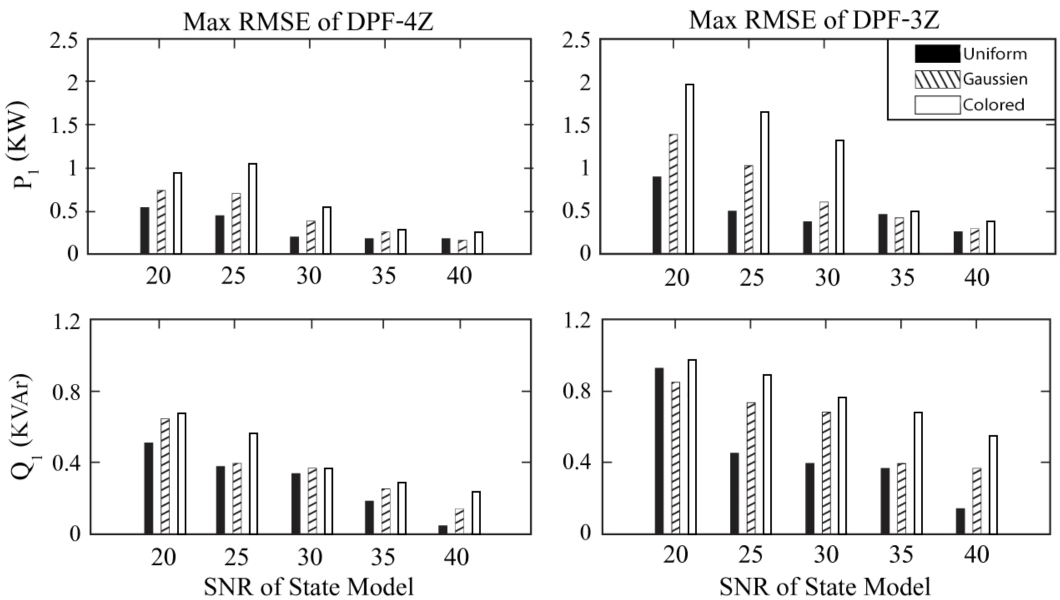

Figure 2.15: Different SNR and noise types on the proposed DPF

ditive noise that include: Gaussian, Uniform, and Colored noise [89]. As shown in the figure, the proposed DPF is superior in tracking the ground truth and its accuracy is significantly enhanced with the selection of the appropriate number of zones.

The results show that appropriate design for the number of zones and their boundaries could impact the accuracy of the proposed DPF and thus careful consideration should be given to the design of distributed state estimation algorithms for IMG systems. In the second phase of this chapter, an optimal design and configuration for the ZSEs is presented.

2.6 Optimization Model for the Design of ZSEs

In a distributed zones environment, each ZSE has its own states where this process overcomes the computational burden and the complexity of estimating highly dynamic and non-linear IMGs. This will, in turn, achieve a global solution for the distributed state estimation problem [36]. Hence, careful consideration should be given for the clustering mechanism of IMGs into zones. In addition to state estimation consideration, the determination of zone boundaries dividing existing individual or coupled IMGs into smaller zones might need to take into account other operation requirements and/or objectives. Without loss of generality, the power adequacy limits between the suppliers (i.e. DGs) and the loads within the created zones is identified as a key operational requirement. Where the power adequacy in the clustered zones must maintain the transferred power between zones for protection purposes, such as failure of another zone. This constraint will prevent the expansion of the fault for healthy sections and helps in the study for the self–healing process from the neighbor zones [99]. It is worth noting that this work assumed that the physical configuration of the system is not changed for the design of the zones, and the physical reconfiguration process and the usage of the tie lines are left for the restoration process in case of an emergency. Toward this trend, the optimal designing of zones for the distributed state estimation is proposed using the ZSEs with the DPF technique, where *virtual* boundaries are defined for each ZSE. The main objective function of the optimal zoning design is to create a set of adequate zones that consider the probability of fault events occurrence in the IMG, with the consideration of the total estimation accuracy. In the IMG, all the grid components can undergo active failure events such as short circuit in the conductors or the breakers. In addition to the active failure events, the passive failure events need to be considered because there can be cases where a passive opening of a conductor often come in contact with ground or other component, which leads to a short circuit condition. Also, error in protection or a lack of situation awareness from the operator will lead to passive failure events [100]. In order to test the accuracy of the created zones on the active ZSEs, a wide variety of system operating conditions and events are assumed in this work such as line failure, sudden load drop, sudden load increase etc. The main objective function of the proposed algorithm is shown in (2.26), which focus to minimize the transferred energy between the coupled zones for the total time T in different scenarios N_{Sc}. The objective function of the proposed DPF algorithm gives the advantage to isolate a faulty zone without the defect of the healthy area;

$$\text{Min. } f(N_{Sc}, T) = \sum_{x \neq y} \Delta S_{cop}^{x,y} \qquad \forall x, y \in N_s. \tag{2.26}$$

where; $\Delta S_{cop}^{x,y}$ is the total apparent transferred power between coupling zones x and y, which can be calculated by the transferred forcing current terms with the

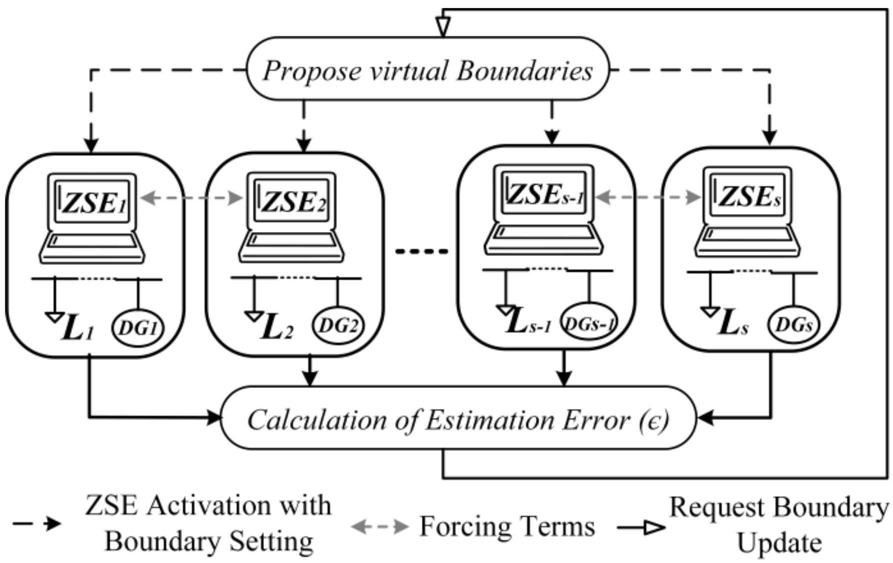

Figure 2.16: Schematic diagram for the proposed design of ZSEs for DPF in IMGs

impedance to the coupling buses. The coupling zones x and y belong to the number of zones N_s on the IMG.

Figure 2.16 shows a schematic diagram for the optimal designing of the proposed DPF. The proposed DPF algorithm identifies and creates the virtual boundaries for the ZSEs based on the required number of zones N_s. Once the virtual boundary is assigned to the ZSE, it begins its local state estimation process. If the estimation process produces an accuracy that exceeds a configurable threshold, the proposed algorithm will search for a new configuration of the virtual boundaries. The proposed algorithm uses the historical data of the DGs and loads to determine the DG output and the required loads in each zone. The objective function is subject to the steady state operational constraints for a distribution system as follow:

2.6.1 Power Flow Constraints

The mismatch power flow equations considering droop controlled DGs are:

$$m_{P_i} \;.\; P_{L_i} = \omega - \omega_i^* + m_{P_i} \;.\; |V_i| \sum_{i' \in \mathbb{B}} \left[|V_{i'}| \;.\; Y_{ii'} \;.\; cos(\theta_{ii'} + \delta_i - \delta_{i'}) \right] \quad \forall i \in \mathbb{B}, \tag{2.27}$$

$$n_{q_i} \;.\; Q_{L_i} = |V_i| - |V_i^*| + n_{q_i} \;.\; |V_i| \sum_{i' \in \mathbb{B}} \left[|V_{i'}| \;.\; Y_{ii'} \;.\; sin(\theta_{ii'} + \delta_i - \delta_{i'}) \right] \; \forall i \in \mathbb{B}, \tag{2.28}$$

where; ω is the operating frequency of the system. $|V_i|$ is the voltage bus connected to the DG. $Y_{ii'}$ and $\theta_{ii'}$ are the Y-bus admittance magnitude and angle between buses i and i', respectively, δ_i is the voltage phase angle at bus i.

2.6.2 Operational Limitations

The IMG has no slack bus to maintain the frequency ω at one per unit. For this reason, the frequency is defined as a state variable, with upper and lower boundaries given in (2.29). In addition, the droop–controlled IMG needs to maintain the operational limitations of the connected buses [30]. In which, the operational voltage of each bus i must be maintained within its specified voltage regulation minimum and maximum limits V_i^{min} and V_i^{max}, respectively, as shown in (2.30). Finally, for every branch $\mathbb{F}$ the line power flow S_j must meet the specified line capacity limits in case of failure [101] formulated as in (2.31)

$$\omega_{min} \leq \omega \leq \omega_{max}, \tag{2.29}$$

$$|V_i^{min}| \leq |V_i| \leq |V_i^{max}| \quad \forall i \in \mathbb{B}, \tag{2.30}$$

$$|S_j| \leq |S_j|^{max} \qquad \forall j \in \mathbb{F}. \tag{2.31}$$

2.6.3 Number of Observation Zones

When there is a certain desired number of operating ZSEs is given by the IMG operator, the designed zones N_{zc} needs to be limited to the desired number of operating ZSEs. This constraint can be mathematically formulated as in (2.32), where R is the solution space for all possible configurations.

$$config \in R[N_{zc} = N_s]. \tag{2.32}$$

2.6.4 State Estimation Error Calculation

After assigning the operating ZSEs, the state estimation error is tested by calculating the difference between the estimated state variables X_t^k and their true values X_T^k as in (2.24), after the execution of the proposed DPF state estimation algorithm ,described in the first fold of this chapter, through time T. The proposed flowchart in Fig 2.10 is updated to Fig 2.17, which provides an updated flowchart summarizing the proposed optimization algorithm of DPF.

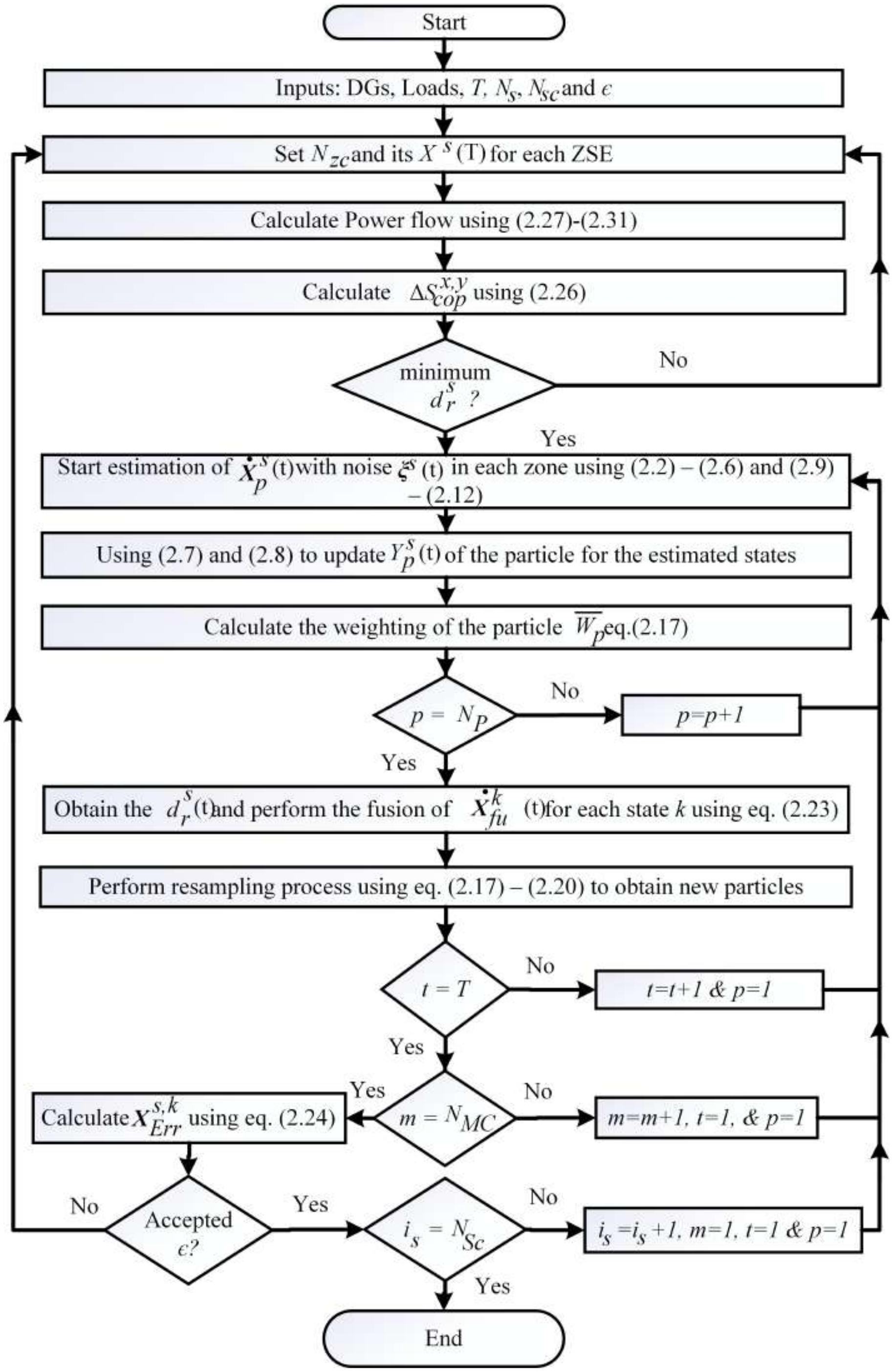

Figure 2.17: Flowchart for the proposed optimization model for DPF in IMG

2.7 Case Studies for the Optimized Model of the ZSEs

The IEEE 33–bus distribution feeder given in Fig 2.11 was used for the proposed algorithm with the same DG assumptions and without the assumption of predefined boundaries for ZSEs. Where, two case studies are presented, including different scenarios in the IMG. The first case study is presented to test the optimal zoning solutions compared to the centralized particle filter, since the fusion process is absent in the centralized particle filter, which will result in an increase of the state estimation accuracy. Further, in the same case study, a comparison is performed between an arbitrary boundaries of the ZSEs and the optimal zoning configuration with the same number of N_s. In the second case study, a sensitivity analysis of choosing the number of zones is presented to show the optimal selection of the N_s for specified system; this case study is tested in different SNR values and types of noises.

2.7.1 Optimal Solution of the Proposed DPF Algorithm

In the first case study, the assumed type of state noise is white Gaussian noise with SNR of 25dB, since the white Gaussian noise was found intrinsically in many real–world systems. DG1 at bus 9 is the reference bus in which the rotational phase angle around the DQ frame equals to zero. To increase system fluctuations, a scenario of different events is adopted for the first case study. The first event is a sudden load incrimination occurred at bus 2 to bus 5 from the 6^{th} to the 8^{th} seconds in addition to a second event which is assumed to be a load outage at buses 2 to 11 at the 11^{th} sec until the end of the estimation time. Furthermore, a third event is assumed as sudden load incriminate from bus 12 to bus 22, this fault is assumed to occur during the second event at the 17^{th} sec until the end of the simulation period. This scenario is specifically chosen to show the difference between an optimal and arbitrary virtual boundaries. In this case study, N_s is set to be 3 where the proposed algorithm needs to optimally configure the virtual boundaries of the 3 operating ZSEs. Figure 2.18 shows the main parameters of DG1 power generation (P_1 and Q_1) using the DPF proposed algorithm compared to the centralized particle filter. As shown in the figure, the estimation of the optimal DPF-3Z obtained using the proposed algorithm at Figs 2.18 (c) and (f) is superior to capture the ground truth of the state variables for the active and reactive power generation of DG1, respectively. Compared with the centralized particle filter at Figs 2.18 (a) and (d), the proposed DPF algorithm can perform the state estimation with an equivalent accuracy to the centralized particle filter. Another solution with an arbitrary selection and configuration for 3 operating ZSEs is presented at Figs 2.18 (b) and (e), showing the failure of tracking down the ground truth of the state variables with several events occurred at the same time. The arbitrary DPF-3Z shows the efficacy of using the proposed DPF algorithm.

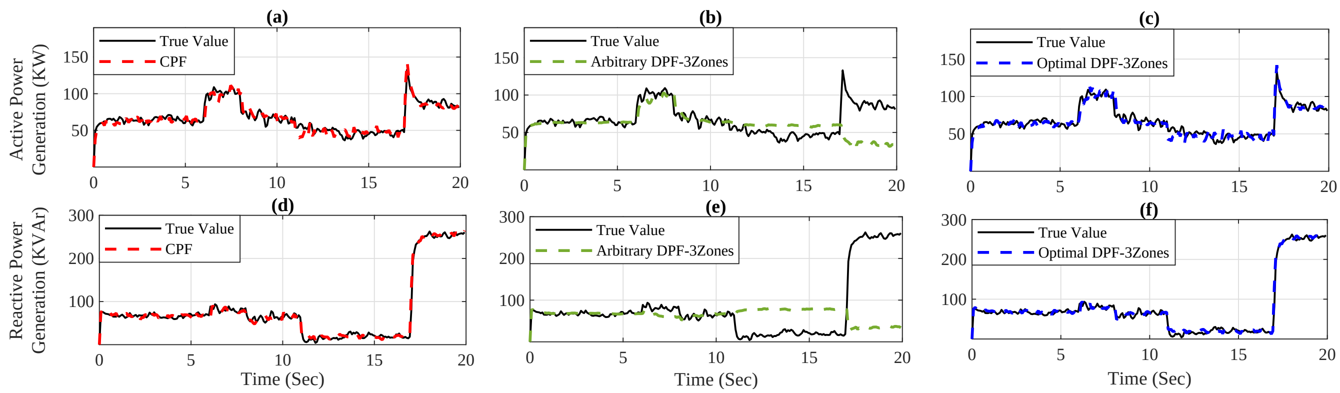

Figure 2.18: Active and reactive state variables for DG1 at 25dB with white Gaussian noise. (a) and (d): Tracking of the centralized particle filter to the true values of the states, (b) and (e): Tracking of an arbitrary DPF-3Z to the true values, (c) and (f): Tracking of the optimal allocated DPF-3Z to the true values

As shown in the figure, the arbitrary boundaries selection fails to track the fluctuations of the state variables at 25dB. In addition, during the second event at the 11^{th} sec, the margin between the predicted state variable and the ground truth increases, which result in an increase for the $X^{s,k}_{Err}$ regarding the studied state variables at Fig 2.18 to their specified ε. Figure 2.19 shows the optimal configuration of the virtual boundaries of the 3 ZSEs using the proposed DPF algorithm and Fig 2.20 shows the minimized forcing terms between the configured zones based on the main objective function of the proposed algorithm.

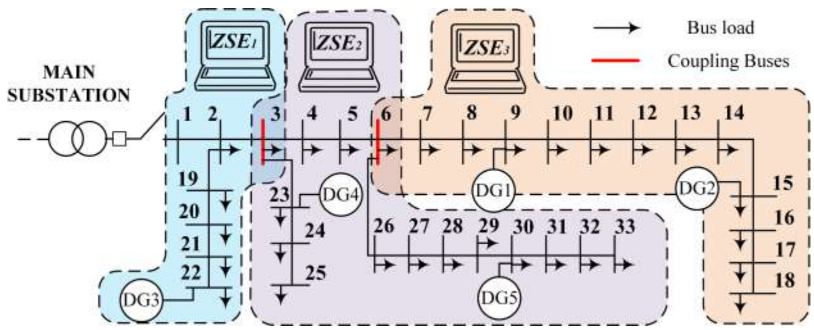

Figure 2.19: Operating ZSEs with the optimal configuration of their factitious boundaries based on the proposed algorithm with DPF-3Z

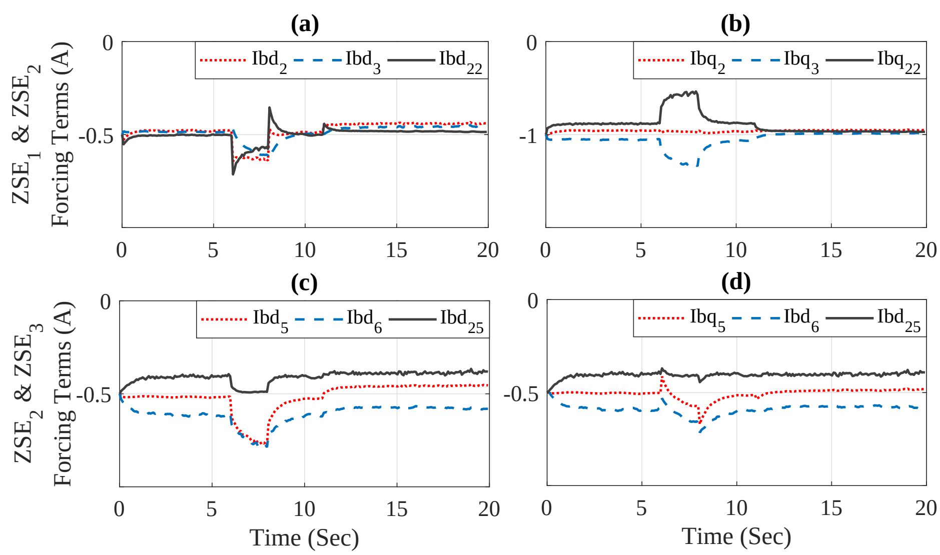

Figure 2.20: Transferred forcing terms for the optimal DPF-3Z. (a) and (b): Forcing terms between ZSE_1 and ZSE_2 in the DQ axis, respectively. (c) and (d): Forcing terms between ZSE_2 and ZSE_3 in the DQ axis, respectively.

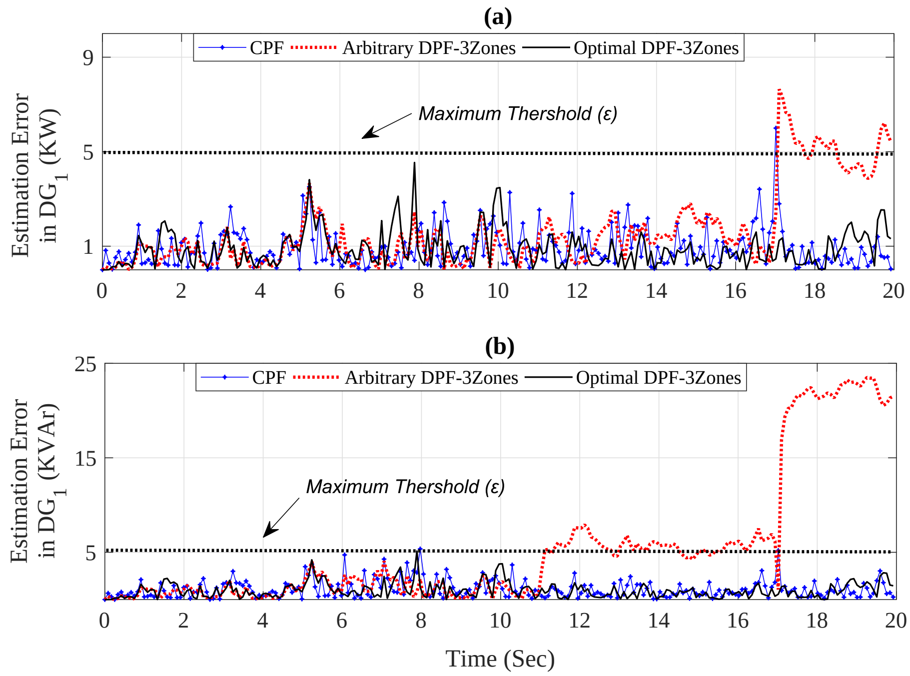

Figure 2.21: The resultant root mean square error. (a), (b): Estimation error of the active and reactive power generation for DG_1 using different SE configurations, respectively.

In Figure 2.21 presents the X_{Err} regarding P_1 and Q_1, where the maximum allowed ε is assumed to be 5%. As shown in the figure, the only solution that is not exceeding the maximum threshold is the obtained solution form the proposed algorithm for both active and reactive power.

2.7.2 Sensitivity Analysis for the Proposed Optimization Model of DPF

A second case study is presented to show the effect of selecting the number of N_s for the proposed optimization model, in order to minimize the operational cost of the operating ZSEs. Using the same events described in the first case study, the proposed algorithm will be tested under different SNR values and types of noises: Gaussian, uniform, and colored [34]. Fig 2.22 shows the power generation state variables of DG4 at bus 23 with a SNR of 30dB, using different sets of N_s. The proposed DPF algorithm is used to configure the virtual boundaries for each set of N_s. Starting from DPF-2Z, the optimal configuration is generated using the proposed algorithm and the tracking results are shown in Figs 2.22 (a) and (e) for the active and reactive power generation, respectively. The results clear demonstrate that the DPF-2Z fails to track down the ground truth of the state variables. Using N_s equal to 3, the optimal configuration is obtained as in the first case study and the simulation results is shown in Figs 2.22 (b) and (f). By comparing the optimal solutions for the DPF-4Z and DPF-5Z at Fig 2.22 (c), (d), (g) and (h), the difference between their estimations are almost the same, which means that increasing N_s beyond 4 does not contribute to the accuracy of the estimations. However, making N_s more than 4 is possible for 33–bus IMG. In order to reduce the operational cost of the operating ZSEs, the optimal solution of the DPF-3Z is the suitable number for distributed state estimation, where the X_{Err} for all state variables are equivalent to the DPF-4Z.

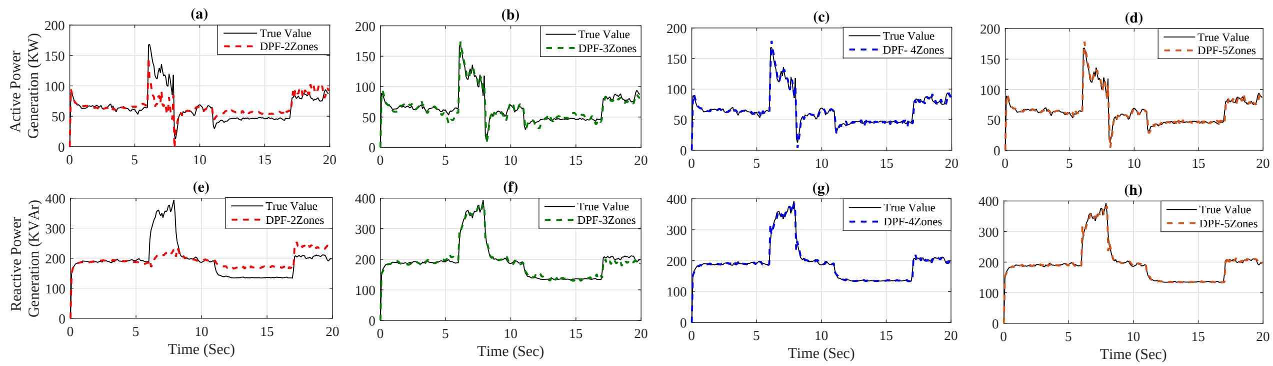

Figure 2.22: Tracking of the optimal zones configuration for the active and reactive power generation in DG4 at 30dB and white Gaussian noise. (a) and (e): Tracking of the optimally allocated DPF-2Z to the true value, (b) and (f): Tracking of the optimally allocated DPF-3Z, (c) and (g): Tracking of the optimally allocated DPF-4Z, (d) and (h): Tracking of the optimally allocated DPF-5Z.

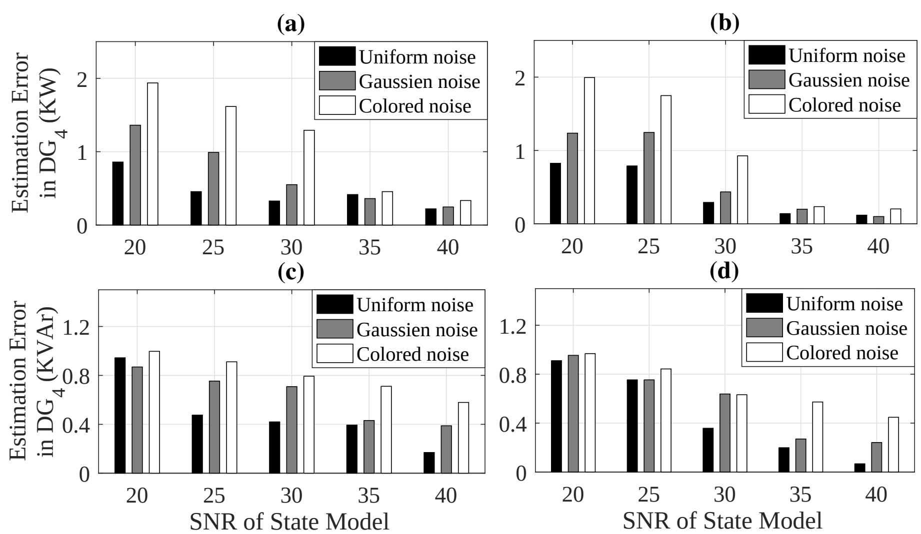

Figure 2.23: Impact of SNR and Noise type on the proposed DPF. (a) and (c) are the maximum estimation error occured for the active and reactive power generation in DG_4 using DPF-3Z, respectively. (b) and (d) are the maximum estimation error occured for the active and reactive power generation in DG_4 using DPF-4Z, respectively.

Figure 2.23 presents the maximum X_{Err} occurred for the second case study using different types of noises with different SNR values for both DPF-3Z and DPF-4Z. The results show that the proposed optimal design of DPF state estimation is superior in tracking the ground truth under different SNR values and types of noise signals.

2.8 Summary for the Proposed Zoning Mechanism for DSE

This chapter compares the performance of centralized and distributed particle filters for dynamic state estimation in droop–controlled IMGs. The impacts of zone numbers and boundaries of DPF on the accuracy of the state estimation is investigated. An optimization model is developed to design the number of zones and identify their boundaries. Two objective functions are defined in the formulated optimization problem: minimization of the RMSE of the state estimation and creation of self–adequate virtual zones by minimizing transferred power among zones. The proposed DPF algorithm can be easily implemented in a real IMG system, where loads and generations vary, and the importance of the estimation is critic to prevent catastrophic outages. The performance of the proposed DPF is measured in number of MC iterations considering the collection of the data with the fusion process. The simulation results show that appropriate design of zones enhances the performance of DPF significantly.

Chapter 3 - Centralized Self–healing Service Restoration Plans for Microgrids

3.1 Introduction

The integration of DG units and other emerging components such as microgrids can have an impact on the operation practices used to be applied in conventional power distribution systems. In fact, various operational strategies are expected to face numerous challenges due to the high degree of complexities that is accompanied with the transformation of distribution networks into SDGs clustered into microgrids. For instance, local distribution companies might no longer able to detect and isolate faults and/or restore the outage loads using the human operator's experimental rules. This, in turn, necessitates the need for implementing automated self-healing mechanisms in SDGs that are considering the special control features and operational characteristics of DGs and microgrids. In this regard, the state-of-the-art self-healing restoration of distribution networks should be adopted to take these new features into consideration.

This chapter introduces the topic of self-healing restoration process for SDGs clustered into microgrids, in which the faulted section is detected and restored using a centralized controller managed by the DNO and/or the microgrid operator. The contribution of this chapter is twofold. The first fold is directed towards developing a self–healing restoration algorithm for droop–controlled IMG systems. To that end, appropriate power flow models for droop–controlled DGs have been incorporated in the optimization problem to provide proper representation for microgrids during islanded mode of operation. Several case studies have been conducted in order to validate the proposed IMG restoration algorithm. In the second fold, an automated back–feeding service restoration algorithm is proposed for SDG clustered into micogrids. The central features of the new proposed algorithm that differentiate this work from the literature are: 1) using DG units as alternative supply configuration; where three types of energy transfer between the adjacent feeders are introduced (load, DG and load/DG); 2) the creation of IMGs via optimal DG and load transfer actions; and 3) the simplicity of the proposed algorithm.

3.2 Steady–state Modeling of Droop–Controlled IMGs

As discussed in previous chapters, the majority of DG units forming microgrids are interfaced via dc-ac power electronic inverter systems. In islanded mode, droop control that enables active and reactive power sharing through the introduction of droop characteristics to the output voltage frequency and magnitude of dispatchable DG units is usually applied. In this section, a review of the steady–state modeling for the concept of droop–based control scheme is presented.

3.2.1 Transmission Line Power Transfer Theory

The active and reactive power transfer in transmission lines is based on the voltage and the phase angel at both sending and receiving bus sides. The active power and reactive power flowing into the transmission line at the sending end can be given as follows:

$$S_i = P_i + jQ_i = V_i.I^* = V_i.[\frac{V_i - V_i.e^{-j\gamma}}{jX}]^* \tag{3.1}$$

$$P_i = \frac{V_i.V_j}{X}.sin\gamma^* \tag{3.2}$$

$$Q_i = \frac{V_i.(V_i - V_j.cos\gamma)}{X} \tag{3.3}$$

where; P_i and Q_i are the active and reactive power at line i, respectively. S_i is the total complex power at line i, V_i and V_j are the voltages at sending and receiving sides, respectively. I is the current flow in the line, γ is the power angle, and X is the line inductance. In transmission lines, the power angle is very small, therefore it can be assumed that $sin\gamma = \gamma$ and $cos\gamma = 1$. Accordingly, one can observe that the active power is strongly dependent on the power angle, while the reactive power is strongly dependent on the voltage of the sending and receiving ends. Therefore the frequency droop can regulate the active power and the voltage droop can regulate the reactive power. Based on the droop concept, the inverters of dispatchable DG units in IMG are controlled to imitate the behaviors of synchronous machines by applying the following droop equations:

$$\omega - \omega_o = -m_P.(P - P_o) \tag{3.4}$$

$$V - V_o = -n_q.(Q - Q_o) \tag{3.5}$$

where, ω is the system frequency, V is the voltage magnitude, ω_o is the nominal system frequency, V_o is the nominal voltage magnitude, P and Q are the inverter output of active and reactive powers, respectively. P_o and Q_o are the momentary set points for the active and reactive powers of the inverter. m_P is the frequency droop parameter, and n_q is the voltage droop parameters.

3.2.2 Voltage and Frequency Control

Figures 3.24 (a, b) shows the power sharing of two inverters based on droop control. Let's assume that the frequency droop parameters of the two inverters are m_{P_1} and m_{P_2}, and the output active power of the two inverters are P_{10} and P_{20} at the nominal frequency of the grid ω_o, respectively.

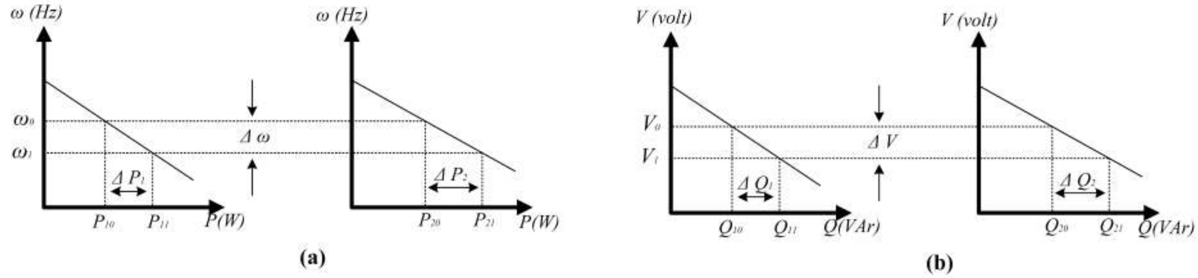

Figure 3.24: (a): Active power sharing in droop control: (P–ω) characteristics; (b): Reactive power sharing in droop control: (Q–V) characteristics.

When the load increases, the two inverters change their output power and the system frequency is changed from its nominal frequency to ω_1. Such change in active power can be formulated mathematically as follows:

$$\Delta P_1 = P_{11} - P_{10} = -\frac{1}{m_{P_1}}.(\omega_1 - \omega_o) \tag{3.6}$$

$$\Delta P_2 = P_{21} - P_{20} = -\frac{1}{m_{P_2}}.(\omega_1 - \omega_o) \tag{3.7}$$

Similar to (3.6) and (3.7), the two inverters share the reactive power demand as shown in Fig 3.24 (b). Figure 3.24 shows the active and reactive power sharing in which they are mainly governed by the static droop parameters of active and reactive power, where

$$\frac{\Delta P_1}{\Delta P_2} = \frac{m_{P_2}}{m_{P_1}} \tag{3.8}$$

$$\frac{\Delta Q_1}{\Delta Q_2} = \frac{n_{q2}}{n_{q1}} \tag{3.9}$$

Equations (3.8) and (3.9) are used as virtual communication mediums among the inverters in order to represent the active and reactive power sharing between the DGs. For n droop-controlled DG units, (3.10) and (3.11) below are met

$$\Delta P_1.m_{P_1} = \Delta P_2.m_{P_2} = \cdots\cdots = \Delta P_n.m_{P_n} \tag{3.10}$$

$$\Delta Q_1.n_{q_1} = \Delta Q_2.n_{q_2} = \cdots\cdots = \Delta Q_n.n_{q_n} \tag{3.11}$$

It is noteworthy that the aforementioned analysis is under the strong assumption that the DG units are highly inductive due to the coupling inductor used in the DG interface. If the system is resistive, however, the equation will be given by (P–ω) and (Q–V) instead.

3.3 Formulation of Service Restoration Problem in Droop–Controlled IMG

The self–healing restoration process for IMG is formulated in this work as an optimization problem. The basic objective function of the restoration process include three main points. The first aspect is to maximize the number of restored loads L_F as in (3.12), while the second aspect is minimizing the number of switching operations N_{sw} as in (3.13). Finally, the last aspect is the minimization of the total losses in the system as in (3.14). The activation of the third objective is based on the duration time of the post-restoration configuration. If the new configuration is intended for a long term (i.e. days/weeks) or for a planned maintenance, that means a reconfiguration process is performed until a proper maintenance is achieved. Based on the above discussion, the basic objective function is presented as follow:

$$F_{RS}(L_F, N_{sw}, \Delta S) = f_1(L_F) + f_2(N_{sw}) + f_3(\Delta S)$$

$$f_1(L_F) = max. \sum L_x.J_x \qquad \forall x \in L_F, \tag{3.12}$$

$$f_2(N_{sw}) = min. \sum SW_b \qquad \forall b \in N_{sw}, \tag{3.13}$$

$$f_3(\Delta S) = min.\ \ RST. \sum \Delta S_{loss}^{IMG} \qquad RST \in [0, 1]. \tag{3.14}$$

where; L_x: The load at bus no. x, J_x: The binary decision whether the load at bus x is restored (i.e., $J_x = 1$: resorted, $J_x = 0$: not restored), L_F: The set of all de-energized loads, SW_b : representation of the switching operation in branch b (i.e., $SW_b = 1$: the switch state is changed, $SW_b = 0$: no change occurs in the switch state). ΔS_{loss}^{IMG} is the total IMG losses which needs to be calculated in case of a long term reconfiguration based on the binary index RST; where RST is set to 1 when the IMG is planned.

3.4 Constraints of the IMG Service Restoration Problem

The self–healing restoration process in the IMG is constrained by the operational limitations as mentioned in section 2.6. Such as, the power flow constraints in (2.27) and (2.28), voltage operational limitation in (2.30), and system rotational frequency in (2.29). In addition to the mentioned constraints, other limitations need to be considered in the restoration process. The operational requirements of DG units depend on their control schemes, which may vary with DG type, inverter control features, and network mode of operation. For instance, low penetration level of renewable based DG units (e.g. wind and solar) are usually uncontrolled and permitted to inject their maximum generated power to the grid. However, under the SDG paradigm, and with high DG penetration, a real time active and reactive power control for the smart inverters of DG units is expected. In such cases, the smart inverter might remotely and/or locally sets the active and reactive powers with respect to maximum generated power and inverter capacity. Hence, each DG inverter located at bus i and at time t injects active and reactive power as in (3.15) and (3.16). In the islanded mode of operation, the droop parameters of the DGs are calculated by (3.4) and (3.5), in which m_P and n_q must be greater than 0.

$$0 \leq P^t_{G,i} \leq S^{Cap}_{G,i} \tag{3.15}$$

$$\mid Q^t_{G,i} \mid \leq min\Big(P^t_{G,i}.tan[cos^{-1}pf^{min}_G], \sqrt{(S^{Cap}_{G,i})^2 - (P^t_{G,i})^2}\Big) \tag{3.16}$$

As shown in (3.15) and (3.16), the active power is limited to the DG inverter capacity $S^{Cap}_{G,i}$ and the DG reactive power is constrained by the DG minimum allowed power factor pf^{min}_G and the available reserve of the inverter capacity. It is noteworthy that the active power setting of renewable DG units is limited to the maximum power that can be extracted at each time instant, t. Additionally, every line power flow between the buses in the IMG have to be maintained in an acceptable limit for the flowing current to avoid the overloading as presented in (2.31). Also, the generated post–restoration network topology in distribution systems must have a radial structure. Therefore the system radial structure needs to be maintained in order not to defect the systems protection coordination schemes [20]. The radial structure constraint can be expresses as in (3.17).

$$N_{sw} \in radialstructure \tag{3.17}$$

3.5 Solution of the IMG Self–healing Restoration Problem Using Heuristic Techniques

Heuristic techniques are well-known for their abilities to solve multi-objective optimization problems. There are numerous heuristic techniques proposed in the literature such as, artificial neural networks [102], genetic algorithm [103], extended petri-nets [104], binary particle swarm [105], and fuzzy logic control [106]. Among those techniques, ant colony optimization (ACO) is one of the most superior mechanisms [107, 108, 109]. ACO is a stochastic population based heuristic algorithm which is equivalent to the behavior of the ant or bee in their colony in the real life

[110, 111]. ACO is widely used in solving the problem of self–healing restoration in active distribution networks. Given its superiority, ACO is selected in this work to solve the formulated optimization problem of self–healing restoration in IMG, where the out of service section finds its own restoration path as follows [112]:

$$\mathbb{P}_{ij} = \frac{\tau_{ij}^{\alpha}.\eta_{ij}^{\beta}}{\sum \tau_{is}^{\alpha}.\eta_{is}^{\beta}} \qquad s \in \daleth \tag{3.18}$$

where; $\mathbb{P}_{ij}$: The probability of the ant to move from point i to j, τ_{ij}^{α}: The quantity of remnant pheromone on the trail from i to j, η_{ij}^{β}: The desirability of the trail which is $1/distance$; α and β: The parameters that control the relative importance of the trail pheromone versus the desirability of the trail. $\daleth$: represent all the possible paths. When all ants have completed a tour, the pheromone trails are globally updated using the global pheromone-updating rule (3.19). The aim of the pheromone update is to increase the pheromone values associated with good or promising solutions, and to decrease those that are associated with bad ones based on (3.20).

$$\tau_{ij} = (1 - \rho)\tau_{ij} + \Delta\tau_{ij} \tag{3.19}$$

$$\Delta\tau_{ij} = \frac{Q}{L_S} \tag{3.20}$$

where, ρ is the evaporation of trail pheromone between i and j and $\Delta\tau_{ij}$ is the pheromone left on trail ij by current optimal solution given as in (3.20). In which, Q is constant value and L_S is the tour length of the ant S to the whole

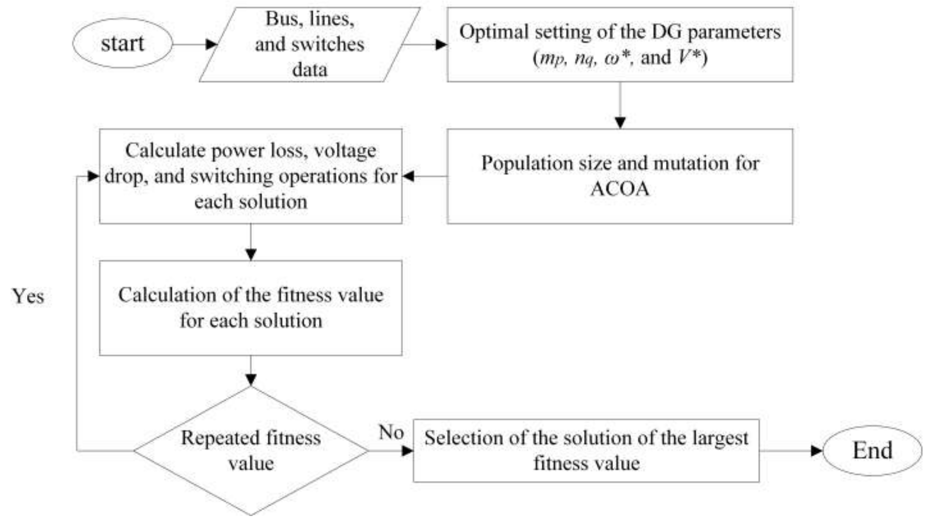

Figure 3.25: Flowchart for the proposed self-healing restoration process in IMG using ACO.

trip. The optimum solution is obtained; after a number of iterations, comparing the probability of each path with each other, and by choosing the one with the highest probability. The ACO is integrated to the self–healing restoration process which can be represented as in Fig 3.25.

3.6 Case Studies for the Application of ACO in Service Restoration of IMG

The 33–bus distribution test system depicted in Fig 2.11 has been used in this study to test the effectiveness of the proposed ACO self–healing algorithm in IMG to optimally restore the out of service loads with optimal setting of the droop

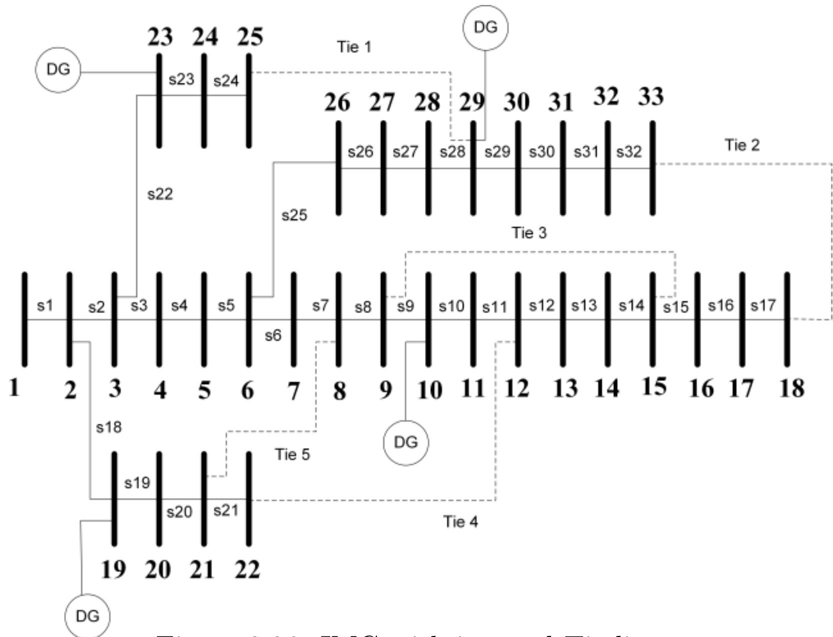

Figure 3.26: IMG with internal Tie lines.

parameters. Figure 3.26 is presented to illustrate the NO tie lines in the IMG, the tie lines are used to support the self–healing restoration process of the IMG in case of a fault. As shown in the figure, four dispatchable DGs are assumed to be installed at buses 10, 19, 23, and 29. All DGs are operating with fixed droop active and reactive power parameters. m_P and n_q, are selected to be 135×10^{-5} and 25×10^{-3} per unit, respectively. ω^* is set at 1 per unit for all DGs with a base value of 60 Hz.

Two case studies are carried out to validate the effectiveness of the proposed optimization model for IMGs. The first case study is conducted to assess the impacts of optimal droop parameters setting on the operation of IMGs during

Table 3.3: Droop parameters for installed DGs in IMG.

	Equal Droop parameters				Optimal Droop parameters			
DG location	10	29	23	19	10	29	23	19
m_P	135×10^{-5}				7×10^{-4}		95×10^{-5}	8×10^{-4}
n_q	25×10^{-3}				125×10^{-4}		16×10^{-3}	145×10^{-4}
ω^*	1				1.0044	1.0001	1.0073	1.0067
V^*	1.01				0.9856	1.01	0.9895	0.9956
Total IMG losses	0.111 MVA				0.106 MVA			
Min. Voltage occurred	0.951				0.97			

normal operation (i.e. no fault). Without loss of generality, the objective function in the normal mode of operation aims to minimize the IMG system losses; where $f_1(L_F)$ and $f_2(N_{sw})$ are deactivated. In the second case study, service restoration process in IMG is performed considering the optimal settings of droop parameters. The second case study is assumed to perform a reconfiguration that last for a long period of time, in order to consider the third term of the basic objective function (i.e. total IMG losses). By applying the proposed ACO algorithm in normal operation, the optimal droop parameters for power sharing are altered. The change of the droop parameters is shown in Table 3.3 in addition to the total system power loss and the minimum occurred voltage in both settings.

As noticed in Table 3.3, the total MVA losses for IMG decrease when applying

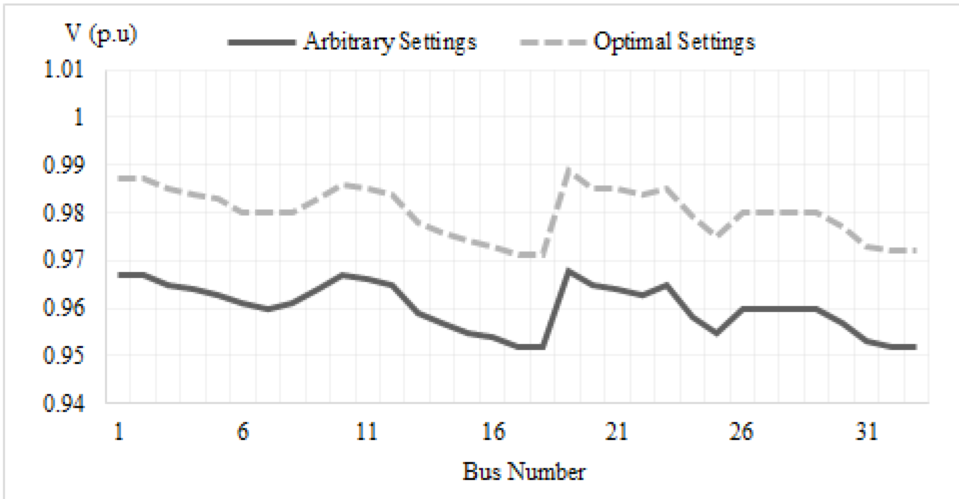

Figure 3.27: Voltage profile of the IMG during normal operation.

the proposed ACO algorithm in addition to an increase in the minimum voltage level occurred in the system. Figure 3.27 shows the voltage profile of the IMG between equal and optimal settings of the droop parameters. The results show that optimal power sharing of droop–controlled DG units reduces the system losses and enhances the voltage profile significantly.

In the second case study, it is assumed that a fault occurs between bus 10 and bus 11, where the loads from bus 11 to the downstream is out of service and need to be restored. According to the topology of the studied system, it can be noticed that Tie 2, 3 and 4 are only the candidate paths in order to restore the faulted area, where only one switching operation of them can be used to satisfy the restoration problem. However, when the losses minimization is taken into account, there might be several required switching actions. To determine the optimal switching actions for maximizing the load restoration, minimizing the switching operation, and satisfying the operation constraints, the proposed ACO needs to be executed. After the occurrence of the faulted area, the restoration process is carried out by the ACO to choose from different switching actions to restore the faulted area, which can help the DNO to take appropriate decision. The challenge in the self–healing restoration process which will remain for a long periodic time, is thus prevailing in taking an optimal decision that is a trade–off between the minimum losses and the number of switching operations, where as the number of switching operation increases the total cost of the restoration process is also increased. A limit of 3 switching operations have been assumed in order to study the impact of switching operation number on the solution of the optimization problem. In this case study, the restoration is performed and compared by using arbitrary and optimal droop parameters (i.e. For each candidate solution (i.e. configuration), a nonlinear optimization problem is solved to determine the droop settings of DG units). Table 3.4 shows the results of the self–healing restoration process for both equal and optimal settings of the droop parameters under different reconfiguration options. Figure 3.28 shows the voltage profile in the two case studies with different switching operation.

Table 3.4: Results of the proposed self-healing restoration in IMG.

<table>
<tr><th colspan="2">Points of comparison</th><th>1 Switching Operation</th><th>2 Switching Operations</th><th>3 Switching Operations</th></tr>
<tr><td rowspan="2">Total MVA Losses</td><td>Arbitrary Setting</td><td>0.1139 MVA</td><td>0.1139 MVA</td><td>0.11253 MVA</td></tr>
<tr><td>Optimal Setting</td><td>0.109713 MVA</td><td>0.1089 MVA</td><td>0.1075 MVA</td></tr>
<tr><td rowspan="2">Min. Voltage Level</td><td>Arbitrary Setting</td><td>0.951 p.u.</td><td>0.949 p.u.</td><td>0.948 p.u.</td></tr>
<tr><td>Optimal Setting</td><td>0.9708 p.u.</td><td>0.9696 p.u.</td><td>0.9675 p.u.</td></tr>
<tr><td rowspan="2">Switching Actions</td><td>Arbitrary Setting</td><td rowspan="2">Close: Tie 3</td><td rowspan="2">Close: Tie 3
Open: s22</td><td rowspan="2">Close: Tie 1, Tie 3
Open: s26</td></tr>
<tr><td>Optimal Setting</td></tr>
</table>

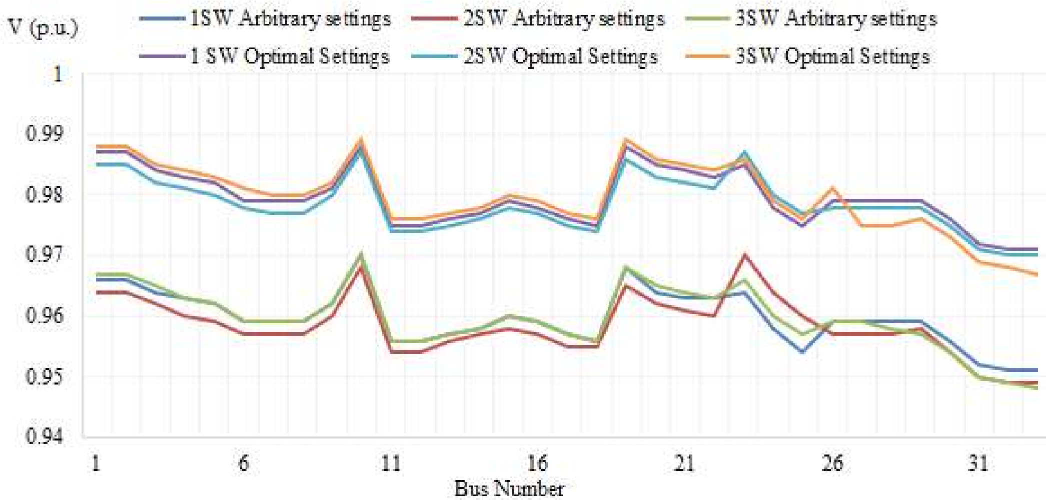

Figure 3.28: Voltage profile for all restoration scenarios.

As shown in the results, the optimal power sharing among the droop–controlled DG units in IMG will enhance the system losses. Further, as depicted in the results, the voltage profile for the buses has been significantly improved. As shown in Fig 3.28, the minimum voltage occurred in all switching scenarios in the optimal droop settings is within the range of the voltage constrains. However, in some switching operation scenarios, in the equal arbitrary droop parameters study, the voltage magnitude violated its lower bound, which is a critical state for the total system. The DNO can use the obtained results to compromise between the total losses and the cost of the switching operation. A key factor that needs to be taken into account in the self–healing restoration process is the time of execution. Where, it is critical to restore the faulted loads as quick as possible. In the proposed algorithm, the number of iterations that has been taken in this process to restore the loads was found to be 9 iterations for the ACO to take the decision in all possible switching actions, and 3 to 12 iterations for the power flow for every nominated configuration for the system. The processor used to conduct the simulation was Intel® Core ™2 Duo CPU P8700 @ 2.53 GHz with system type of 32-bit operating system and the installed memory was 4.00 GB.Where at this specs the duration time taken from the ACO to propose the suitable configuration was 115.25sec. The obtained execution time of the proposed self–healing restoration process is acceptable to the microgrid operator in order to do the switching actions in the system.

3.7 Automatic Restoration in SDG Considering Different Energy Transfer and Creation of new IMGs

In SDGs, several electric power system areas can form microgrids capable of operating either parallel to or isolated from the main grid. In this regard, a new centralized control scheme for automatic back–feed service restoration in SDGs clustered into microgrids is proposed. The central features that differentiate this work from the literature are: 1) using DG units as alternative supply configuration; where three types of energy transfer between the adjacent feeders are introduced (load, DG and load/DG); 2) the creation of IMGs via optimal DG and load transfer actions; 3) the simplicity of the proposed algorithm. The proposed algorithm takes into consideration the load variability in different feeders during the fault occurrence and the system operational constraints.

3.7.1 Power Transfer Mechanisms in the Restoration Process

The widespread implementation of DG units in distribution networks has created microgrids with sufficient generation capacities to meet all, or most, of their local demands [113]. Microgrids are regarded as the building blocks of SDGs, since they may offer multiple potential benefits for customers, DG owners, and utilities. The network configuration for each microgrid can be identified based on the zone in which the devices that allow separation of a microgrid from the electric power system are located. Figure 3.29 shows an example of a SDG configured into multi–microgrids. As depicted, each microgrid consists of a group of components (e.g., distribution feeders, DG/storage units, and loads) with an isolation switch at its point of coupling with the main power grid. Each microgrid is capable of operating in both grid–connected and islanded modes. Adjacent microgrids are tied through NO switches. Most distribution networks have a radial structure, where loads are normally fed from one substation through a distribution feeder. However, in order to increase customer service reliability, distribution feeders, supplied from different substations, are tied together normally via open switches, (i.e. redundancy). These

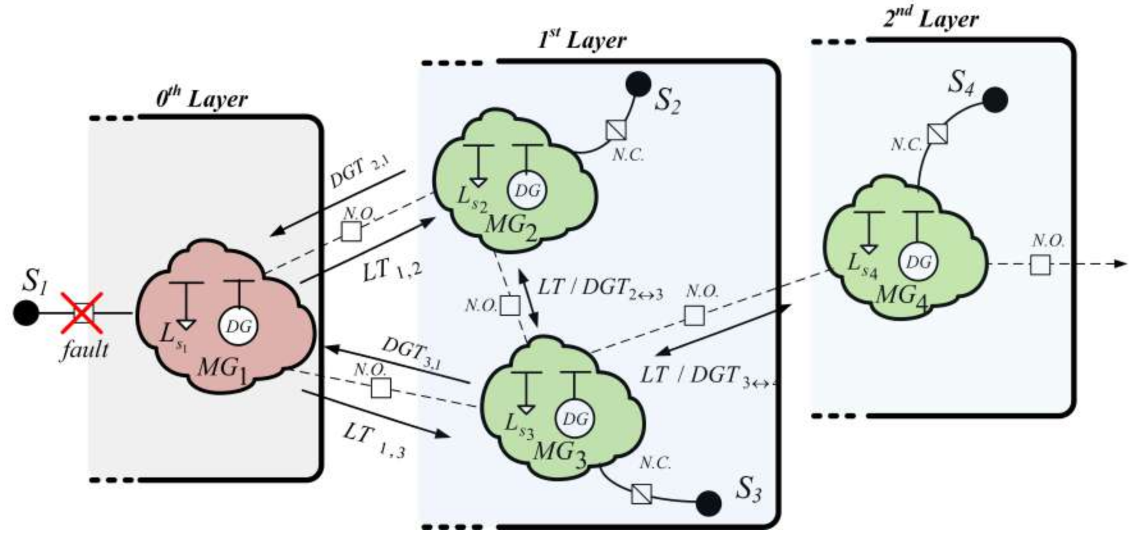

Figure 3.29: Typical structure of a SDG configured using multi-microgrids transferring different types of power support.

switches allow customers to be back–fed from an alternate source/substation during an outage affecting their main substation. This reconfiguration process can be achieved in the form of a single–path restoration, in which the potential back–feeding source (i.e., adjacent source directly tied to the faulted feeder), can provide the required power, from a single path, to the load [114, 115].

However, in some severe conditions (e.g. storms), the capacity of the adjacent source may be limited, and multiple back–feeding sources (i.e. multi–path restoration) may be required to reach a feasible solution for the restoration problem [116]. In such conditions, the non served load may have to be split into two or more load zones, in order to be fed from multiple sources and maintain the radial structure. In order to prevent load shedding, the back–feeding source(s) can increase its available power by transferring part of its loads to its unfaulted adjacent source(s) (this process is known as load transfer [116, 117]). Here, a supporting feeder can disconnect a portion of its local load and transfer it to another adjacent supporting feeder via the tie line between them, in order to reduce local loading and thus offer an adequate surplus of power to help restore the supported feeder. This, in turn, introduces the concept of a multi–layer restoration, where the switches that tie the un–served load area with its back–feeding sources are called the first layer of tie switches for load restoration. The second layer of tie switches binds the back–feeding sources and their adjacent sources. In SDGs, the integration of high DG penetration in distribution systems can be utilized as an alternative supply configuration. DG units can be transferred between microgrids in order to increase available power and reduce load shedding [118]. In addition, with an appropriate sequence of switching, the creation of (a) post–restoration IMG network(s) may create a feasible solution for solving the restoration problem. Based on the aforementioned discussion, three types of power transfer between microgrids, during the restoration process, are introduced in this work: load transfer (LT), DG transfer (DGT), and a mix of load/DG transfer (LT/DGT).

As shown in Fig 3.29, when the source S_1 is disconnected, the out of service loads in MG_1 can be restored either in single–path, multi–path or multi–layer switching schemes. For instance, a single–path restoration solution is feasible when either MG_2 or MG_3 (i.e. back–feeding microgrids) can provide the required power for the non served loads. When a single–path solution is infeasible, a multi–path restoration maybe needed. In such cases, both MG_2 and MG_3 pick up the un–served loads by splitting them via internal zone switching. In the case of infeasible solutions, the restoration process requires a multi–layer scheme, in which MG_4 can contribute to MG_2 and MG_3, by increasing their remaining capacity. Another viable solution, under the SDG paradigm, is to create an IMG in the zone of the un–served load by transferring DG units from MG_2 and MG_3. The proposed control scheme is a centralized control, assuming that the DNO have a total knowledge of information of each feeder near by the faulted area. The DNO can run the simulation power flow for every supporting feeder individually by installing a dummy load at the end of the tie line, in order to calculate the maximum reserved capacity for every feeder that can be supplied for the installed dummy bus. The DNO now can know the MVA for every supporting feeder that can be transferred. The main possible solution of the service restoration in conventional distribution systems is to restore the out–of–service load zone using a potential back–feeding source via the installed NO tie switches [66]. The restoration could be in the form of a single–path restoration, when a potential back–feeding sources able to provide the required power over a single path to the out-of-service load zone.

The problem of automated restoration is formulated as a mixed integer nonlinear optimization problem. The objective function reflects mainly the total cost of the restoration process including the costs of load interruption and switching operations [68], also taking into consideration that the losses in the total restored system is not a major factor to be added in the objective function since the aim of the restoration process is to deliver the service for the faulted loads, the objective function can be formulated as follows:

$$min.\Big(\sum_{i=1}^{L_F} CIC_i + \sum_{sw=1}^{SOC_T} C_s w \mid x_{sw,t} - x_{sw,t+1} \mid + \sum_{k=1}^{N_T} \mid T_{k,t} - x_{k,t+1} \mid\Big) \tag{3.21}$$

where; CIC_i is the cost of customer I interruption from the total faulted loads L_F, SOC_T is the total number of internal automatic switches of each supply, C_{sw} is the cost of changing the switch status time t to $t+1$; N_T is the total number of tie line switches, C_k is the cost of changing the state of each tie line switch from time t to $t+1$.

As discussed before, any distribution system operates under the safety constraints that must be taken into consideration when creating new configurations of the system even in the normal condition without any fault. These constraints are set to maintain the system stability in over or under loading. The objective function is subjected to different constraints depending on the mode of operation of each created network in the restoration algorithm. These constraints include the voltage level at each node (2.30), generation capacity of the DGs (3.15) and

(3.16), and feeder line capacity (2.31). The power flow operational constraint as in (2.27) and (2.28) in case of IMG or the creation of a new IMG in addition to the frequency constraint as in (2.29). Additionally, the connection between microgrids is considered in the constraints to prevent any violations after the restoration process. Power transfer between adjacent sources is limited by the capacity of the NO tie lines given in (3.22).

$$S_{i,j_T} \leq Tie_{i,j_{cap}} \tag{3.22}$$

where, S_{i,j_T} is the transferred MVA from feeder i to feeder j and $Tie_{i,j_{cap}}$ is the tie line capacity that can accept the transfer from feeder i to feeder j. Technically (3.22) is the major constraint that must be considered in both load and DG power transfer. Also, the generated post–restoration network topology in the distribution systems must have a radial structure. Therefore the system radiallity needs to be maintained as in (3.17). The proposed control strategy measure the radiallity constraint by taking into account any of a circulating current in the created structure [71]. The updated radiallity constraint considering the tie lines can be expresses as in (3.23),

$$(SOC_T + N_T) \in radialstructure \tag{3.23}$$

As explained above, in addition to the LT, the integration of high DG penetration in distribution systems can also be utilized as an alternative supply configuration. DG can be disconnected from its main/normally-predefined microgrid and connected to an adjacent microgrid to increase the surplus power of the adjacent one, and thus maximize restored loads. This process is called "DG transfer between microgrids." This process of DG transfer between microgrids might be limited to some technical operation constraints set by the utility, e.g. protection coordination, feeder capacity/loading limits, and specified voltage and reactive power control requirements [118]. Hydro One, for instance, a transmission and distribution company, located in Ontario Canada, sets a limit of less than 251 kW for the capacity of each single DG unit in order to allow for transfer ability [118]. Figure 3.30 illustrates the DGT between different feeders. As shown in Fig 3.30(a), each microgrid has its own set of different DG capacities at normal system configuration. However, in the case of any alternative reconfiguration, as in Fig 3.30(b), the allowed DGT from MG_1 to MG_2 or MG_3 is limited to the 240 kW DG. It is worth noting that the total allowed DGT from MG_2 to MG_1 is 500 kW i.e., 2 units x 250 kW. Also, as shown in the figure, DGT from MG_3 is not allowed, as the individual capacity of each DG unit exceeds the allowed transferable limit. The DGT limit can be modeled as:

$$TR_{G(i)}^{k,l} = \begin{cases} 1 & \forall S_{G(i)}^{Cap} < S_{DGT,lim}^{k,l} \\ 0 & otherwise \end{cases} \tag{3.24}$$

where, $TR_{G(i)}^{k,l}$ is a binary variable for the status of transfer for DG i, between two adjacent feeders, k and l (i.e. one is transferable and zero, otherwise); and $S_{DGT,lim}^{k,l}$

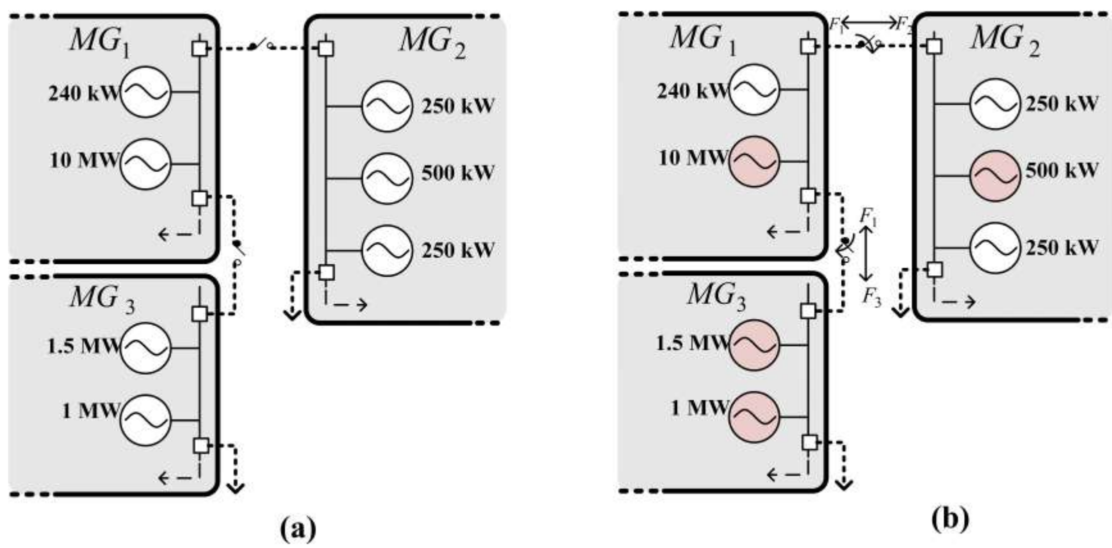

Figure 3.30: Different DG transfer among different microgrids.

is the allowed limit of DG transfer between the two feeders.

3.7.2 Case Study for the Proposed Centralized Automatic Restoration of SDG Clustered into Microgrids

In order to test the effectiveness of the proposed automated restoration, simulation studies have been carried out in MATLAB environment on the 70–bus distribution test system [119] as shown in Fig 3.31, the system has four substations, T1, T2, T3, and T4 with the following assumptions: scheduled maintenance is assumed at T4 and its feeder has enough DG units to operate in islanded mode of operation (i.e. scheduled IMG). The capacities of T1, T2, and T3 are 2, 2.5, and 2.5 MVA, respectively.

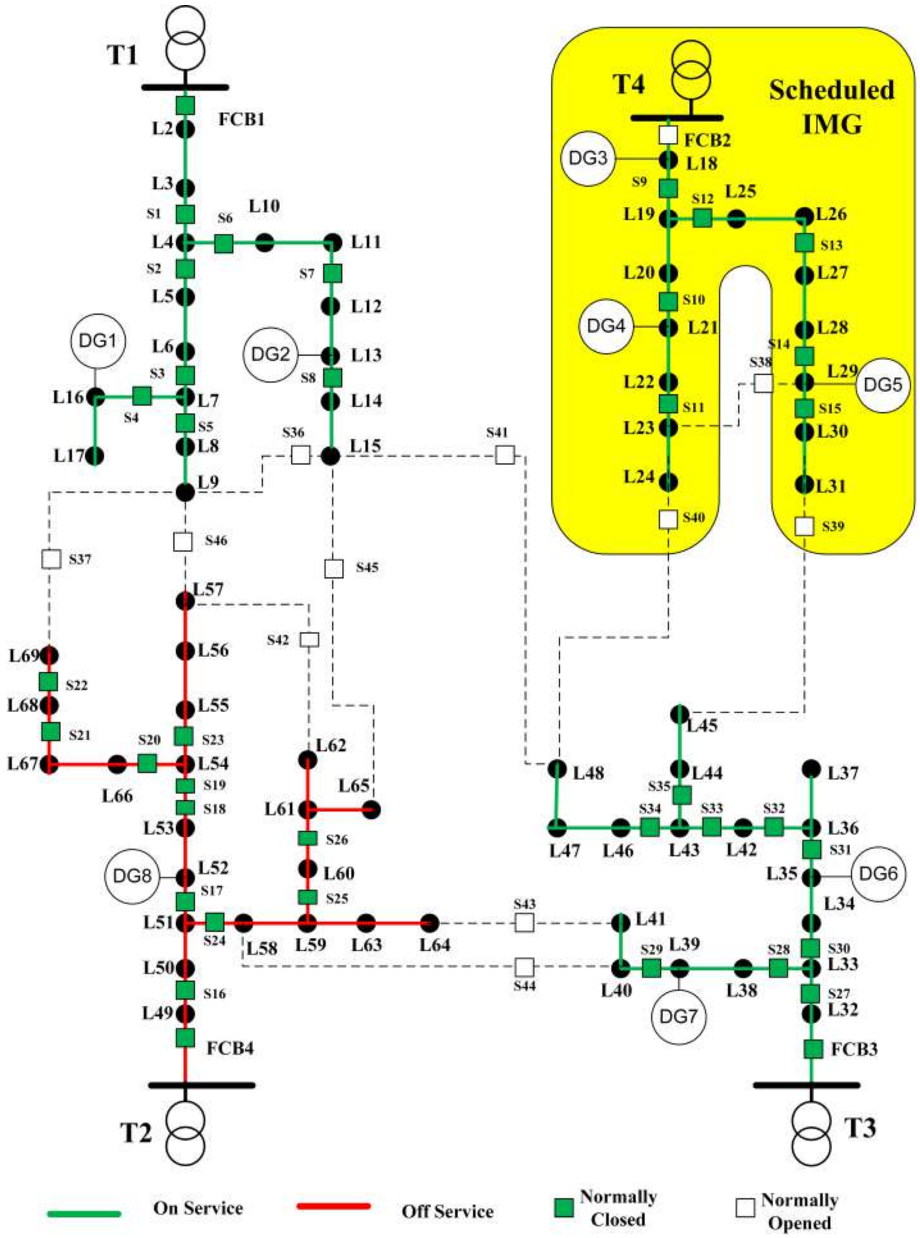

Figure 3.31: 70 Bus system represented as a SDG clustered into four microgrids.

Table 3.5 show the sizes and droop gain parameters of the DG units assumed in the system. It is noteworthy that the droop gains are utilized when the DG units operate in islanded mode to control the system frequency and voltages. In grid–connected mode, the installed DG units are assumed to operate in PQ mode with unity power factor. As for the loads in this system, different types of loads (i.e. residential, commercial and industrial) have been considered in order to assign the load priorities according to the customer interruption cost (CIC). In the pre–fault condition, the system was fully functional where each feeder was working separately without connection with its adjacent feeders, as shown in Fig 3.31 (i.e. all tie switches were opened). The minimum voltage during the pre–fault condition in the system was found to be 0.97 per unit.

Table 3.5: Different Installed DGs in the Total system with the Rated Capacity.

DG Number	Rating MVA Capacity	Droop Parameters in IMG			
		m_P	n_q	ω^*	V$\hat{}$*
3 and 6	1	0.0027	0.05	1	1.02
1, 2, 4, 5, and 7	0.5	0.0054	0.1	1	1.03
8	0.25	0.0108	0.2	1	1.02

During a full loading condition, a fault is assumed to occur at T2. The repair time of the fault is assumed to be 2 hours. The installed DG8 at this feeder will not be applied to restore all the faulted loads in this feeder taking into consideration the critical loads that are connected on this feeder, four restoration scenarios have been conducted in the aforementioned condition. In the first scenario, it is assumed that only single–path restoration is allowed using T1, T3 individually. In the second scenario, a multi–path restoration process is achieved by using the back–feeding supplies T1, T3 With each other in order to increase the total restored loads with the system reliability. Finally in the third and fourth scenarios are proposed using the multi–layer restoration using all the available (back–feeding/ adjacent) feeders, where in the fourth scenario the creation of the IMG is proposed, in Table 3.6 DNO can obtain the remaining power for each feeder.

Table 3.6: The Remaining Capacity for each feeder.

	Capacity Limit MVA	Actual Generation MVA	Remaining Capacity MVA
T1	2	1.1262	0.8738
T2	2.5	2	—
T3	2.5	1.86	0.64
T4 Scheduled IMG	2	1.1405	0.8595

First scenario of the single path restoration from either T1 or T3 cannot achieve the full restoration since the available power capacity of each feeder individually is much less than the requested restoration power in T2, therefore the DNO will search for more restoration scenarios. In Table 3.7 the difference between the restoration layers is presented, as illustrated in the proposed algorithm. In the multi–path restoration the DNO use only the back–feeding supplies without considering the adjacent supply IMG. One of the other relaxations to the system to overcome the fault occurrence is reducing the minimum limit of the voltage that will occur in the neighbor feeders to 0.9 per unit voltage, which is acceptable in the distribution systems under the critical conditions. As shown in Table 3.7, the multi–path restoration was sufficient in the total cost and the minimum losses occurred in the system while there are a tremendous number of loads out of restoration process due to the power adequacy with the major constraints.

On the other hand, in order to increase the system reliability, the DNO will restore the faulted area using the multi–layer restoration considering the adjacent supplies. As shown in Fig 3.31 the IMG is directly connected to T3 where the DNO starts to optimize the operational condition between them in order to increase the available capacity that can be finally transferred to T4. In Table 3.7 it is noticeable that the number of total restoration cost is decreased with the increase of the switching operation while on the other hand the number of un–restored loads decreased which can be seen in the CIC of the restoration process.

Table 3.7: Restoration process with different feeders.

Operation	Multi-Path Restoration	Multi-Layer Restoration	
		without IMG Creation	IMG Creation
Switching Operation	Close: S43, S46 Open: S17, S20, S24	Close: S40, S43, S46 Open: S17, S19, S20, S33	Close: S36, S40, S43, S46 Open: S3, S8, S17, S22, S33
Power Loss	0.102 MVA	0.135 MVA	0.131 MVA
Min. V	0.917 p.u.	0.944 p.u.	0.966 p.u.
Switching Cost	$ 253.75	$ 355.25	$ 456.75
Elapsed Time	2.6602 Sec	4.0961 Sec	3.7319 Sec
Not served loads after restoration	L49, L50, L51, L66, L67, L68, L69	L68, L69	L69
CIC	$ 9,892	$ 2,779	$ 1,621
Total Cost	$ 10,146	$ 3,134	$ 2,078

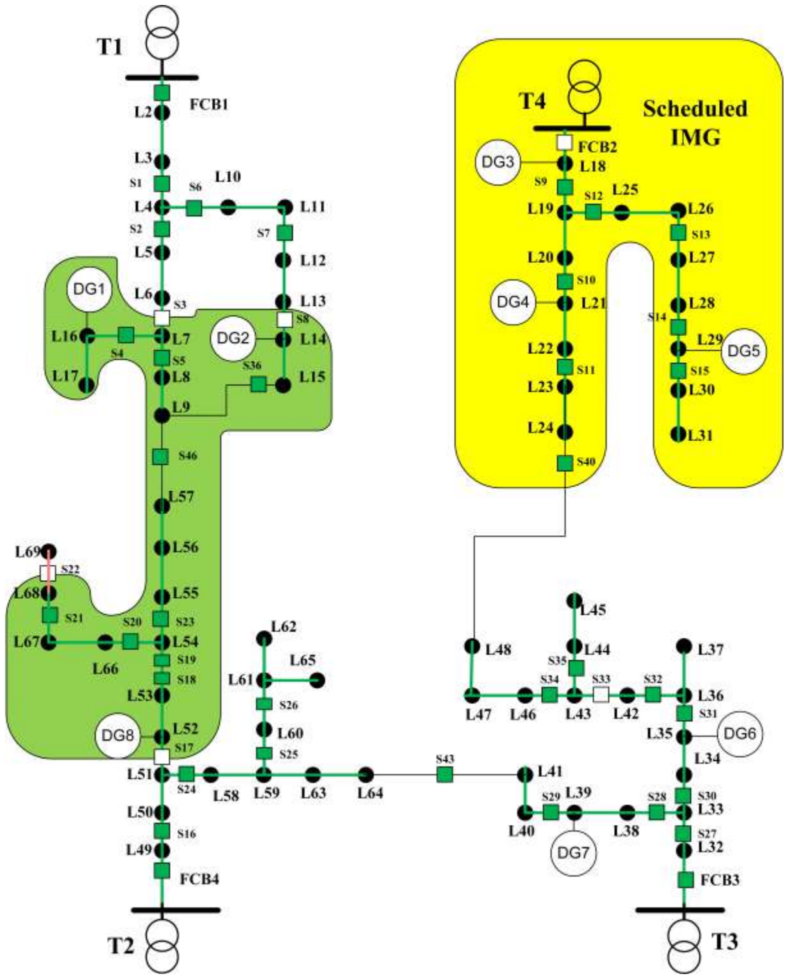

Figure 3.32: New configuration yield from multi-layer restoration process with creation of IMG.

Finally in order to increase the restoration percentage, the DNO will operate on the formation of a new IMG in the faulted area which can be achievable based on the proposed method by checking Table 3.5 with the capacity of the installed DGs. For example, in T1 the total available capacity was 0.8738 MVA that can be transferred through the capacity of the tie lines and as for the installed DGs 1 or 2 with a capacity of 0.5 MVA, which means the acceptance of DG transfer condition. In order to formulate the new IMG, in Table 3.7 it can be noticeable that the restoration process cost is slightly decreased due to the decrease of the number of un–restored loads. Also, it can be observed that the total MVA losses have been decreased due to the new created networks (i.e. configurations) and the formation of a new IMG. Figure 3.32 shows the system post–restoration networks using the proposed algorithm. As shown in the figure, the concept of DG transfer and creation of IMGs generated a feasible solution for the restoration problem.

3.8 Summary for the Automatic Centralized Restoration Proposed Algorithm

In this chapter, centralized optimization algorithms are proposed for self–healing service restoration of SDGs. The developed algorithms take into account the special characteristics and operation philosophy of droop–controlled IMG system, allowing different types of energy transfer between adjacent microgrids, and facilitate the creation of new (not predefined) IMGs in order to maximize the restored loads during emergency conditions. The formulated problems consider other aspects such as the number of switching and the system losses. Two different operational control schemes (without and with optimal power sharing) have been implemented in the proposed algorithms to account for the impacts of the selection of the droop parameters on the enhancement of the IMG restoration process. The problem has been formulated as a mixed integer nonlinear optimization. The ACO has been utilized to solve the optimization problems. Several case studied have been carried out to validate the efficacy of the proposed optimization models.

Chapter 4 - Multiagent Back–Feed Power Restoration using Distributed Constraint Optimization in SDGs Clustered into Microgrids

In this chapter, a distributed optimization problem is formulated for the automatic back–feed service restoration in SDGs. The formulated problem relies on the structure of SDGs, clustered into multi–microgrids, capable of operating in both grid–connected and islanded modes of operation. Similar to the work in chapter 3, the three types of power transfer presented between the neighboring microgrids, during the restoration processes are taken into account: load transfer, DG transfer, and combined load/DG transfer. Also, the formulated optimization problem takes into account the ability of forming new, not predefined IMGs, in the post–restoration configuration, to maximize service restoration. To obviate the need for a central unit, the optimization problem is reformulated in this chapter as a distributed constraint optimization problem, in which the variables and constraints are distributed among automated agents. To reduce the problem complexity, the restoration problem is decomposed into two sequential and interdependent distributed sub–problems: supply adequacy, and optimal reconfiguration. The proposed algorithm adopts the Optimal Asynchronous Partial Overlay (OPTAPO) technique, which is based on the distributed constraint agent search to solve distributed sub–problems in a multi–agent environment.

4.1 Formulation of the Distributed Constraint Optimization Problem

The problem formulation is based on a distributed optimization problem, in which the variables and constraints are distributed among automated agents [120]. In a distributed optimization environment, each agent has its own agent–view, which stores its variable assignment, domain, constraints, and algorithm procedures. The solution philosophy of distributed optimization problems adopts a multi–stage negotiation protocol among the automated agents, via two-way communication channels [77, 121]. Figure 4.1 shows a schematic diagram of the proposed distributed control structure for SDGs. As shown in the figure, each microgrid is connected to an adjacent microgrid(s) at the point of coupling through a NO switch. Each microgrid control agent updates its agent–view by estimating the power adequacy of its

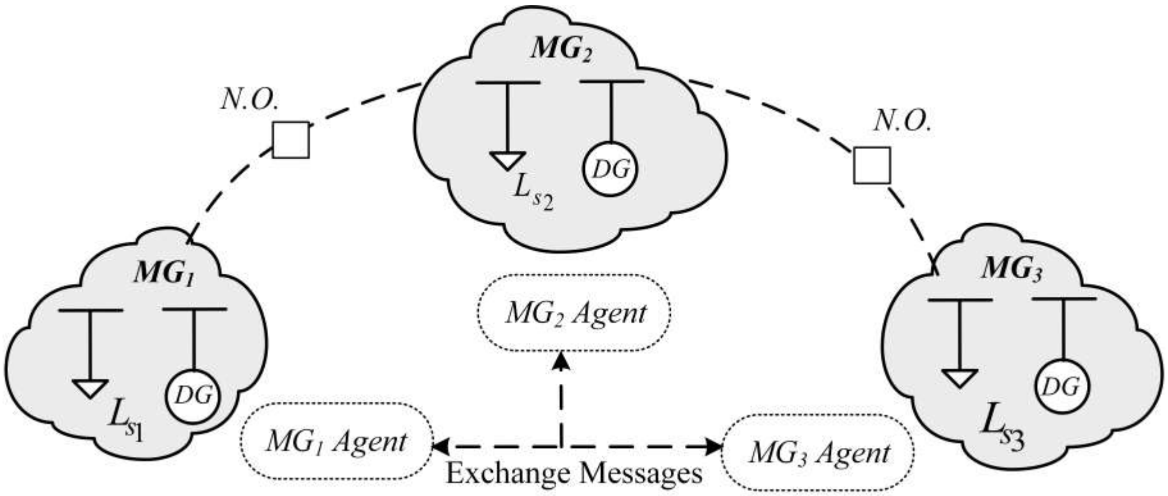

Figure 4.1: Schematic diagram of the distributed control structure between microgrids

assigned microgrid, each time it receives information. In order to implement a distributed control scheme, a two–way communication network needs to be deployed to facilitate the exchange of messages between control agents. The communication network is modeled as a directed graph given as [77, 120]:

$$G = (v, E, \Lambda) \tag{4.1}$$

where, $v = (v_1, \ldots, v_H, \ldots, v_{n_{MG}})$, is a set of nodes at which location the control agents are connected in the SDG, and $E \subseteq v \times v$ is the set of directed edges that describes the communication links between the control agents. An edge $(v_H, v_K) \in E$, denotes that control agent H can obtain information from control agent K, but the inverse in not necessarily true. Λ is an $n_{MG} \times n_{MG}$ adjacency matrix; where $\Lambda = [\lambda_{HK}] \in \Re^{n \times n}$ with λ_{HK} equals one, if $(v_H, v_K) \in E$, and zero, otherwise. Also, in order to align with the literature, self–loops are not counted in E, i.e., $\lambda_{HH} = 0$. The in–neighbors of control agent H, are those eligible to send data to H, and are represented as $\aleph_H^{in} = [l \in \nu : (l, H) \in E \; and \; l \neq H]$. Further, the out–neighbors of control agent H, are those eligible to receive data from H, and are represented as $\aleph_H^{out} = [l \in \nu : (H, l) \in E \; and \; l \neq H]$ [122]. Given that a two–way communication is deployed, it is assumed, in this work,that $N_H^{in} = N_H^{out}$. It is noteworthy that this communication model is totally independent of SDG structure, and the locations of microgrids; however, a communication optimization problem can be adopted to minimize the exchanged messages path and the duration of the solution set points of the microgrids [122].

In order to reduce the restoration complexity, the formulated optimization problem is split, in this work, into two sequential distributed optimization problems: distributed supply adequacy assessment (DSAA), and distributed optimal reconfiguration (DOR).

4.2 Distributed Supply Adequacy Assessment (DSAA)

This problem aims to allocate resources for the out–of–service loads via a mediation process between the microgrid control agents (μA). To that end, the control agents are classified into two categories: supported and supporting. Supported agents are the microgrid control agents in which the un–served loads exist. In this stage, each supported agent (μA_x) determines the required load $S_{F_x}^{Max}$ that needs to be restored, which is equivalent to the difference between the total load and the available generation capacity. Also, a slack variable that acts as a fictitious generator A_{F_x}, is defined. A_{F_x} represents the amount of un–served/curtailed load, in case the reconfiguration process cannot completely restore the entire power demand. Hence, A_{F_x} can be defined as:

$$A_{F_x} = min[S_{F_x}^{Max}, \sum TL_{k,x}^{Max}] \qquad \forall x \in X \tag{4.2}$$

where, $x \in X$ and X is the set of supported microgrids; $TL_{k,x}^{Max}$ is the maximum back–feeding power transfer from any adjacent microgrid h.For each supporting agent μA_y, a generation variable A_{P_y}, representing the energy transfer to support μA_x is defined as:

$$A_{F_y} = min[S_{F_y}^{Max}, \sum TL_{k,y}^{Max}] \qquad \forall y \in Y \tag{4.3}$$

where $y \in Y$; and Y is the set of the supporting microgrids; $S_{P_y}^{Max}$ represents the difference between the available generation capacity and load. As depicted in (4.3), A_{P_y} is limited to the power capacity $TL_{k,y}^{Max}$ for each tie line between microgrid y and its adjacent microgrids h, where h can be a supporting or supported microgrid for x/y. Based on the above discussions, the DSAA problem for each supported agent can be formulated mathematically, as follows:

$$min. \sum_{x \in X} A_{F_x} \tag{4.4}$$

$$Subjected\ to = \begin{cases} \sum_{y \in Y} TL_{k,y} + A_{P_y} = 0 \\ \sum_{x \in X} TL_{k,x} + A_{F_x} = S_{F_x}^{Max} \\ 0 \leq A_{P_y} \leq S_{P_y}^{Max} \\ 0 \leq A_{F_x} \leq S_{F_x}^{Max} \end{cases} \tag{4.5}$$

At this stage, the μA_x can solve (4.4) and (4.5) to minimize the A_{F_x} and generate/send the assessment for all of the μA_y with the required MVA A_{P_r}.

4.3 Distributed Optimal Reconfiguration (DOR)

After execution of the DSAA, each μA_y knows the optimal amount of supporting energy that needs to be assigned to maximize load restoration. The second stage, (i.e., DOR), sets the obtained tie line energy transfer from the first stage, as power transfer constraints, between the adjacent microgrids. Then, it determines the minimum number of internal switching to satisfy: 1) the system operation constraints; and 2) the defined power transfer constraints. To that end, a decomposition technique is proposed in this work. The proposed technique relies on the existence of a

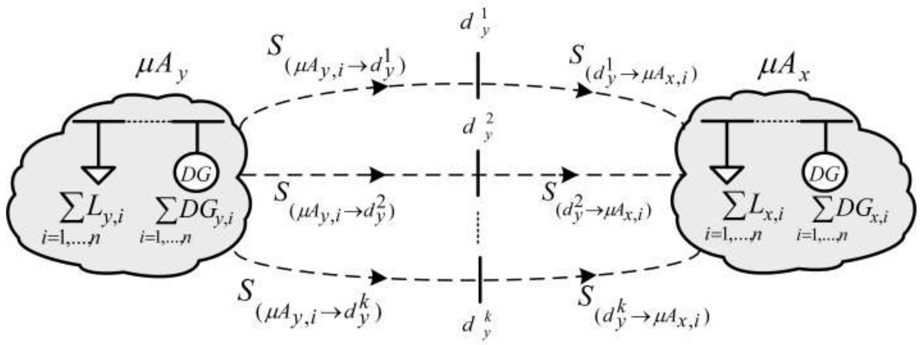

Figure 4.2: The Proposed DOR stage

dummy bus located between the adjacent microgrids, that are supposed to be tied, as shown in Fig 4.2.

The dummy bus identifies the boundary between two adjacent microgrids (i.e., point of microgrids coupling). This bus is typically defined at the point where the NO tie–line switch is located (i.e., zero injection bus). The location of the dummy bus determines the information that needs to be exchanged between the adjacent agents. Hence, the definition of a dummy bus is used to decompose the optimization problem [123]. In fact, the theory of defining a dummy bus to decompose the optimization process for large power systems, has been proposed in previous works, for the purpose of handling daily generation scheduling problems [124, 125, 120]. Also, several methods have been proposed in the literature to optimal power flow problems that are applicable to large interconnected power systems, and are suitable for distributed implementation. Two basic approaches were established, enabling the coordination of various areas in a multi–area system [126]. One of these approaches is decomposition, based on passing adjacent variables, where a fictitious dummy bus is defined between two areas. The dummy bus is defined to provide the necessary shared variables,written as follows:

$$d_y^k = [S_{d_y^k}, V_{d_y^k}, \theta_{d_y^k}] \qquad \forall k \in TL_k \tag{4.6}$$

The dummy variables consist of the voltage $V_{d_y^k}$, angle $\theta_{d_y^k}$, and power $S_{d_y^k}$ at the dummy bus for each feeder. These variables represent the power transferred from μA_y to μA_x. In the DOR stage, the objective function can be defined as follows:

$$min.f(X_{sw}, \tau_i) = \sum_{t=1}^{T} \sum_{i=1} \big(k_w.(SW_{f_y} + TL_k) + k_B.\widehat{d}^d_{S_{f_y}}\big) \qquad \forall k \in TL_k, i \in n_{bus} \tag{4.7}$$

where, k_w is the weighting factor for the total switching operation in μA_y, k_B is the weighting factor necessary to minimize the shared VA $\widehat{d}^d_{S_{f_y}}$ at d, which is divided into active and reactive shared power (i.e. $\widehat{d}^d_{P_{f_y}}$ and $\widehat{d}^d_{Q_{f_y}}$, respectively). As depicted in (4.7), the objective function contains two parts; the first, is the minimization of the total switching operation in μA_y to transfer the required amount of A_{P_r}. The second, is the term needed for coordination between the μA(s), which consists of the Lagrangian multipliers k_B, and the necessary shared variables at the fictitious bus of both cooperated microgrids. The DOR's objective functions are subjected to internal constraints in addition to the following:

$\forall y \in Y, k \in TL_k \Rightarrow$

$$A^y_{P_r} \leq \overline{A}^y_{P_{r,max}} \tag{4.8}$$

$$DGT_{y,x} + LT_{x,y} = A^y_{P_r} \tag{4.9}$$

$$\widehat{d}^d_{P_{fy}} = -P_{\mu A_{y,i},d^k_y} - P_{\mu A_{x,i},d^k_y} \tag{4.10}$$

$$\widehat{d}^d_{Q_{fy}} = -Q_{\mu A_{y,i},d^k_y} - P_{\mu A_{x,i},d^k_y} \tag{4.11}$$

The constraint in (4.8) presents an indicator for each μA in order to relax the required energy transfer constraint with a margin that is provided in the DSAA stage. As presented in the previous chapter, energy transferred between two microgrids can be satisfied via different actions (LT, DGT, and LT/DGT). In (4.9), the amount of energy transferred between μA_y and μA_x has to be equal the total generation transferred between the microgrids. The constraints in (4.10) and (4.11) are given for the active and reactive power transfer mismatch between the tied microgrids, i.e. the imported and exported power variables must be equal.

4.4 Proposed Algorithm Based on OPTAPO

A distributed constraint optimization algorithm is proposed, based on OPTAPO. This algorithm is based on solving parts of the optimization problem; it then merges partial solutions into a global one [127, 128]. OPTAPO uses mediation to construct connected sub–problems, which are solved by a selected agent (the mediator) merged with other sub–problem solutions. This will, in turn, achieve a global solution for the distributed constraint optimization problem. This process works, first, by constructing a good–list, taking into consideration the agent–view structure, which contains all local variables, and the constraints in the assigned zone of the mediator agent. Each mediator agent attempts to reach an optimal solution for its sub–problem, or minimize the penalty cost, based on the cost of its violated constraints. The mediator agent also starts a mediation session with other neighbor mediator agents in their good–list. This process is used to compute the optimal value of the sub–problems by changing assignments of the variables of each mediator agent zone. Whenever the mediation cannot be achieved without causing a cost greater than zero for agents outside of the mediation session, the mediator agent communicates with those agents to include them in the next session. In other words, the mediator agent attempts to optimally solve the sub–problem in the next session, with the support of these additional agents. When the constraint cost is greater than zero, neighboring zones try to merge into a single, bigger zone, in order to minimize overall costs of the violated constraints. OPTAPO is terminated when there is no violation for any constraints, and also when all sub–problems reach their optimal solution, i.e. a global optimal solution.

In decentralized control schemes, intelligent agents should be able to communicate with each other using language that shares common syntax, semantics, pragmatics, and mutual understanding. In this work, the foundation for intelligent physical agent (FIPA) is utilized [121, 129]. The FIPA messages can provide a well–defined process, where messages can contain various parameters, based on the situation; some of these parameters are defined as: performative, sender, receiver, and content. According to [130], the FIPA request interaction protocol was selected, where the sender agent requests an action from the receiving agents, indicating the out–of–service zone. The receiving agents either fulfill the request message, or reply that the task cannot be completed, or refuse an action. In the case of an agree message, the receiver agent tries to execute the action to be sent to the sender agent. As a result, a message of response is created to inform on the status of the execution.

4.4.1 Solution for the DSAA Problem using OPTAPO

The described DSAA problem is solved in this work using OPTAPO, where each microgrid agent is defined as a mediator agent. The mathematical formula for the OPTAPO can be expressed in the DSAA problem as a function that is mainly dependent on three parameters, as follows:

$$OPTAPO = f(MG, S, C) \tag{4.12}$$

where, MG is the set of defined microgrids in SDGs $[MG_1, MG_2, \ldots, MG_n]$, S is the set of the supply adequacy for each microgrid that can be transferred $[S_1, S_2, \ldots, S_n]$, and C is the set of applied power transfer constraints $[C_1, C_2, \ldots, C_n]$, for each mediator agent responsible for microgrid and included in the OPTAPO process. To that end, a Request message is sent from the supported μA_x to the supporting μA_y containing an equal sharing of the not served loads A_{F_x}, given as:

$$Request = [A_{f_x}] \tag{4.13}$$

Once the *Request* message is received, each μA_y responds with either an *Agree* or *Refuse* message. An *Agree* message contains A_{P_y} that can be transferred, and the number of layers (l) between the supported and supporting agents (i.e. l=1 for the μA_y adjacent to μA_x, since they are directly connected to the μA_x) as follows:

$$Agree = [A_{P_y}, l] \qquad \forall y \in Y \tag{4.14}$$

Upon receiving a *Refuse* message, the μA_y sends a message with a zero contribution from its μA. Once reply messages are received, the μA_x starts building its own good–list, and thus, its agent–view.

While μA_x is processing the received messages, supporting agents continue searching for power availability from higher layer agents. The search continues until either: 1) μA_x sends an *Inform-Done* message to its supporting agents, due to having received enough power to supply the un–served load $S_{F_x}^{Max}$ or; 2) supporting agent μA_y sends an *Inform-Done* message to μA_x when no additional back–

feeding power can be supplied. Finally, μA_x combines all received *Agree* messages to form its own good–list. The good–list is used to store all proposed solutions from μA_y(s) to the μA_x, in which μA_x constructs the agent–view from the good–list by rearranging the proposed solutions, based on the number of layers, l.

At this stage, the μA_x can solve (4.4) and (4.4) and then generate/send the value assignment A_{P_r} for/to the supporting agents.

4.4.2 Solution for the Formulated DOR Problem using OPTAPO

In DOR, each agent aims to determine the switching actions that satisfy the internal constraints, as well as the assigned back-feeding power transfer from the first stage. To that end, adjacent agents exchange the state variables of the dummy bus, and their candidate power transfers action (i.e., LT, DGT, and LT/DGT), expressed as follows:

$$Propose = [ID, S_{d_y}, V_{d_y}, \theta_{d_y}] \tag{4.15}$$

The supporting agents μA_y initiates the iteration process; where it sends its value assignments in (4.15) to its adjacent supported agents μA_x, in the form of a *Propose* message. It is worth noting that the value assignments are chosen to minimize the internal switching actions of the agent. Each μA_y searches for internal value assignments that minimize the violated constraints in order to achieve the $A^y_{P_r}$. To that end, each μA_y searches for optimal DG settings and switching operations.

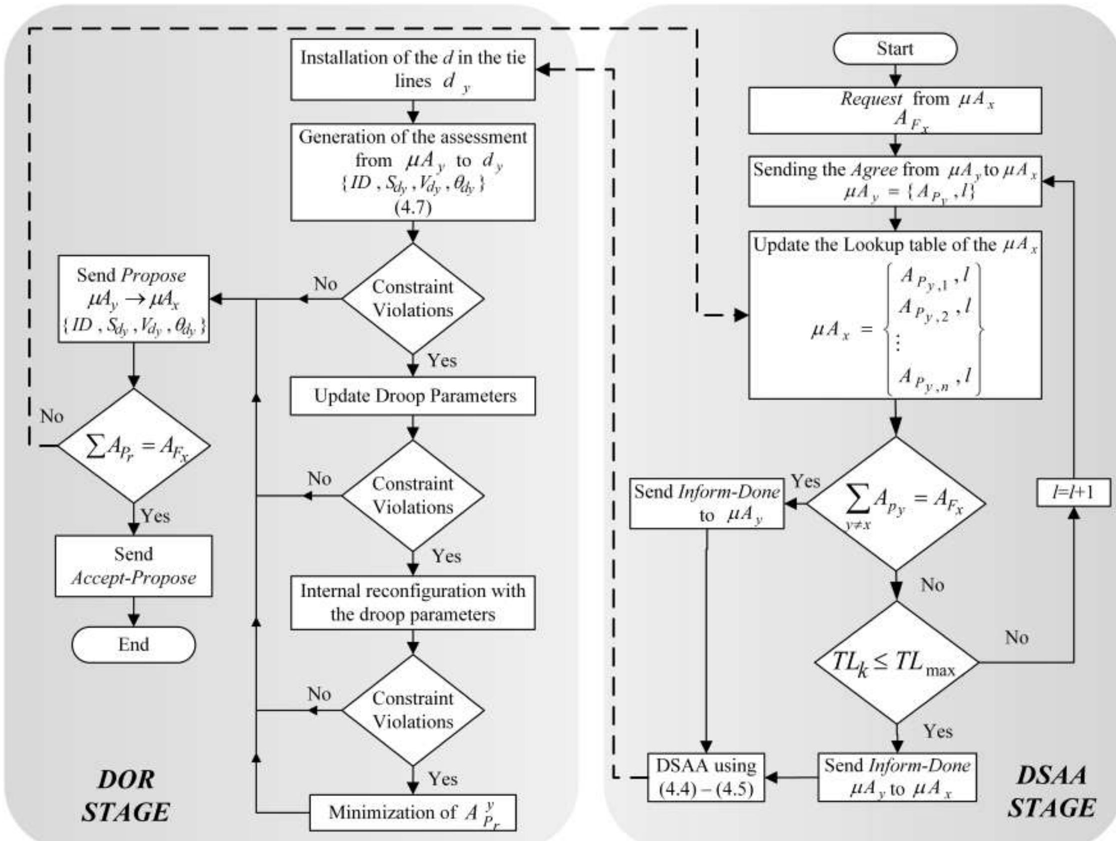

Figure 4.3: Flowchart of the proposed OPTAPO

In some cases, the value assignments of switching actions of adjacent agents may result in creating a new IMG. If the proposed solution is accepted, μA_x sends an *Accept-Proposal* message. However, if none of the switching actions satisfy the system constraints, and the assigned power transfer, the μA_x updates the power transfer value assignments for each agent in the first stage, sending a new *Inform-Done* message. This iterative process continues until an optimal solution is found, and an *Accept-Proposal* message is sent to all μA_y from their μA_x.

Figure 4.3 provides a flowchart that summarizes the proposed two stages of the distributed restoration algorithm. This flowchart is valid for any supported agent μA_x and its adjacent supporting agent(s) μA_y. Supporting agents that are non–adjacent to the supported agent (i.e. upper layers) are communicating with their adjacent supporting agents, in the lower layers, in a similar manner.

4.4.3 Communication Requirements of the OPTAPO

Based on the proposed algorithm, the OPTAPO is decomposed in two stages (DSAA and DOR), in which each stage has its own message and data to be transferred between agents. Such decomposition aims to improve the search for the control agents in the solution space, and thus reduce the number of execution cycles required to reach a solution. In the DSAA, exchanged messages between participant agents contain two types of value assignments, which are the maximum capacity of supporting energy and the number of layers, respectively. The DSAA stage is then terminated by sending an *Inform-Done* message to terminate the search process. As for the DOR, exchange messages sent between the participant agents consist of four pieces of information, as presented in the OPATPO: the ID of the energy transfer type, the maximum capacity that can be transferred, limitations that cause minimum voltage to occur at the dummy bus representing the supporting feeder, and its angle, respectively. In total, the OPTAPO consists of six pieces of information to be exchanged between agents. These messages are followed by an *Accept-Proposal* response to terminate the search process.

According to [77, 131, 132], any integer data is 32-bit data and any float number is 64-bit data. The energy transfer ID and the response of each stage (i.e. *Inform-Done* or *Accept-Proposal*) are 32-bit integer data, and the rest of the information exchanged is float numbers, where by the size of each is 64-bit data. Therefore, the total message size of the DSAA is 160 bits and the total message size of the DOR stage is 256 bits. In total, the message size in the OPTAPO can be estimated at 416 bits, which is significantly small, and, thus, the lowest Ethernet 64-byte packet size can be used for these messages. In addition, in order to calculate the bandwidth for the OPTAPO, the data transferred rate (DTR) can be calculated as [77], which tests the convergence of the proposed algorithm. The DTR of the OPTAPO should be as follows:

$$DTR = \frac{n_c.n_m.p_z}{T} \tag{4.16}$$

where, n_c is the number of cycles until convergence, where one cycle of computation represents that at least one agent, start receiving messages, processing the calculation and then send back the action. n_m is the number of back and forth messages per cycle which is based on the number of agents in the system, p_z is the packet size used to transfer the data and finally T is the execution time of the total process. The data rate can be calculated assuming a worst-case scenario, where each agent connects to all other agents and thus sends 2 x ($n_{MG} - 1$) messages, where n_{MG} is the number of microgrid agents. Given that, the number of cycles is found to be linearly correlated to the number of agents, a SDG with 10 microgrid agents can reach the convergence within 25 cycles, which will be carried in few seconds [77]. Therefore the estimated required bandwidth can be estimated as 60 kHz which is double the DTR. From the above discussions, it can be observed that a low bandwidth can be used for the proposed algorithm.

4.5 Case Studies and Simulation Results

In order to test the effectiveness of the proposed multi–agent self–healing restoration algorithm, simulation studies have been carried out in the parallel computing MATLAB toolbox environment. The 70-bus distribution system has been used in the case studies as shown in Fig 3.31 with the same assumptions. In this study, a normalization of the two functions (i.e. load restoration and the switching operation, respectively) is performed to be represented as a total cost of restoration. First of all, in order to represent the restored load, different loads and their behavior have to be taken into account. The behavior of residential, commercial and industrial loads defers during a daily time domain which is directly proportional for the restoration solution. Besides, the interruption cost of each load changes based on the load type [58, 122, 124]. Therefore, CIC depends on the expected behavior of the loads in addition to the duration of interruption during the restoration process. Secondly, the life time of the switches in the system have to be considered in order to represent the optimal restoration cost and sustain the system reliability [133]. Three case studies were carried out to validate the effectiveness and robustness of the proposed distributed restoration algorithm. The first case study involved testing the effectiveness of the proposed distributed algorithm, compared to centralized optimization. In the second case study, the convergence and the robustness of the proposed algorithm were tested for extreme events (i.e.multiple faults). Finally, a third case study was implemented to test the impact of communication failure between μA(s).

4.5.1 Comparison between Centralized and Distributed Restoration Processes in SDGs

During a full loading condition, a fault is assumed to occur at the main substation microgrid circuit breaker (FCB4) in T2 in which loads from L49 to L69 are out-of-service, and DG8 is the only local microgrid source for these loads. Repair time for the fault is assumed to be 2 hours. Table 4.8 shows the results of the centralized restoration using a centralized optimization algorithm, taking into consideration the multi–layer restoration process, with the creation of a new, non–predefined IMG. Table 4.9 shows the optimized droop parameters of the IMG(s) after restoration.

Total cost is based on the change of sw status, in addition to the un-served loads after restoration.

Table 4.8: Restoration process in a Multi–microgrid system

Control Scheme		Centralized Control	Proposed OPTAPO
Switching Operation		Close: S36, S40, S43, S46 Open: S3, S8, S17, S22, S33	
Elapsed Time		3.7319 Sec	1.862 Sec
Un-served loads		L69 (Industrial)	
CIC		$ 1,621	
Total Cost		$ 2,078	
New Created IMG		L7 - L9, L14 - L17, L52 - L57, L66 - L68	
Communication Requirements	DTR	—	1.728 kbps
	Bandwidth	—	3.45 kHz

Table 4.9: Optimized DG Droop parameters for restoration

		m_P	n_q	ω^*	V^*
Scheduled IMG	DG3	0.0027	0.05	1	1.02
	DG4, DG5	0.0054	0.1	1	1.03
New Created IMG	DG1, DG2	0.0054	0.1	1	1.03
	DG8	0.0108	0.2	1	1.02

Based on the proposed distributed optimization, a μA is defined for each predefined microgrid. The μA(s) installed in the system start(s) to communicate with adjacent μA(s), in order to allocate resources for the restoration of the out-of-service zone. In Fig 4.4, the exchange messages between the μA(s) are clarified.

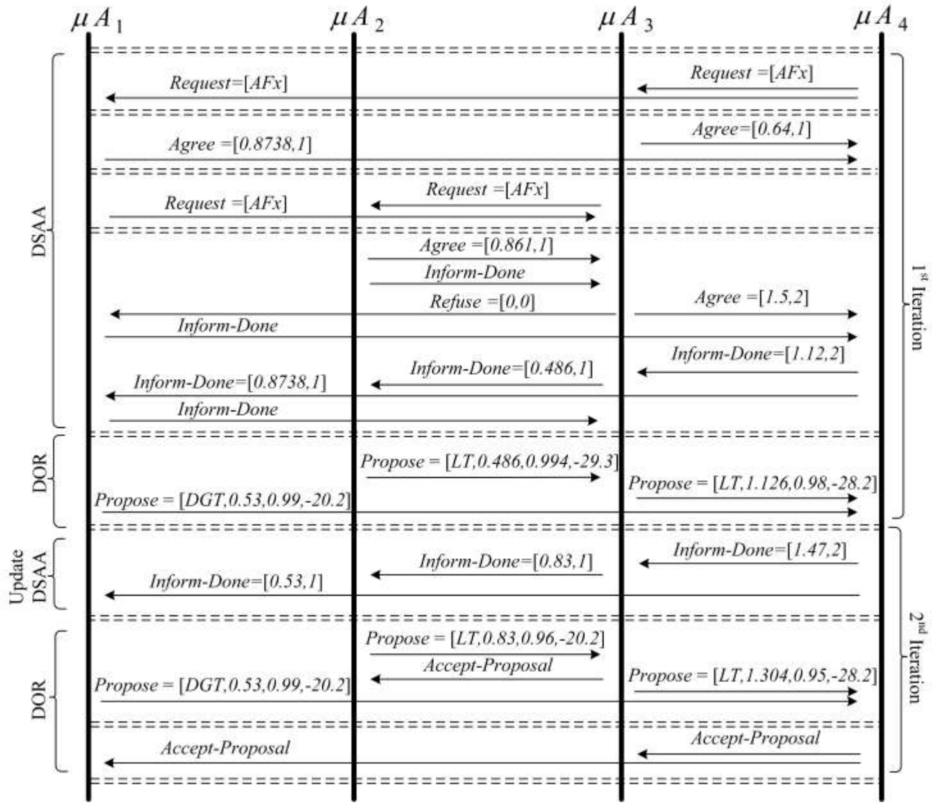

Figure 4.4: Exchanged messages between the MAs for the first case study

After the fault clearance, the supported μA_4 initiates a *Request* to the supporting adjacent agents, μA_1, and μA_3, as in (4.13). When the *Request* is received, the supporting μA(s) respond(s) by sending an *Agree* message containing information about the contents of the available power, where μA_3 = (0.64, 1), and μA_1 = (0.8738, 1). While μA_4 processes the information received, μA_1 and μA_3 continue searching for support from their adjacent agents. Based on the configuration of the test system, a *Request* is sent from μA_3 to μA_2 and μA_1. A *Request* is also sent from

μA_1 to μA_3. At this time, μA_3 notices two different *Request*(s) from μA_4 and μA_1, where the priority to respond is taken into account at μA_3. The search process is terminated when an *Inform-Done* is sent from either the supporting or supported agent(s). It is noted that μA_2 does not have upstream adjacent microgrid(s), hence it sends *Agree* with the contents (0.86, 1) to μA_3. Consequently, μA_3 updates the contents of its *Agree* to (1.5, 2), followed by *Inform-Done* to μA_4. In the simulation, it has been noted that μA_3 sends *Refuse* to the μA_1 *Request*, since the maximum available capacity is sent directly to the higher priority Request (μA_4). It is worth noting that after satisfying μA_4, the remaining capacity at μA_3 will be sent to μA_1, unless an *Inform-Done* is sent from μA_1. Therefore, the updated *Agree* from μA_1 remains the same, since its alternative did not respond with availability support. As such, an *Inform-Done* is sent from μA_1 to μA_4, as well. Based on the received *Agree*, μA_4 built its good–list to allocate resources for the restoration process, with a priority given to the options with enough resources and a fewer number of layers. As such, the constructed good–list is found to be [0.8738,1 ; 0.64,1 ; 1.5,2] and the DSAA problem is solved, then, at μA_4. The assessment of theμA_y(s) can be seen in Fig 4.4.

Once the first stage is complete, the algorithm moves toward the second stage to determine the optimal configuration and energy transfer actions that satisfy the specified constraints of the first stage. Since μA_2 is the least supporting microgrid based on l (i.e. 2nd layer), it generates the required amount of assigned MVA $A^2_{P_r}$. μA_2 *Propose* its optimal action through LT for the faulted area. As a result of LT, μA_3 has no constraints on the proposed solution, therefore μA_3 sends an *Accept*-Proposal to μA_2, and executes only one switching operation in order to transfer the loads from T3 to T4, and prevent any violation at μA_2. After the 2^{nd} layer of restoration is executed, the DOR solution moves to the 1^{st} layer between the adjacent μA_y to μA_4, where μA_1 and μA_3 determine their actions, based on the MVA amount (i.e., $A^2_{P_r}$: 0.4862) received from the 2^{nd} layer. In μA_1, the $A^1_{P_r}$ cannot be satisfied using the LT action, due to an internal voltage violation in the microgrid. For this reason, μA_1 Proposes DGT as an action and thus transfers DG1 and DG2 installed at downstream buses, with a maximum $A^1_{P_r}$ of 0.5298 MVA. As for μA_3, it takes the advantage of LT from μA_2 and *Proposes* the required $A^3_{P_r}$. The total amount of MVA received by μA_4 is 1.656 MVA (i.e. 1.1262 MVA from μA_3 and 0.5298 MVA from μA_1). Therefore, μA_4 repeats the DSAA stage again taking into consideration the maximum limit from μA_1 (i.e. 2^{nd} iteration). As shown in Fig 4.4, the value assignment determined by μA_4 for each μA for the 2^{nd} updated DSAA iteration. As a result of the new assessment, the μA(s) continue(s) the negotiation process, as in Fig 4.4, in which μA_4 receives the proposed actions of μA_1 and μA_3 and those actions meet the new assessment, as follows: μA_1 to μA_4 = [DGT, 0.53, 0.99, -20.2], μA_3 to μA_4 = [LT, 1.304, 0.95, -28.2]. μA_4 notices the maximum optimal solution that can be received since the required assessment is executed, therefore an *Accept*-Proposal for both μA_1 and μA_3. Based on the proposed settings, μA_4 determines its optimal internal configuration. Table 4.8 summarizes the results of the proposed distributed optimization algorithm in which execution time to convergence is much less than for the centralized control, since it only took two iterations to reach the same solution as the centralized control. Figure 4.5 shows voltage profile for the created configurations, after the restoration. It is worth noting that the minimum occurred voltage in the total system is 0.966 p.u.

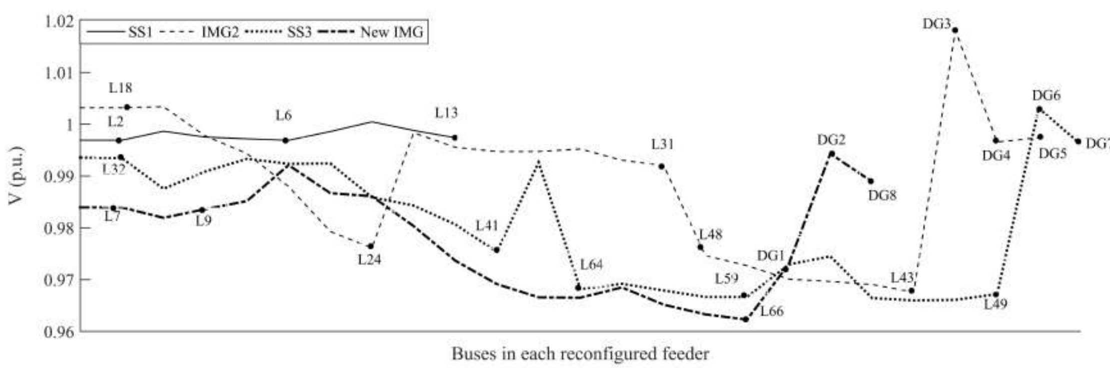

Figure 4.5: Voltage profiles for the post-restoration microgrids in the first case study

4.5.2 Performance of OPTAPO when Multiple Faults Occur

The second case study assumed a different multi–fault occurrence in the system, where one of the faults is assumed to take place at T3, in switch S27, at peak loading condition. The other fault is assumed to be a total damage of DG7. In order to test the strength of the OPTAPO restoration search, an overloading is assumed in one of the supporting feeders (i.e. T2) during a fault occurrence. Figure 4.6 depicts the exchange messages of the OPTAPO during the restoration process in the second case study.

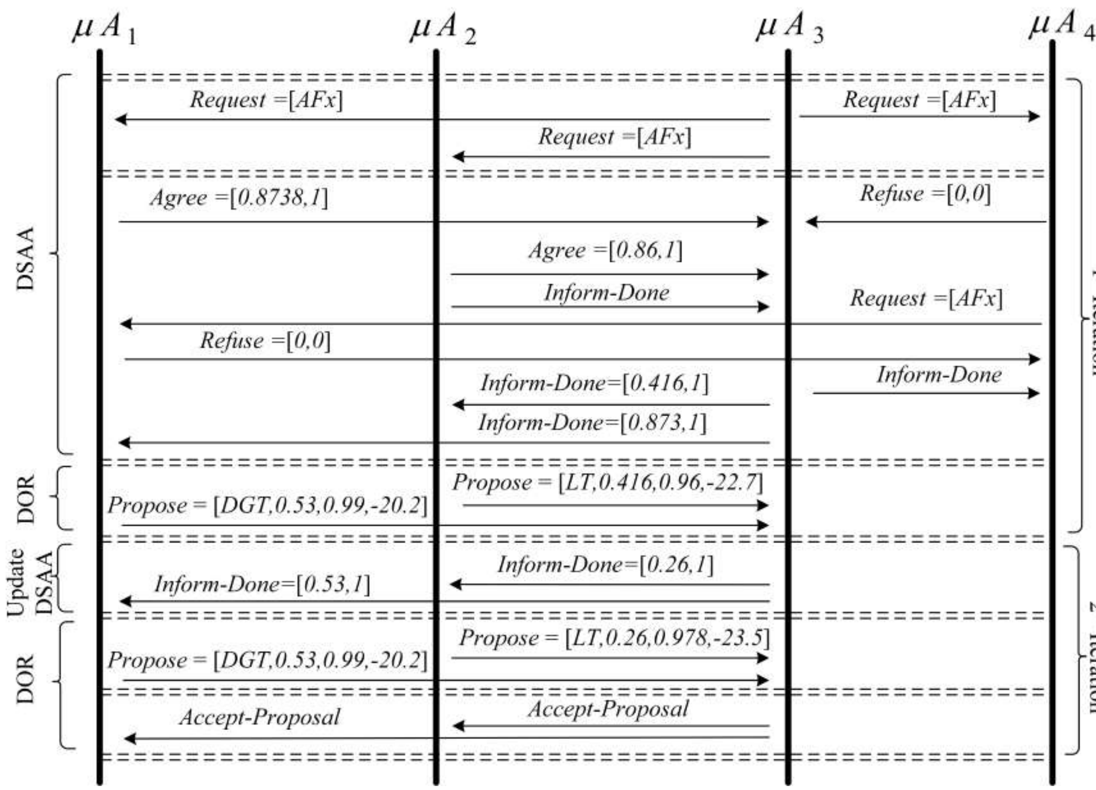

Figure 4.6: OPTAPO exchanged messages between MAs for the second case study

As shown in the figure, after fault clearance, the out-of-service power in T3 is 1.79 MVA, and the supported agent μA_3 sends a *Request* to its adjacent μA(s), based on the DSAA of the proposed OPTAPO. The supporting μA_1 and μA_2 send their available power through an *Agree* message to μA_3. Due to the overloading of T2, μA_4 starts to search for further support to perform a multi-layer restoration process; in this case, the only adjacent supporting feeder for μA_4, is μA_1. Therefore, μA_1 starts to build a priority using the *Request* received from μA_3 and μA_4. According to the receiving time, μA_1 needs to support μA_3 first, therefore μA_1 sends a *Refuse* to μA_4. As a result, μA_4 sends a *Refuse* to μA_3. μA_1 sends an *Agree* to μA_3, with a maximum MVA of [0.8738, 1]. Similarly, μA_2 sends an *Agree* with [0.8595, 1]. Based on the total received supporting power A_{P_y}, μA_3 can build its good–list and perform the DSAA stage, which ultimately sends an *Inform-Done* to μA_y(s). This assessment takes into consideration that DG6 is still in service and it can assist in the creation of IMG. According to the good–list of the μA_3, μA_1 and μA_2 have the same l, while the proposed MVA of μA_1 is greater than that of μA_2. Therefore, μA_3's assessment starts from μA_1, followed by μA_2. It is worth noting that another *Inform-Done* message is also sent to μA_4. In order not to search for additional solutions, this step is followed by an *Inform-Done* from μA_4 to μA_1. According to the proposed OPTAPO, all the μA(s) starts the DOR stage to set the optimal configurations, starting from the last layer, if applicable. μA_2 will satisfy the required $A^2_{P_r}$ from μA_3 without sacrificing its own DGs, therefore the sent Propose is in the form of an LT. On the other hand μA_1 can not achieve the required $A^3_{P_r}$ due to a violated constraint, therefore μA_1 sends the maximum contribution from its side by Propose to a DGT with the maximum available MVA. In this way, μA_3 takes advantage of the DGT to perform a new IMG. The received Propose message can not restore all of the un-served loads at T3, therefore μA_3 performs a 2^{nd} iteration of DSAA to update its good–list, taking into account the maximum limitation of μA_1. In the 2^{nd} iteration of the DSAA, μA_3 notices the benefit of the DGT from μA_1, therefore the assessment starts with μA_1 with the MVA of the DGT, and the rest comes from μA_2. μA_1 sends the maximum available power, based on the 1^{st} iteration. As for μA_2, $A^2_{P_r}$ in the 2^{nd} iteration is achieved, since this iteration is much less than the assessment of the 1^{st} iteration, therefore *Accept-Proposal* is sent from μA_3. The remaining MVA in T3 is restored with the aid of DG6; the appropriate switching is done by μA_3, taking advantage of the DGT from μA_1, and LT from μA_2. It is noteworthy that the total un-served loads are restored after these actions, and total restoration cost is based on the change of the switching operations to perform LT to μA_2, and create two new IMGs. Table 4.10 shows the total restoration process by the proposed OPTAPO, in addition to Table 4.11 for the optimized droop settings of the OPTAPO solution. Figure 4.7 depicts the voltage profile over the created networks after the restoration process.

Table 4.10: OPTAPO restoration actions for the second case study

DSAA	$A^{y}_{P_r}$ (1^{st}*iteration*)	μA_1: 0.8737 MVA μA_2: 0.4163 MVA
	Updated $A^{y}_{P_r}$ (2^{nd}*iteration*)	μA_1: 0.458 MVA μA_2: 0.734 MVA
Restoration Process	Switching Operation	Close: S36, S39, S41 Open: S3, S8, S31, S34
	Switching Operation Cost	\$ 304.5
	IMG_1	L7 - L9, L14 - L17, L46 - L48
	IMG_2	L33 - L35, L38 - L41
Communication Requirements	DTR	1.28 kbps
	Bandwidth	2.56 kHz

Table 4.11: Optimized DG droop parameters for the second case study

		m_P	n_q	ω^*	V^*
Scheduled IMG	DG3	0.0027	0.05	1	1.02
	DG4, DG5	0.0054	0.1	1	1.03
New Created IMG_1	DG1	0.0068	0.15	1	1.04
	DG2	0.0039	0.05	1	1.02

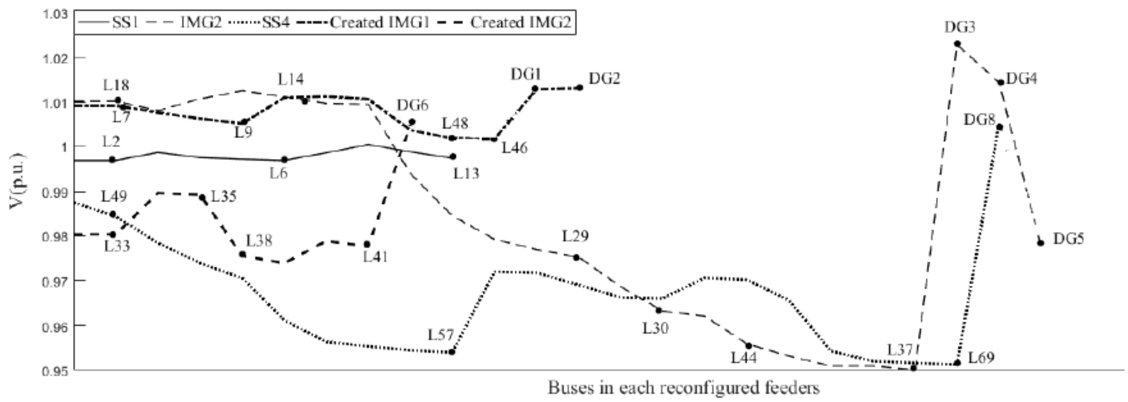

Figure 4.7: Voltage profiles for the post-restoration microgrids in the second case study

4.5.3 Impacts of Communication Failure on The proposed OPTAPO

A third case study was implemented to show the strength of the proposed OPTAPO. In this case study, the fault is assumed to take place at T3 in S27. A communication failure is also assumed to be occurred between T3 and T2. The total out–of–service power is found to be 1.79 MVA. After fault clearance, the supported agent μA_3 sends the *Request* to its adjacent μA(s). The supporting μA(s) (i.e., μA_1 and μA_2) send their available power to μA_3 (multi–path restoration process). Due to the miscommunication that occurred in T2, μA_4 will be eliminated from the restoration process. μA_1 Proposes an *Inform-Done* message to μA_3 with a max. MVA of [0.8738, 1], and, as for μA_2 the *Inform-Done* message is [0.8595, 1]. Based on the received, the $A^{y}_{P_r}$ and *Inform-Done* messages are sent from μA_3 to the supporting feeders, where μA_1 will be notified not to search for further support. μA_3 can build its own good–list, taking into consideration that DG6 and DG7 are in service to support the feeder and they can assist in the creation of IMG. According to the good–list of the μA_3, μA_1 and μA_2 have the same l while $A^1_{P_r} > A^2_{P_r}$ therefore μA_3's assessment will start from μA_1 and then in order μA_2 if required. The assessment for μA_1 can be shown in Fig 4.8. After the installation of the dummy bus between μA_1 and μA_3, the optimal support, based on the $A^1_{P_r}$ is LT with a maximum value of 0.458 MVA. Finally, μA_3 will notice that the available power received will be sufficient with the creation of IMG by using DG6 and DG7. Therefore, μA_3 will perform an inner reconfiguration in T3 to take advantage of the LT from μA_1 and also create a new IMG. The total switching operation is shown in Table 4.12, and Table 4.13, the optimized droop parameters of the DGs are presented. Figure 4.9 presents a voltage profile for all feeders.

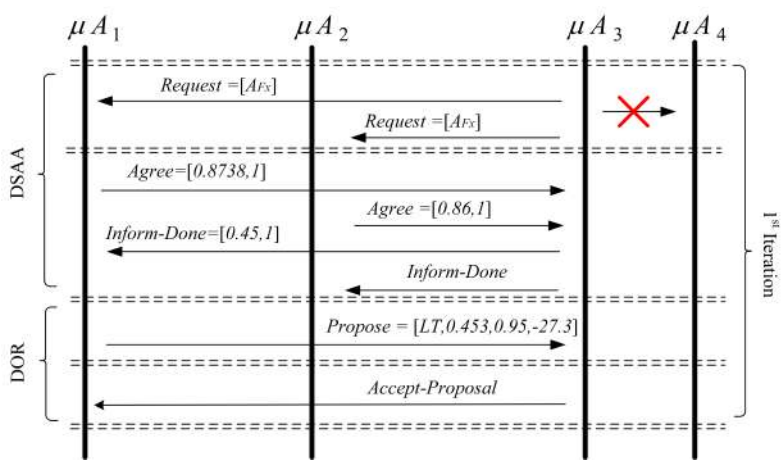

Figure 4.8: OPTAPO exchanged messages between MAs for the third case study

Table 4.12: OPTAPO Restoration actions for the third case study

DSAA	$A^{y}_{P_r}(1^{st} iteration)$	μA_1 : 0.45 MVA
Restoration process	Switching operation	Close S41, Open S34
	Unserved loads	——
	Total Cost	$ 101.5
Communication requirements	DTR	0.512 kbps
	Bandwidth	1.024 kHz

Table 4.13: Optimized DG Droop parameters for the third case study

		m_P	n_q	ω^*	V^*
Scheduled IMG	DG3	0.0027	0.05	1	1.02
	DG4, DG5	0.0054	0.1	1	1.03
New IMG	DG6	0.0062	0.12	1	1.04
	DG7	0.0054	0.05	1	1.03

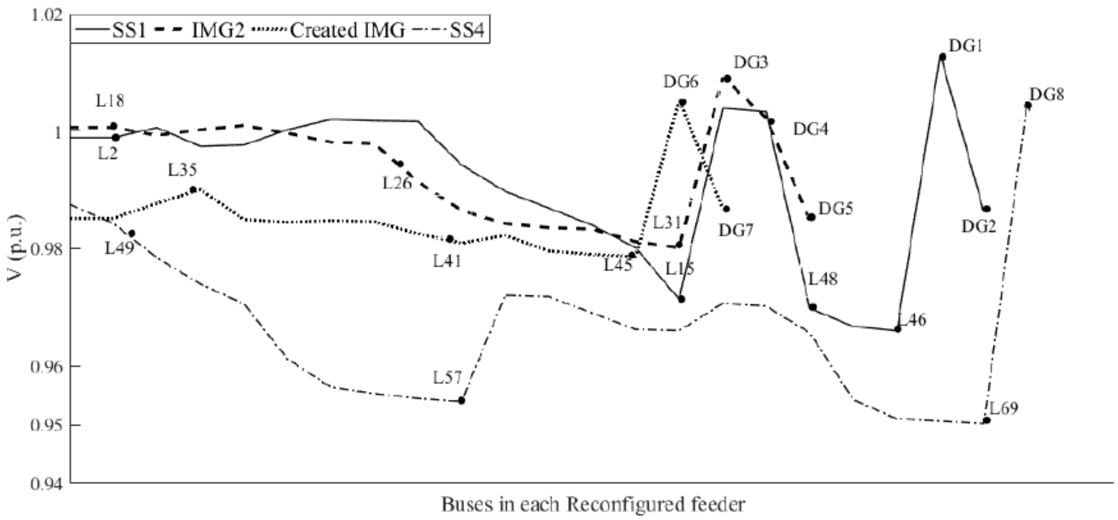

Figure 4.9: Voltage profiles for the post-restoration microgrids in the third case restoration

4.6 Summary of the Proposed Multi–agent Restoration Algorithm

The problem of service restoration in SDGs clustered into microgrids is formulated as a multi–agent problem. The formulated problem takes into account the special features and operational characteristics of droop–controlled IMGs. The OPTAPO technique is utilized to solve the formulated problem, where each agent is responsible for its microgrid and to create a mediation session between adjacent agents in order to reach an optimum solution. The proposed algorithm can be easily implemented in a real network, where the loads and generations are constantly changing. The performance of the proposed OPTAPO is discussed, such that its performance is measured using a metric called "number of iterations". The number of iteration takes into account communication and execution time and cost. Also, further discussion of distributed constrain optimization methods shows the superiority of the proposed OPTAPO, in performance terms, for small and large–scale problems. In addition, the proposed OPTAPO is divided into two stages in order to reduce computational burden. The first stage aims to allocate resources for the out–of–service loads via a mediation process between the microgrid control agents. In the second stage, the optimal tie line energy transfer from the first stage is set, as a power transfer constraints, between the adjacent microgrids. Based on these two stages, five types of value assignments for the agents' variables are created, in order to improve the search for the μA(s) in the solution space, and thus, reduce the number of required iterations to reach a solution.

Chapter 5 - Optimal Scheduling of Bidirectional Energy Conversion Units in Energy and Ancillary Services Markets for System Restoration within Multi–Carrier Energy Systems

Multi–carrier energy systems (MCESs) can be formed by integration of various energy infrastructures, including power and natural gas systems. The proliferation of bi–directional energy conversion units in a MCES can set the stage for a more resilient and robust system. Consequently, this chapter shows how bi–directional energy conversion units and storage devices can be optimally scheduled within a MCES for provision of various regulation services to the grid operator. In particular, a new model for optimal scheduling of PtG and GfG systems in an integrated grid considering service restoration in neighboring microgrids is introduced. The model aims to facilitate integration of renewable energy resources, utilize gas and power price arbitrage, provide regulation services to the real–time market, and contribute to the system restoration. New indices are proposed that would quantify the contribution of the MCES–based microgrid operator to the real–time and ancillary services market. The operation of the proposed model is both technically and economically evaluated using historical operating data on a test system. In particular, the main features of the proposed MCES are summarized in bullets here under:

- The proposed MCES model enables PtG and GfG units to provide services to the integrated microgrid including energy shifting via price arbitrage utilization.

- The proposed model enables the integrated microgrid to participate in the restoration process internally or in a neighbouring microgrid.

- The model enables a back–feeding service from the integrated microgrid to the PtG gas storage in case of a gas grid outage.

- New indices are introduced that would quantify the contribution of the MCES–based microgrid to real–time and ancillary service markets.

5.1 The Proposed MCES Model

The proposed model for optimal scheduling within a MCES along with the mathematical formulation is given in this section. Figure 5.1 (a) illustrates the interconnection of multiple supporting microgrids with a supported microgrid (i.e. faulted microgrid) where one of the supporting microgrids is integrated with the gas distribution grid. As shown in Fig 5.1 (a), the gas distribution grid has its own private investor who decides the operational characteristics of the PtG and GfG units based on the data in both the electrical and gas markets. In Fig 5.1 (b), the mediation sessions between the integrated supporting microgrid and gas utility are presented. Based on the constructed tie lines, a service request signal can be issued by the supported microgrid (i.e. S_1), and a response is given from the supporting microgrids (i.e. S_2, S_3, S_4, ...). The integrated supporting microgrid could request more generation from the gas utility, if needed. All the messages between the integrated microgrid and the gas utility can be seen in Fig 5.1 (b). As shown in Fig 5.1 (b), PtG and GfG units are scheduled for arbitrage, service restoration, and contribution to the real–time market.

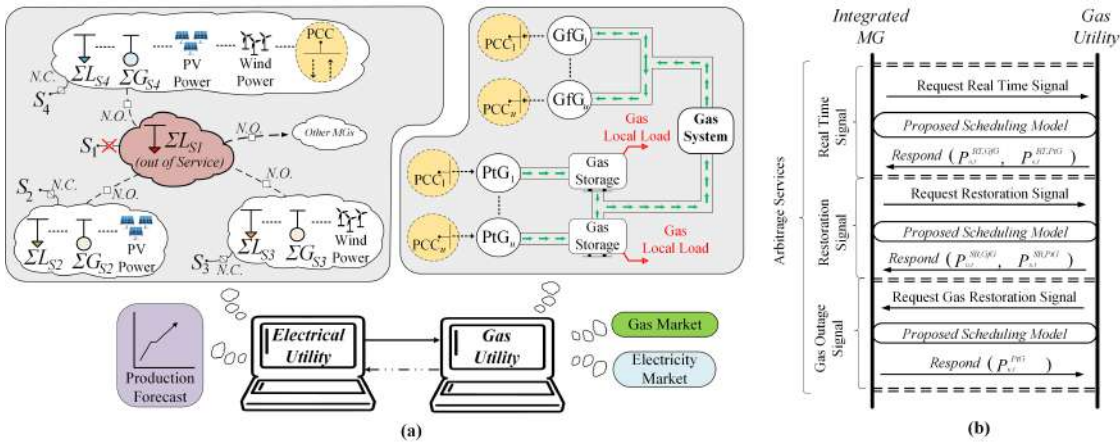

Figure 5.1: Interconnection between multiple grids. (a) Multiple distribution feeders in both the electrical and gas utilities; (b) Communication messages between utilities for different services.

.

It is worth noting that a real–time signal from the market can represent a power adequacy problem that can be resolved by an increase or decrease in the generation of PtG/GfG units. The figure shows that a gas storage unit is deployed at the point of common coupling (PCC) between the PtG unit and the integrated microgrid where it supplies a local gas load in case of an outage in the main gas distribution grid. Furthermore, the proposed algorithm takes into account the restoration process between two neighboring microgrids. As shown in Fig 5.1 (a), the red marked microgrid faces a fault on the main feeder S_1; thus, it is tripped off the grid. This action classifies microgrids into supported and supporting ones, where the faulted one is considered as the supported. The supported microgrid can request power from the neighboring supporting microgrids through sending a service restoration signal. In such a case, supporting microgrids can participate to restore the faulted loads in the supported microgrid. While S_2 and S_3 can support the faulted microgrid, S_4 has a higher prospect to provide longer–term support since it has access to the gas grid. Figure 5.1 (b) shows the information exchange mechanism between the microgrids for different services.

The formulation of the proposed model is given in the below sections where a new algorithm for optimal scheduling of integrated electrical–gas systems is presented in Section 5.1.1. The optimal algorithm enables the integrated system to (i) exploit arbitrage opportunities, (ii) assist in restoration of electrical and gas loads in case of grid outages, and (iii) balance the supply and demand in the grid through participation in the real–time market. In Section 5.1.2, new indices are presented to assess the efficacy of the proposed algorithm in providing restoration services and contributing in the real–time market.

5.1.1 Proposed Optimal Scheduling Algorithm

5.1.1.1 Objective Function of the Optimization Problem

The objective function of the optimization problem is stated in (5.1) as a profit maximization function:

$$\text{Maximize}:$$
$$\sum_{t\in\mathbb{T}}\left\{\begin{aligned}&\sum_{u\in\mathbb{U}}\big(P_{u,t}^{GfG}-P_{u,t}^{PtG}\big)\,.\,E_t^{Prc}\\&+\sum_{u\in\mathbb{U}}\big(F_{u,t}^{PtG}-F_{u,t}^{GfG}\big)\,.\,G_t^{Prc}\\&-\sum_{u\in\mathbb{U}}\big(C^{GfG}\,.\,P_{u,t}^{GfG}+C^{PtG}\,.\,F_{u,t}^{PtG}\big)\\&-\sum_{u\in\mathbb{U}}\beta_{u,t}^{RT,GfG}.\,\big(P_{u,t}^{S,RT,GfG}+P_{u,t}^{S,RT,GfG'}\big)\\&-\sum_{u\in\mathbb{U}}\beta_{u,t}^{RT,PtG}.\,\big(P_{u,t}^{S,RT,PtG}+P_{u,t}^{S,RT,PtG'}\big)\\&-\sum_{u\in\mathbb{U}}\beta_{u,t}^{SR}.\,P_{u,t}^{S,SR}\\&-\sum_{u\in\mathbb{U}}\big(\beta_{u,t}^{Dhg}\,.\,F_{u,t}^{S,Dhg}+\beta_{u,t}^{Res}\,.\,LOG_{u,t}^{S,Res}\big)\end{aligned}\right\}.\,\Delta T, \tag{5.1}$$

where 5.1 includes the following terms:

- Electricity price arbitrage: $\sum_{u\in\mathbb{U}}\big(P_{u,t}^{GfG}-P_{u,t}^{PtG}\big)\,.\,E_t^{Prc}$. Where, $P_{u,t}^{GfG}$ is the output power of the GfG unit u and $P_{u,t}^{PtG}$ is the input power for the PtG unit u. E_t^{Prc} is the electricity prices (\$/MWh).

- Gas price arbitrage: $\sum_{u\in\mathbb{U}}\big(F_{u,t}^{PtG}-F_{u,t}^{GfG}\big)\,.\,G_t^{Prc}$. Where, $F_{u,t}^{GfG}$ is the gas inflow of GfG unit (m^3/h) and $F_{u,t}^{PtG}$is the gas outflow of PtG unit (m^3/h), G_t^{Prc} is the gas prices (\$/m^3).

- Cost of operation: $\sum_{u\in\mathbb{U}}\,\big(C^{GfG}\,.\,P_{u,t}^{GfG}+C^{PtG}\,.\,F_{u,t}^{PtG}\big)$. Where, C^{GfG} and C^{PtG} are the GfG and the PtG units operating expenditure (\$/m^3), respectively.

- Term managing GfG unit contribution to real–time market: $\sum_{u\in\mathbb{U}}\beta_{u,t}^{RT,GfG}.\,\big(P_{u,t}^{S,RT,GfG}+P_{u,t}^{S,RT,GfG'}\big)$. Where, $P_{u,t}^{S,RT,GfG}$ and $P_{u,t}^{S,RT,GfG'}$ are the GfG positive and negative slack variables for real–time service (MW), respectively. $\beta_{u,t}^{RT,GfG}$ is the GfG real–time service penalty factor (\$/MWh).

- Term managing PtG unit contribution to real–time market: $\sum_{u\in\mathbb{U}}\beta_{u,t}^{RT,PtG}.\,\big(P_{u,t}^{S,RT,PtG}+P_{u,t}^{S,RT,PtG'}\big)$. Same as the GfG unit, $P_{u,t}^{S,RT,PtG}$ and $P_{u,t}^{S,RT,PtG'}$ are the PtG positive and negative slack variable for the real–time service (MW), respectively. and $\beta_{u,t}^{RT,PtG}$ is the PtG real–time service penalty factor (\$/MWh).

- Term managing the contribution of the supporting microgrid to service restoration: $\sum_{u\in\mathbb{U}}\beta_{u,t}^{SR}.\,P_{u,t}^{S,SR}$, $P_{u,t}^{SR}$ is the system restoration signal (MW) at unit u and $\beta_{u,t}^{SR}$ is the system restoration penalty factor (\$/MWh).

- Term managing the gas supply to the local gas consumer:

$\sum_{u \in \mathbb{U}}\big(\beta_{u,t}^{Dhg} \,.\, F_{u,t}^{S,Dhg} + \beta_{u,t}^{Res} \,.\, LOG_{u,t}^{S,Res}\big)$. $F_{u,t}^{S,Dhg}$ is the gas storage discharge rate (m^3/h) and $LOG_{u,t}^{S,Res}$ is the reserved gas storage slack variable (m^3). $\beta_{u,t}^{Dhg}$ and $\beta_{u,t}^{Res}$ are the gas storage discharge penalty factor and the reserve margin penalty factor (\$/m^3), respectively.

The objective function in (5.1) is subject to the following operational constraints of the PtG and GfG units:

$$P_{min}^{GfG} \leq P_{u,t}^{GfG} \leq P_{max}^{GfG} \quad \forall t \in \mathbb{T} \wedge \forall u \in \mathbb{U} \tag{5.2}$$

$$F_{min}^{PtG} \leq F_{u,t}^{PtG} \leq F_{max}^{PtG} \quad \forall t \in \mathbb{T} \wedge \forall u \in \mathbb{U}, \tag{5.3}$$

where (5.2) and (5.3) express the maximum and minimum output power constraint of the GfG unit and the output gas constraint of the PtG unit, respectively.

5.1.1.2 Energy Conversion Equations

The electrical and gas systems are linked through the following energy conversion equations:

$$P_{u,t}^{GfG} = \lambda^{GfG} .\, \eta^{GfG} .\, F_{u,t}^{GfG} \quad \forall t \in \mathbb{T} \wedge \forall u \in \mathbb{U} \tag{5.4}$$

$$F_{u,t}^{PtG} = \lambda^{PtG} .\, \eta^{PtG} .\, P_{u,t}^{PtG} \quad \forall t \in \mathbb{T} \wedge \forall u \in \mathbb{U}, \tag{5.5}$$

where (5.4) states the GfG unit output power in terms of its inflow gas, λ^{GfG} is the GfG unit conversion factor (MWh/m^3) and η^{GfG} is the efficiency of the GfG unit

(%). While (5.5) states the output gas of the PtG unit in terms of its input power, wehre; λ^{PtG} is the PtG unit conversion factor (m^3/MWh) and $\eta^{PtG}$is the efficiency of the PtG unit (%).

5.1.1.3 Power Flow Constraints

The microgrid distribution network is subject to the operational constraints as in the previous chapters such as (2.27) and (2.28), voltage operational limitation in (2.30). In addition to the branch power flow constraint as follow:

$$P^{Brn}_{i,min} \leq P^{Brn}_{i,t} \leq P^{Brn}_{i,max} \;\; \forall t \in \mathbb{T} \wedge \forall i \in \mathbb{F} \tag{5.6}$$

where the power flow limit of each branch $P^{Brn}_{i,t}$ is expressed in (5.6) limited to its maximum and minimum acceptable limit of operation.

5.1.1.4 Gas Flow Constraints

On the gas side of the integrated system, (5.1) is subject to the flow and pressure constraints stated by the following:

$$F^{Pip}_{k,min} \leq F^{Pip}_{k,t} \leq F^{Pip}_{k,max} \qquad \forall t \in \mathbb{T} \wedge \forall k \in \mathbb{P} \tag{5.7}$$

$$Pr^{Nod}_{l,min} \leq Pr^{Nod}_{l,t} \leq Pr^{Nod}_{l,max} \quad \forall t \in \mathbb{T} \wedge \forall l \in \mathbb{N} \tag{5.8}$$

$$\Delta Pr^{Nod^2}_{ll',t} = Pr^{Nod^2}_{l,t} - Pr^{Nod^2}_{l',t} - \mathbb{Z}_{ll'} \, . \, F^2_{ll',t}$$

$$\forall t \in \mathbb{T} \wedge \forall \, l \; \& \; l' \in \mathbb{N} \tag{5.9}$$

$$\Delta F_{l,t} = F^{Src}_{l,t} - F^{Dmd}_{l,t} - \sum_{l' \in \mathbb{N}} F_{ll',t}$$
$$\forall t \in \mathbb{T} \wedge \forall\, l \in \mathbb{N}. \tag{5.10}$$

where; $F^{Pip}_{k,t}$ is the gas flow in pipeline k (m^3/h) limited to its acceptable maximum and minimum operational limits. $Pr^{Nod}_{l,t}$ is the gas pressure at node l (kPa), $\mathbb{Z}_{ll'}$ is the pipeline resistance from node l to node l' (kPa.h/m^3) which is multiplied by the gas flow between the nodes $F_{ll',t}$ (m^3/h). Same as the electrical power flow, eq. 5.10 calculate the gas flow balance with $F^{Src}_{l,t}$ the gas injected at node l (m^3/h) and the $F^{Dmd}_{l,t}$ gas demand at node l (m^3/h).

5.1.1.5 Gas Storage Constraints

Changes to the level of gas (LOG) in the installed gas storage is limited by the PtG and storage operational limits as in (5.3) and (5.11), respectively; and represented by the input/output energy balance as in (5.12).

$$F^{Dhg}_{min} \leq F^{Dhg}_{u,t} \leq F^{Dhg}_{max} \quad \forall t \in \mathbb{T} \wedge \forall u \in \mathbb{U} \tag{5.11}$$

$$LOG^{G}_{u,t} - LOG^{G}_{u,(t-1)} + \big(F^{Dhg}_{u,t} - P^{PtG}_{u,t}\,.\,\lambda^{PtG}\,.\,\eta^{PtG}$$
$$+\,\lambda^{G,Dsp}.\,LOG^{G}_{u,t}\big)\,.\,\Delta T = 0 \quad \forall t \in \mathbb{T} \wedge \forall u \in \mathbb{U}. \tag{5.12}$$

In addition, a reserved capacity is kept in the gas storage to be used for local gas load restoration in case of gas grid outages as in (5.13) and (5.14):

$$LOG^{G}_{min} + LOG^{G,Res} - LOG^{S,Res}_{u,t} \leq LOG^{G}_{u,t} \leq LOG^{G}_{max}$$

$$\forall t \in \mathcal{T} \wedge S_{u,t}^{Grd,St} = 1 \quad (5.13)$$

$$0 \leq LOG_{u,t}^{S,Res} \leq LOG^{G,Res} \quad \forall t \in \mathcal{T} \wedge S_t^{Grd,St} = 1. \quad (5.14)$$

Where; $LOG_{u,t}^{G}$ is the LOG of gas storage (m^3), $LOG_t^{G,Res}$ is the gas reserved capacity for restoration service (m^3) and $LOG_{u,t}^{S,Res}$ is the reserved gas storage slack variable (m^3). $S^{Grd,St}$ is the gas system outage signal indicator. In case of a gas grid outage, the following constraints would apply to the supply of the local gas load; where the slack variable in (5.15) enables load curtailment in case of insufficient supply and (5.16) allows the use of reserved capacity.

$$F_t^{Dhg} = F_t^{GL} - F_{u,t}^{S,GLC}$$
$$\forall t \in \mathbb{T} \wedge \forall u \in \mathbb{U} \wedge S_t^{Grd,St} = 0 \quad (5.15)$$

$$LOG_{min}^{G} \leq LOG_{u,t}^{G} \leq LOG_{max}^{G}$$
$$\forall t \in \mathbb{T} \wedge \forall u \in \mathbb{U} \wedge S_t^{Grd,St} = 0, \quad (5.16)$$

where

$$0 \leq F_{u,t}^{S,GLC} \quad \forall t \in \mathbb{T} \wedge \forall u \in \mathbb{U} \quad (5.17)$$

Where; F_t^{GL} is the gas system outage signal (m^3/h) and $F_{u,t}^{S,GLC}$ is the gas system outage slack variable (m^3/h).

5.1.1.6 Constraints Set for Operation in the Real–Time Market

The real–time signals sent by the electrical microgrid are signals that indicate imbalance in the system. These signals can be fulfilled by the PtG unit demand response or GfG unit generation adjustment. Therefore, PtG demand could be increased in response to real–time signal from the electrical microgrid indicating excess power in the system, considering the slack variable $P_{u,t}^{S,RT,PtG'}$ to calculate the PtG unit participation in the market. Such a mechanism is formulated by (5.18):

$$\begin{gathered} P_{u,t}^{PtG} = P_{u,t}^{RT,PtG} - P_{u,t}^{S,RT,PtG} + P_{u,t}^{S,RT,PtG'} \\ \forall t \in \mathbb{T} \wedge \forall u \in \mathbb{U} \wedge M_t^{RT} = 1 \wedge \\ 0 \leq P_{u,t}^{S,RT,PtG} \leq P_{u,t}^{RT,PtG} - P_{min}^{PtG} \wedge \\ 0 \leq P_{u,t}^{S,RT,PtG'} \leq P_{min}^{PtG} - P_{u,t}^{RT,PtG}. \end{gathered} \tag{5.18}$$

Where; M_t^{RT} is the real–time ancillary service signal indicator. On the other hand, the generation of the GfG unit could be increased in response to the real–time signal requesting additional power in the system considering the slack variable $P_{u,t}^{S,RT,GfG'}$ to compute the contribution as stated in (5.19):

$$\begin{gathered} P_{u,t}^{GfG} = P_{u,t}^{RT,GfG} - P_{u,t}^{S,RT,GfG} + P_{u,t}^{S,RT,GfG'} \\ \forall t \in \mathbb{T} \wedge \forall u \in \mathbb{U} \wedge M_t^{RT} = 1 \wedge \\ 0 \leq P_{u,t}^{S,RT,GfG} \leq P_{u,t}^{RT,GfG} - P_{min}^{GfG} \wedge \end{gathered}$$

$$0 \leq P_{u,t}^{S,RT,GfG'} \leq P_{min}^{GfG} - P_{u,t}^{RT,GfG}. \tag{5.19}$$

5.1.1.7 Constraints Set for System Restoration

After the isolation of the faulty section in the supported microgrid, the service restoration signal is sent to all neighboring microgrids with the aim of allocating alternative sources for power restoration. The proposed algorithm takes into account the integration of the electrical and gas distribution grids. In addition, the response to the service restoration signal is resulted from summation of the contribution from the neighboring microgrids as stated in the following:

$$\begin{aligned} & P_t^{ES,SR} + \sum_{u \in \mathbb{U}} \big(P_{u,t}^{GfG,SR} - P_{u,t}^{PtG,SR} \big) = P_t^{SR} + P_{u,t}^{S,SR} \\ & 0 \leq P_{u,t}^{S,SR} \leq P_{u,t}^{SR}, \quad \forall t \in \mathbb{T} \wedge \forall u \in \mathbb{U} \wedge M_t^{SR} = 1, \end{aligned} \tag{5.20}$$

Where; $P_t^{ES,SR}$ is the supporting microgrid service restoration response (MW). $P_{u,t}^{GfG,SR}$ and $P_{u,t}^{PtG,SR}$are the GfG and PtG units power with restoration signal (MW), respectively. The slack variable $P_{u,t}^{S,SR}$ is considered to compute the contribution of the facilities to the restoration process. It is worth noting that supporting neighboring microgrids provide service restoration using their PtG and GfG units as dispatchable sources. M_t^{SR} is the system restoration signal indicator.

5.1.2 Contribution Indices

Four indices are proposed to assess the contribution of the microgrids to the real–time market and service restoration services. The real–time contribution index of PtG ($\mathrm{RTCI}^{\mathrm{PtG}}$) and the real–time contribution index of GfG ($\mathrm{RTCI}^{\mathrm{GfG}}$) are stated in (5.21) and (5.22), respectively:

$$\mathrm{RTCI}^{\mathrm{PtG}}\,\% = \Big(1 - \frac{\sum_{u\in\mathbb{U}}\sum_{t^h\in\mathbb{T}^{\mathbb{H}*}}(P^{S,RT,PtG}_{u,t^h} + P^{S,RT,PtG'}_{u,t^h})}{\sum_{u\in\mathbb{U}}\sum_{t^h\in\mathbb{T}^{\mathbb{H}*}} P^{RT,PtG}_{u,t^h}}\Big)\times 100, \tag{5.21}$$

$$\mathrm{RTCI}^{\mathrm{GfG}}\,\% = \Big(1 - \frac{\sum_{u\in\mathbb{U}}\sum_{t^h\in\mathbb{T}^{\mathbb{H}*}}(P^{S,RT,GfG}_{u,t^h} + P^{S,RT,GfG'}_{u,t^h})}{\sum_{u\in\mathbb{U}}\sum_{t^h\in\mathbb{T}^{\mathbb{H}*}} P^{RT,GfG}_{u,t^h}}\Big)\times 100. \tag{5.22}$$

In (5.21) and (5.22), $\mathbb{T}^{\mathbb{H}*}$ is stated as the set of historical time steps for PtG/GfG unit scheduling where,

$$\sum_{u\in\mathbb{U}}\sum_{t^h\in\mathbb{T}^{\mathbb{H}*}} P^{RT,PtG}_{u,t^h} \neq 0, \tag{5.23}$$

$$\sum_{u\in\mathbb{U}}\sum_{t^h\in\mathbb{T}^{\mathbb{H}*}} P^{RT,GfG}_{u,t^h} \neq 0. \tag{5.24}$$

The service restoration contribution index (SRCI) is formulated to assess the contribution of the GfG and PtG units to the service restoration process as stated in (5.25) and (5.26):

$$\mathrm{SRCI}^{\mathrm{GfG}}\,\% = \Big(\frac{\sum_{u\in\mathbb{U}}\sum_{t^h\in\mathbb{T}^{\mathbb{H}*}}(P^{GfG,SR}_{u,t} - P^{GfG,N}_{u,t})}{\sum_{u\in\mathbb{U}}\sum_{t^h\in\mathbb{T}^{\mathbb{H}*}} P^{SR}_{u,t^h}}\Big)\times 100, \tag{5.25}$$

$$\mathrm{SRCI}^{\mathrm{PtG}}\,\% = \Big(\frac{\sum_{u\in\mathbb{U}}\sum_{t^h\in\mathbb{T}^{\mathbb{H}*}}(P^{PtG,N}_{u,t} - P^{PtG,SR}_{u,t})}{\sum_{u\in\mathbb{U}}\sum_{t^h\in\mathbb{T}^{\mathbb{H}*}} P^{SR}_{u,t^h}}\Big)\times 100. \tag{5.26}$$

In (5.25) and (5.26), $\mathbb{T}^{\mathbb{H}*}$ is stated as the set of historical time steps for PtG/GfG unit scheduling where,

$$\sum_{u\in\mathbb{U}}\sum_{t^h\in\mathbb{T}^{\mathbb{H}*}} P^{SR}_{u,t^h} \neq 0. \tag{5.27}$$

It is worth noting that the terms $(P^{GfG,SR}_{u,t} - P^{GfG,N}_{u,t})$ in (5.25) and $(P^{PtG,N}_{u,t} - P^{PtG,SR}_{u,t})$ in (5.26) state the participation of the GfG/PtG units in the service restoration process by obtaining the difference between their scheduled set points with and without the service restoration signal. $\mathbb{T}^{\mathbb{H}*}$ represents the set of historical time steps for the scheduling of PtG, GfG, and storage facilities; and t^h expresses the historical values of the system variables and parameters. In order to calculate the total service restoration profit, the proposed algorithm considers the customer interruption cost (CIC) based on the method given in [78]. Accordingly, (5.28) represents the total profit resulted from service restoration contribution for the PtG/GfG operator:

$$Pr^{SR,CIC}_{u,t} = E^{Prc}_t.\big(P^{GfG,SR}_{u,t} + P^{PtG,SR}_{u,t}\big)+\big(CIC^{rate}/P^{SR}_{u,t}\big).\big(P^{GfG,SR}_{u,t} + P^{PtG,SR}_{u,t}\big)$$
$$\forall t \in \mathbb{T} \wedge \forall u \in \mathbb{U} \tag{5.28}$$

5.2 Case Studies for the Proposed MCES Algorthim

Figure 5.2 shows the 33–bus power distribution system integrated with the natural gas distribution grid that is used as the test system for the simulation results. The

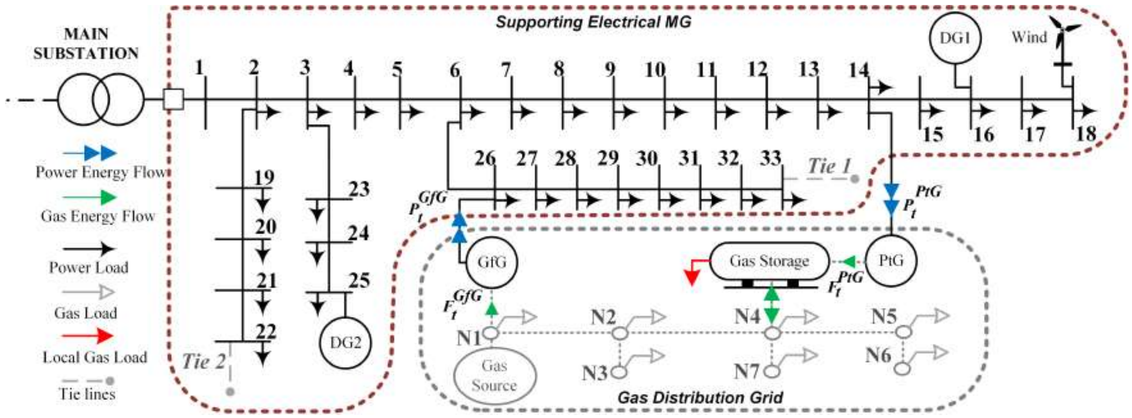

Figure 5.2: 33-bus power distribution system integrated with the renewable DG, gas storage, and natural gas distribution grid via GfG and PtG facilities

system is assumed to be a supporting microgrid that receives a participation signal from the supported microgrids. The system includes renewable DG at Bus 18, GfG unit at Bus 26 and PtG unit at Bus 14 with a gas storage. The gas storage is connected to Node 4 in the gas system which allows a bidirectional gas flow in addition to supplying its local load. All buses in the distribution grid and the nodes in the gas grid are loaded. The historical electricity price data from Ontario's electricity market are adopted for the numerical studies for a typical year [134]. The gas price is set as a flat rate of 0.174 $\$/m^3$ as per the real–world price data. The modeling and simulation parameters of the proposed system are listed in Table 5.14, where the operational parameters of the GfG and PtG units are adopted from [135]. The load demand profile for the electrical distribution system is modeled

Table 5.14: Modeling and Simulation Parameters.

$\eta^{GfG} = 60\%$	$C^{GfG} = 70\% \times HMC/P^{GfG}_{max}$
$\eta^{PtG} = 80\%$	$C^{PtG} = 30\% \times HMC/(P^{PtG}_{max} \times \eta^{PtG})$
$P^{GfG}_{i,min} = 0$ (MW)	$P^{Brn}_{j,min} = 0$ (MW) $\forall j \in \mathbb{B}$
$P^{GfG}_{i,max} = 2.5$ (MW)	$P^{Brn}_{j,max} = 3.5$ (MW) $\forall j = \{1, 2, ..., 6\}$
$F^{PtG}_{i,min} = 0$ (m^3/h)	$P^{Brn}_{j,max} = 1.5$ (MW) $\forall j = \{7, 8, ..., 33\}$
$F^{PtG}_{i,max} = 113.676$ (m^3/h)	$\lambda^{GfG} = 94.73$ (MWh/m^3)
$Pr^{Nod}_{l,min} = 900$ (kPa)	$\lambda^{PtG} = 1/94.73$ (m^3/MWh)
$Pr^{Nod}_{l,max} = 1000$ (kPa)	$V^{Bus}_{i,min} = 0.95$ (pu)
$F^{Dhg}_{min} = 0$ (m^3/h)	$V^{Bus}_{i,max} = 1.05$ (pu)
$F^{Dhg}_{max} = 125$ (m^3/h)	$F^{Pip}_{k,min} = 0$ (m^3/h)
$LOG^{G}_{min} = 15$ (m^3)	$F^{Pip}_{k,max} = 1000$ (m^3/h)
$LOG^{G}_{max} = 300$ (m^3)	$P^{PtG}_{min} = 0$ (MW)
$LOG^{G}_{Res} = 115$ (m^3)	$P^{PtG}_{max} = 1.5$ (MW)

based on real data obtained from [136]. Figure 5.3 shows various load profiles for one day in a year.

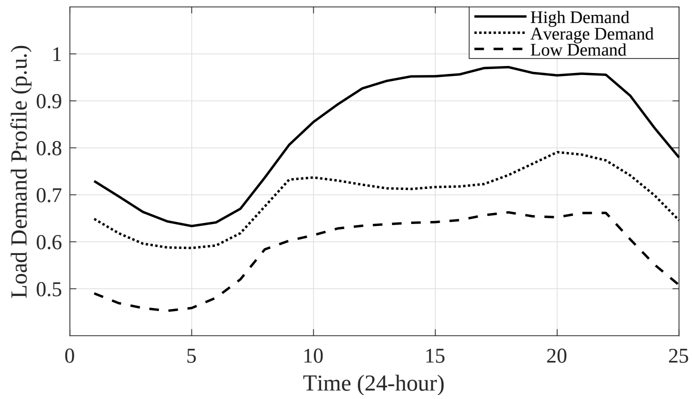

Figure 5.3: Different load demand profiles for 24 hours in one year.

The optimization horizon for simulation is set to 24 hours. Three case studies are presented in this section. The response of the proposed model in case of receiving a restoration signal from the neighboring microgrid is given in the first case study. In the second case study, a gas network outage is assumed to occur in the presence of a gas storage connected to a local gas load. In the third case study, participation of the PtG/GfG units in the real–time market is assessed.

5.2.1 Restoration Services to the Neighboring Microgrid

It is assumed that two open–tie lines (Tie 1 and Tie 2) are connected to the electrical grid in Fig 5.2, where the installed tie–lines represent optional paths to neighboring microgrid; in this case study, it is assumed that Tie 1 is a path for transferring power to a supported microgrid. microgrid is assumed to require support in contingency situations. Hence, the service restoration signal is assumed to be received through Tie 1 from a neighbor faulted microgrid. Two studies are considered in this case as follows:

1. Service restoration signal is received while market prices are lower than the maximum threshold for PtG unit operation.
2. Service restoration signal is received while market prices are higher than the minimum threshold for GfG unit operation.

The maximum threshold is defined here as the level of market prices above which the PtG unit stops operating, whereas the minimum threshold is defined as the level below which the GfG unit does not operate.

5.2.1.1 Under Lower Electricity Market Prices

It is worth noting that when the service restoration signal is received (i.e., M^{SR}=1), the penalty factor $\beta_{u,t}^{SR}$ is set to a very large positive value which forces the PtG/GfG units to participate in the restoration process. The operation of the PtG and GfG units are altered from the arbitrage utilization mode to respond to the received service restoration signal. The simulation results are given in Fig 5.4. As shown in Fig 5.4 (d), the duration of the received restoration signal is assumed to be 6 hours with 2 MW ratings. The restoration signal is issued during lower electricity prices as

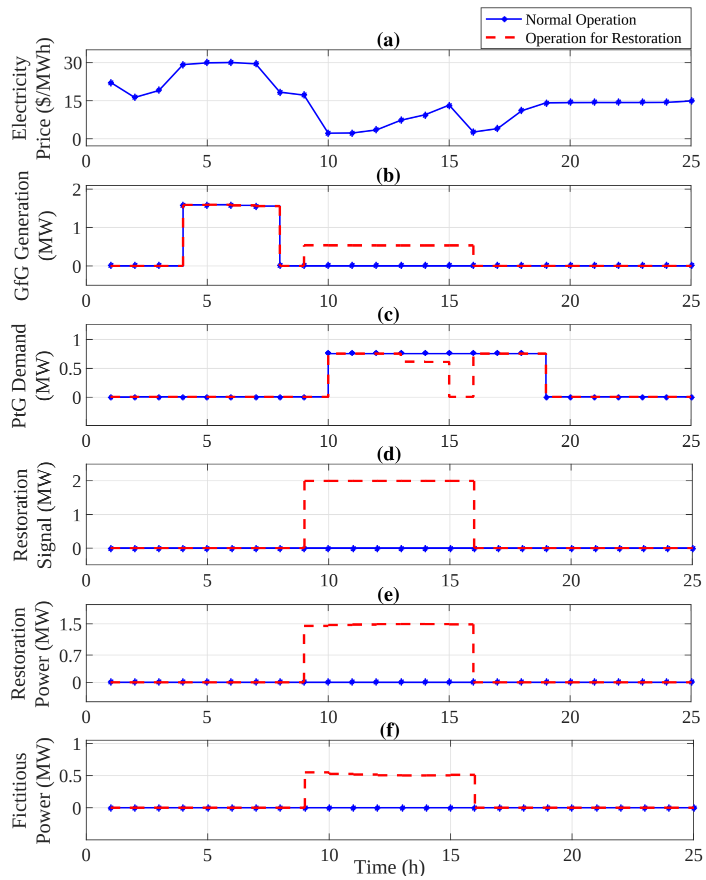

Figure 5.4: System operational parameters under first restoration scenario; (a) Electricity price, (b) Generation of the GfG unit, (c) Demand of the PtG unit, (d) Restoration signal, (e) Actual transferred power in response to the restoration signal, and (f) Restoration slack variable.

shown in Fig 5.4 (a). When the restoration signal is received, the GfG unit is forced to participate in the restoration process to the extent that its physical limitations are not violated as shown in Fig 5.4 (b). Considering the participation of the GfG unit, the maximum power $P^{R,RS}$ that can be sent to the neighboring microgrid is approximately equal to 1.5 MW without violating the operational constraints of the system. It is worth noting that Fig 5.4 (f) shows $P^{S,RS'}$ representing the difference between the received restoration signal (i.e. Fig 5.4 (d)) and the actual contribution power (i.e. Fig 5.4 (e)). In Fig 5.4 (c), the demand of the PtG unit is shown to be 0.75 MW under the normal mode of operation, while during the restoration signal the PtG demand varies due to restoration process. It can be noticed that in Hour 15, the energy cost starts increasing which causes the algorithm to participate in the restoration and reduce the gas demand to 0. This leads to an increase in the overall profit of the system.

5.2.1.2 Under Higher Electricity Market Prices

To assess the efficacy of the proposed model, another case study is considered where the restoration signal is assumed to be received when market prices are higher than the minimum requirement for GfG unit operation. Figure 5.5 shows the simulation results under this scenario. As shown in the figure, under the normal operation mode, the electricity price is high where the GfG unit ramps up its

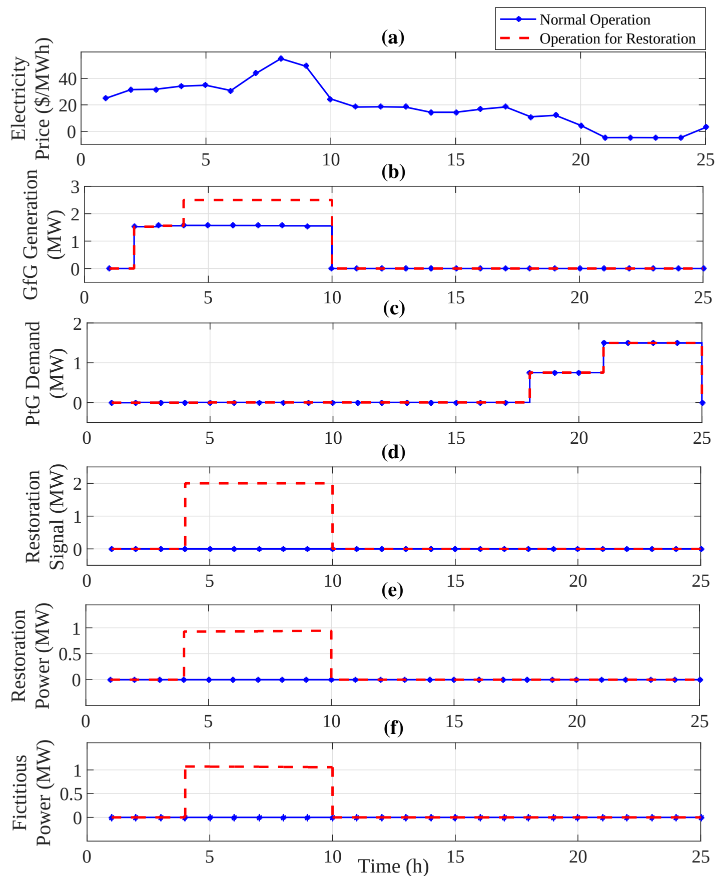

Figure 5.5: System operational parameters under second restoration scenario; (a) Electricity price, (b) Generation of the GfG unit, (c) Demand of the PtG unit, (d) Restoration signal, (e) Actual transferred power in response to the restoration signal, and (f) Restoration slack variable.

generation, and the PtG demand does not increase as it can be seen in Figs 5.5 (b) and (c). At Hour 17, the electricity price starts decreasing which causes an increase in the PtG demand as shown in Fig 5.5 (c). After receiving the restoration signal, the scheduling algorithm increases the generation of the GfG unit from its normal operation as it can be seen in Fig 5.5 (b) to satisfy the total participation to the restoration process. During this time period and based on the generation and demand of the power distribution grid, the maximum generation that can be supported for restoration process would be 1 MW as shown in Fig 5.5 (e); where the fictitious power is represented in Fig 5.5 (f).

5.2.2 Gas Grid Outages

In this case study, the proposed algorithm is assessed while there is an outage in the gas grid. It is assumed that the gas outage occurs from Hour 11 to 16 as shown in Fig 5.6 (a). Prior to the outage incident, the LOG of the gas storage is held at the reserve value of 115 m^3 as shown in Fig 5.6 (d). Due to the gas grid outage, the gas storage is scheduled to discharge with a constant rate until the LOG reaches to 15 m^3 at the end of outage event. The discharged capacity during the outage is shown in Fig 5.6 (c). The gas storage charging pattern can be seen from Fig 5.6 (b), where the PtG unit operates to fill in the storage reservoir up to its reserved capacity. After the outage event ends, the gas storage keeps charging for one hour,

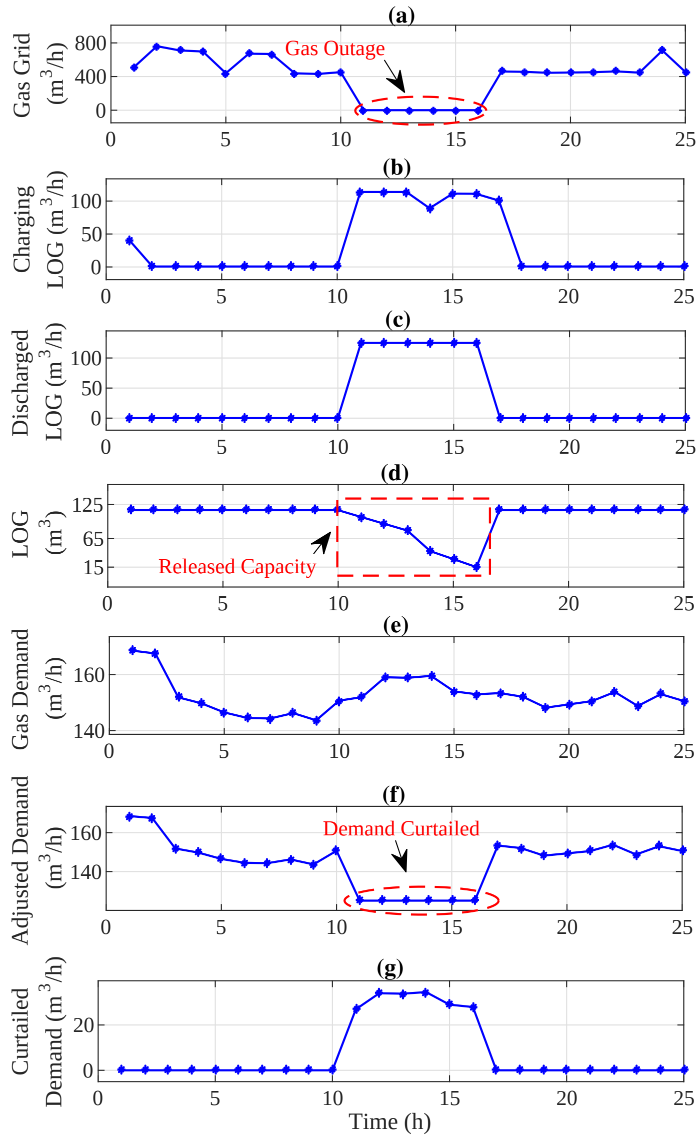

Figure 5.6: Gas system operational parameters during the gas grid outage; (a) Total gas grid demand during the outage, (b) Charging from the PtG unit, (c) Discharging to the local gas load, (d) LOG, (e) Local gas load demand, (f) Actual gas transferred to the local load, and (g) Curtailed gas local load.

so that the LOG can reach to its reserved limit again. As shown in Fig 5.6 (e), the local gas demand varies from 152 m^3/h to 159 m^3/h during the outage event, which is supplied by the gas storage. Since there is not enough gas to supply the load in full during the outage, a portion of the demand is curtailed as shown in Fig 5.6 (f). Accordingly, the adjusted gas demand would be lower than the original value (i.e., set to 125 m^3/h by the optimization problem) as shown in Fig 5.6 (g).

5.2.3 Contribution to Real–time Market

In this section, the behavior of the proposed algorithm for participation in the real–time market is assessed. The real–time signal is sent by the grid operator to PtG and GfG units to maintain the operational requirements of the electrical distribution grid. Figure 5.7 shows the operation of the facilities for arbitrage utilization under the normal condition. In addition, the received real–time signal is shown in Figs 5.7 (a) and (c), assumed to equal 1 MW charging and discharging. The real–time signal represents that higher generation by the GfG is needed to meet the power demand as shown in Fig 5.7 (b). In addition, Fig 5.7 (d) shows that the PtG demand has been adjusted in response to the real–time signal.

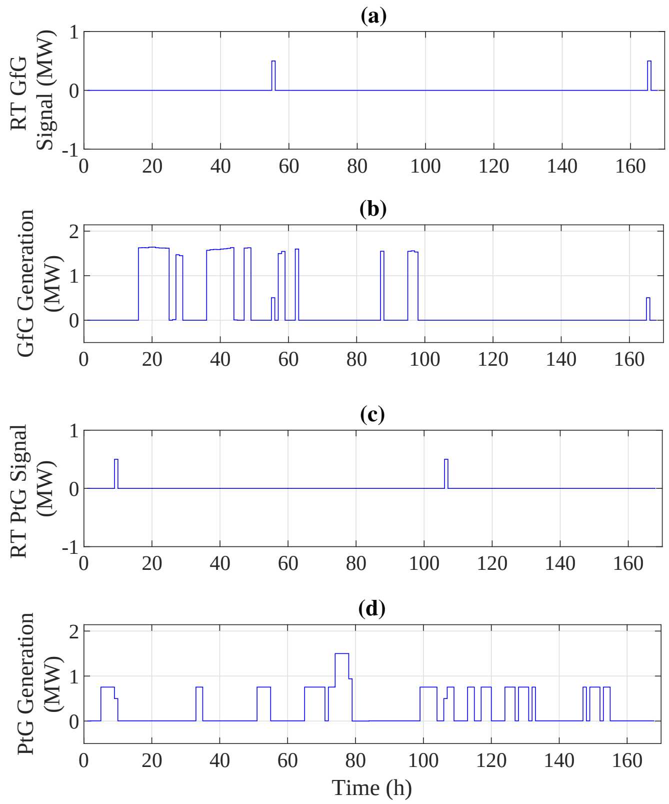

Figure 5.7: Operating results in response to the real–time signal; (a) Received real–time signal for the GfG unit, (b) Generation of the GfG unit, (c) Received real–time signal for the PtG unit, and (d) Demand response of the PtG unit.

5.2.4 System Revenue and Contribution Indices

The simulation is executed for a year for computation of the annual revenue. Figure 5.8 shows the total revenue in USD$ on a monthly basis under various cases. The model is operated for the following services: (i) arbitrage, (ii) arbitrage with real–

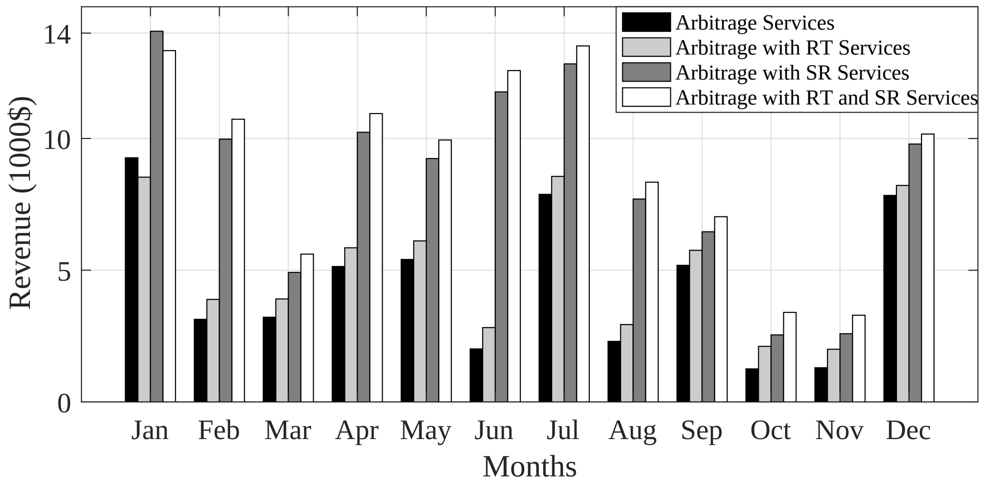

Figure 5.8: Monthly system revenue under various scenarios

time service, (iii) arbitrage with service restoration service, and (iv) arbitrage with real–time and service restoration services. It can be seen in the figure that participation in the real–time market slightly increases the system revenue, while adding service restoration services considerably enhances the total revenue. Furthermore, the impact of penalty factor values on the operation of the model is investigated using the proposed indices in Section 5.1.2. Figure 5.9 shows the trend of the SRCI values versus the penalty factor. Under the higher market price case, a change in the penalty factor $\beta_{u,t}^{SR}$ does not impact the response of the system towards the service restoration process since the system already generates maximum power for arbitrage utilization. Under the lower electricity price case, however, it can be noticed that the selection of $\beta_{u,t}^{SR}$ affects the contribution percentage. The GfG unit

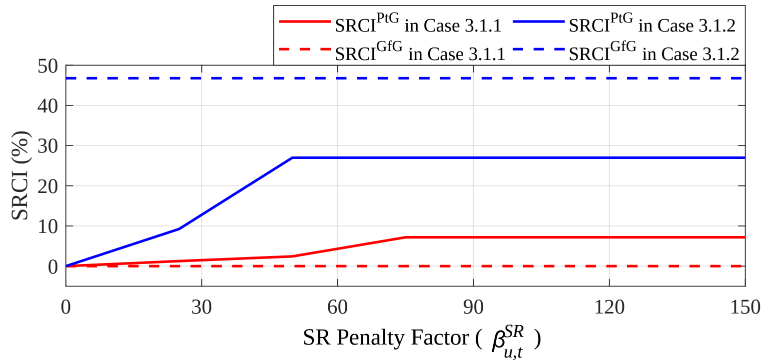

Figure 5.9: System restoration contribution index

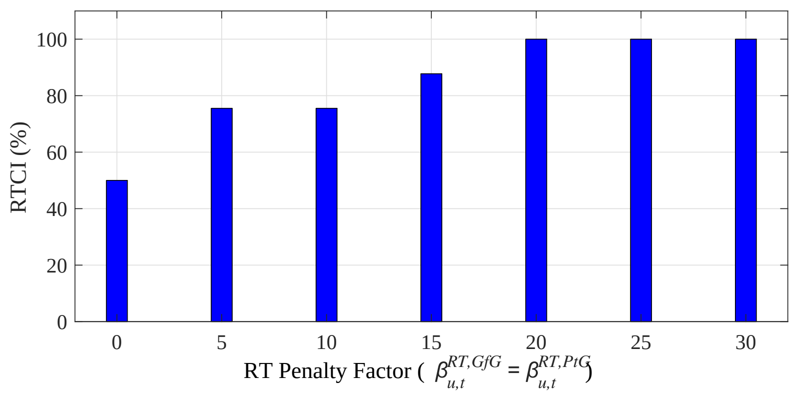

Figure 5.10: PtG and GfG real–time contribution index

reaches to its maximum contribution limit at $\beta_{u,t}^{SR} = 50$, while the PtG unit reaches to the maximum contribution at $\beta_{u,t}^{SR} = 75$. Fig 5.10 illustrates the trend of the real–time contribution versus the penalty factor. As shown in the figure, the larger the penalty factor is, the higher the contribution index becomes until it saturates at penalty factor of 20.

5.3 Summary of the Proposed Algorithm for Integrated Power and Natural Gas System

The proposed algorithm enables PtG and GfG units to provide several services to the integrated grid in addition to the price arbitrage exploitation. Such services include electrical and gas loads restoration in case of outages as well as ancillary service provision to local microgrids. Through numerical results from implementing the proposed algorithm on a test system, the efficiency of the proposed algorithm is evaluated. It is demonstrated that participation of PtG and GfG units in the aforementioned services using the proposed algorithm leads to a considerable increase in the system revenue. The results indicate that a higher return on investment can be generated for PtG and GfG units operators by adoption of the proposed model.

Chapter 6 - Conclusions and Future Work

6.1 Summary and Conclusions

The research in this thesis presents new optimization algorithms to address and mitigate different SDG challenges considering microgrids operating in both grid-connected and islanded modes. In particular, three main optimization models have been formulated in order to: enhance the performance of distributed state estimation algorithms of IMGs (chapter 2),automatic service restoration for SDGs clusteted into microgrids (chapters 3 and 4), and scheduling of bidirectional energy conversion units PtG and GfG in energy and ancillary services markets in multi–carrier energy systems (chapter 5).

In chapter 2, a new algorithm was presented for optimal zone clustering of droop–controlled IMGs based on the supply adequacy taking into account the dynamic performance of distributed state estimation units. In this regard, the IMG is partitioned into several localized, yet coupled zones, where each zone is responsible for its local state estimate and performs data fusion to reach consensus for shared state variables between zones by assigning a state estimator for each zone. The technique proposes a novel algorithm to optimally define the placement of the virtual boundaries of the zones by minimizing the potential power transfer between adjacent zones. The proposed algorithm adopts the distributed particle filter technique for the state estimation process. The proposed algorithm also has the ability to come up with one optimal configuration considering different events and scenarios that might occur in IMGs. Monte Carlo simulations demonstrate the efficacy of the proposed technique in the presence of severely corrupted measurements and state values, as well as displaying tolerance to major load changes within the IMG. The distributed particle filter shows similar performance when compared to its centralized implementation while also providing computational savings by a factor of the number of zones. The simulation results show that proper zoning in an IMG considering different operating conditions and fault scenarios will result in a successful state estimation leading to an accurate identification of faulty conditions.

In chapter 3, a new model is introduced for optimum self–healing restoration in planned IMGs. The objective of the proposed algorithm is to optimize the topological structure of the IMG via: (1) maximizing the served load after the fault isolation; (2) minimizing the switching operation costs, and (3) minimizing the system losses. The problem is formulated as a multi-objective optimization problem and solved using Ant Colony Optimization algorithm. The formulated optimization model accounts for the special operational characteristics of droop controlled IMGs. The simulation results concluded that appropriate reconfiguration in conjunction with optimal settings of droop parameters between the DGs will improve the restoration process, while maintaining the system operational constraints. The above formulated problem has been extended in the same chapter to provide automatic back–feed service restoration in SDGs clustered into multi–microgrids that are capable of operating in both grid-connected and islanded modes of operation. The proposed restoration algorithm presented different layers of restoration process, based on the participating microgrids. The proposed restoration algorithm introduces three types of power transfer between the tied adjacent microgrids during the restoration process: load transfer, DG transfer, and a combination of load-/DG transfer. Another feature of the extended algorithm is the ability of forming a new, not planned, IMGs in the post–restoration network by utilizing the available DGs. Several case studies have been carried out on a typical distribution system with multiple microgrids to demonstrate the effectiveness and robustness of the proposed algorithm. The simulation results shows that the multiple layers of restoration process with consideration of different types of energy transfer and optimal droop settings in created IMG(s) will increase the chance to restore more unserved loads in addition to a reduction of the restoration cost.

In order to obviate the need for a central unit in the automatic back–feed service restoration, the optimization problem is reformulated in chapter 4, as a distributed constraint optimization problem, in which the variables and constraints are distributed among automated agents. To reduce the problem complexity, the restoration problem is decomposed into two sequential and interdependent distributed sub–problems: supply adequacy assessment, and optimal reconfiguration. The proposed algorithm adopts the optimal asynchronous partial overlay technique, which is based on the distributed constraint agent search to solve distributed sub–problems in a multi–agent environment. Each agent is assigned to a specific microgrid, where a mediation session is performed between the multi–agents to optimally perform the restoration process among them. Several case studies are simulated to test the convergence, performance, and effectiveness of the proposed algorithm under different operating conditions. The obtained simulation results show the effectiveness and robustness over the centralized restoration process.

The proliferation of bidirectional energy conversion units between power and natural gas systems is set the stage for a more integrated, resilient, and robust system. Chapter 5 shows how bidirectional energy conversion units and storage devices can be optimally scheduled within a MCES for provision of various regulation services to the grid operator. To that end, a new model is proposed for optimal scheduling of PtG, GfG, and gas storage units in a MCES. The model aims to facilitate integration of renewable energy resources, utilize gas and power price arbitrage, provide regulation services to the real–time market, and contribute to the system restoration between adjacent microgrids. Also, new indices that quantify the contribution of the MCES operator to real–time and ancillary service markets, are proposed. The proposed model is validated technically and economically by using a test system historical operating data. Numerical results demonstrate that not only the proposed model is technically feasible, but also it enhances the economic viability of the grid operator.

6.2 Contributions

The main contributions in this thesis can be highlighted as follows:

- Comparing the performance of centralized and distributed particle filters for dynamic state estimation of droop–controlled IMGs and analyzing the impacts of zone selection on the accuracy of distributed particle filter.

- Development of a multi–objective optimization model for the optimum zoning design of IMGs to enhance the performance of distributed particle filter under different operating conditions and reduce the power flow among adjacent zones (i.e., enhance the supply adequacy for each identified zone to be self-sufficient).

- Formulating a new optimization problem for automatic service restoration of planned IMGs considering the optimal settings of droop parameters for the disptachble DGs and solving the formulated problem using ACO.

- Introducing new mechanisms for back–feed automatic service restoration of SDGs clustred into microgrids via the introduction of new types of energy transfer between adjacent microgrids: load, DG, and a combination of load-/DG; in addition to the creation of new, not predefined, IMGs.

- Development of a new a multi–agent scheme for the automatic back–feed service restoration in SDGs. The proposed algorithm obviates the need for a central unit and reduces the restoration complexity problem by decomposing it to two sequential and interdependent distributed sub–problems: supply adequacy and optimal reconfiguration.

- Development of a new optimizing algorithm for the scheduling process of bidirectional energy conversion units PtG and GfG in integrated power and natural gas system in order to provide: energy shifting arbitrage, power service restoration, and gas service restoration. Also, new contribution indices have been proposed to measure the contribution of the energy conversion units to the real–time and service restoration.

6.3 Future Work

Building on the results and the proposed algorithms of this research work, the following summarizes some of the research points that can be carried out in the future:

- Investigate the vulnerability of SDGs and IMGs to cyber-physical attacks under both centralized and distributed control schemes
- Extending the developed optimization models for service restoration to consider both AC and DC microgrids
- Incorporating emerging technologies such as battery energy storage devices in the back–feeding restoration process.
- Extending the work in integrated power and natural gas to include electrified transportation systems (i.e., electric vehicles and charging stations)

Bibliography

[1] Y. A. R. I. Mohamed and E. F. El-Saadany, "Adaptive Decentralized Droop Controller to Preserve Power Sharing Stability of Paralleled Inverters in Distributed Generation Microgrids," IEEE Transactions on Power Electronics, vol. 23, no. 6, pp. 2806–2816, Nov. 2008.

[2] "IEEE Standard for Interconnecting Distributed Resources with Electric Power Systems," IEEE Std 1547-2003, pp. 1–28, Jul. 2003.

[3] I. El-Samahy and E. El-Saadany, "The effect of DG on power quality in a deregulated environment," in IEEE Power Engineering Society General Meeting, 2005, Jun. 2005, pp. 2969–2976 Vol. 3.

[4] G. Chicco, "Challenges for smart distribution systems: Data representation and optimization objectives," in 2010 12th International Conference on Optimization of Electrical and Electronic Equipment (OPTIM), May 2010, pp. 1236–1244.

[5] M. Ghofrani, A. Arabali, M. Etezadi-Amoli, and M. S. Fadali, "Energy storage application for performance enhancement of wind integration," IEEE Transactions on Power Systems, vol. 28, no. 4, pp. 4803–4811, Nov 2013.

[6] P. F. Ribeiro, B. K. Johnson, M. L. Crow, A. Arsoy, and Y. Liu, "Energy storage systems for advanced power applications," Proceedings of the IEEE, vol. 89, no. 12, pp. 1744–1756, Dec 2001.

[7] R. Hebner, J. Beno, and A. Walls, "Flywheel batteries come around again," IEEE Spectrum, vol. 39, no. 4, pp. 46–51, April 2002.

[8] S. Clegg and P. Mancarella, "Storing renewables in the gas network: modelling of power-to-gas seasonal storage flexibility in low-carbon power systems," IET Generation, Transmission Distribution, vol. 10, no. 3, pp. 566–575, 2016.

[9] M. Dewadasa, A. Ghosh, and G. Ledwich, “Islanded operation and system restoration with converter interfaced distributed generation,” in Innovative Smart Grid Technologies Asia (ISGT), 2011 IEEE PES, Nov. 2011, pp. 1–8.

[10] S. P. Chowdhury, S. Chowdhury, and P. A. Crossley, “Islanding protection of active distribution networks with renewable distributed generators: A comprehensive survey,” Electric Power Systems Research, vol. 79, no. 6, pp. 984–992, Jun. 2009.

[11] EPRI, “Overview of advanced distribution automation implementation in North America,” France, Dec. 2008.

[12] P. C. Baker, S. D. J. McArthur, and M. Judd, “Data Management of On-Line Partial Discharge Monitoring Using Wireless Sensor Nodes Integrated with a Multi-Agent System,” in International Conference on Intelligent Systems Applications to Power Systems, 2007. ISAP 2007, Nov. 2007, pp. 1–6.

[13] “GRID 2030’—A national vision for electricity’s second 100 years,” 2003.

[14] “A vision for the smart grid,” 2009.

[15] S. A. Arefifar, Y. A. R. I. Mohamed, and T. H. M. EL-Fouly, “Comprehensive Operational Planning Framework for Self-Healing Control Actions in Smart Distribution Grids,” IEEE Transactions on Power Systems, vol. 28, no. 4, pp. 4192–4200, Nov. 2013.

[16] N. El Halabi, M. García-Gracia, J. Borroy, and J. Villa, “Current phase comparison pilot scheme for distributed generation networks protection,” Applied Energy, vol. 88, no. 12, pp. 4563–4569, Dec. 2011.

[17] M. Kezunovic, “Smart Fault Location for Smart Grids,” IEEE Transactions on Smart Grid, vol. 2, no. 1, pp. 11–22, Mar. 2011.

[18] “A vision for the modern grid,” Mar. 2007.

[19] H. Liu, X. Chen, K. Yu, and Y. Hou, “The Control and Analysis of Self-Healing Urban Power Grid,” IEEE Transactions on Smart Grid, vol. 3, no. 3, pp. 1119–1129, Sep. 2012.

[20] A. Zidan and E. F. El-Saadany, “A Cooperative Multiagent Framework for Self-Healing Mechanisms in Distribution Systems,” IEEE Transactions on Smart Grid, vol. 3, no. 3, pp. 1525–1539, Sep. 2012.

[21] M. A. Shahin, “Smart Grid self-healing implementation for underground distribution networks,” in 2013 IEEE Innovative Smart Grid Technologies-Asia (ISGT Asia), Nov. 2013, pp. 1–5.

[22] I. Dzafic, N. Lecek, and T. Donlagic, “Data exchange in self-healing applications for power distribution networks,” in 2012 IEEE Power and Energy Society General Meeting, Jul. 2012, pp. 1–7.

[23] A. Elmitwally, M. Elsaid, M. Elgamal, and Z. Chen, “A Fuzzy-Multiagent Self-Healing Scheme for a Distribution System With Distributed Generations,” IEEE Transactions on Power Systems, vol. 30, no. 5, pp. 2612–2622, Sep. 2015.

[24] I. H. Lim, T. S. Sidhu, M. S. Choi, S. J. Lee, S. Hong, S. I. Lim, and S. W. Lee, “Design and Implementation of Multiagent-Based Distributed Restoration System in DAS,” IEEE Transactions on Power Delivery, vol. 28, no. 2, pp. 585–593, Apr. 2013.

[25] D. A. Cartes and S. K. Srivastava, “Agent Applications and their Future in the Power Industry,” in IEEE Power Engineering Society General Meeting, 2007, Jun. 2007, pp. 1–6.

[26] W. Shahidehpour and Y. Wang, “Wiley: Communication and Control in Electric Power Systems: Applications of Parallel and Distributed Processing,” 2003. [Online]. Available: http://ca.wiley.com/WileyCDA/WileyTitle/productCd-0471453250.html

[27] “Microgrid Alliance Forms to Promote Tech,” May 2014.

[28] “IEEE Guide for Design, Operation, and Integration of Distributed Resource Island Systems with Electric Power Systems,” IEEE Std 1547.4-2011, pp. 1–54, Jul. 2011.

[29] N. Pogaku, M. Prodanovic, and T. C. Green, “Modeling, analysis and testing of autonomous operation of an inverter-based microgrid,” IEEE Transactions on Power Electronics, vol. 22, no. 2, pp. 613–625, March 2007.

[30] N. A. El-Taweel and H. E. Farag, “Voltage regulation in islanded microgrids using distributed constraint satisfaction,” IEEE Transactions on Smart Grid, vol. 9, pp. 1613–1625, May 2018.

[31] H. E. Farag, M. M. A. Abdelaziz, and E. F. El-Saadany, “Voltage and reactive power impacts on successful operation of islanded microgrids,” IEEE Transactions on Power Systems, vol. 28, no. 2, pp. 1716–1727, May 2013.

[32] H. Tebianian and B. Jeyasurya, "Dynamic state estimation in power systems: Modeling, and challenges," Electric Power Systems Research, vol. 121, pp. 109–114, Apr. 2015.

[33] R. Huang, R. Diao, Y. Li, J. Sanchez-Gasca, Z. Huang, B. Thomas, P. Etingov, S. Kincic, S. Wang, R. Fan, G. Matthews, D. Kosterev, S. Yang, and J. Zhao, "Calibrating parameters of power system stability models using advanced ensemble kalman filter," IEEE Transactions on Power Systems, vol. 33, no. 3, pp. 2895–2905, May 2018.

[34] H. E. Z. Farag, S. Saxena, and A. Asif, "A robust dynamic state estimation for droop controlled islanded microgrids," Electric Power Systems Research, vol. 140, pp. 445–455, Nov. 2016.

[35] A. Baiocco and S. D. Wolthusen, "Dynamic forced partitioning of robust hierarchical state estimators for power networks," in ISGT 2014, Feb 2014, pp. 1–5.

[36] A. Mohammadi and A. Asif, "Distributed particle filtering for large scale dynamical systems," in 2009 IEEE 13th International Multitopic Conference, Dec 2009, pp. 1–5.

[37] S. Choi and A. P. S. Meliopoulos, "Effective real-time operation and protection scheme of microgrids using distributed dynamic state estimation," IEEE Transactions on Power Delivery, vol. 32, no. 1, pp. 504–514, Feb 2017.

[38] L. Xie, D. Choi, S. Kar, and H. V. Poor, "Fully distributed state estimation for wide-area monitoring systems," IEEE Transactions on Smart Grid, vol. 3, no. 3, pp. 1154–1169, Sep. 2012.

[39] V. Kekatos and G. B. Giannakis, "Distributed robust power system state estimation," IEEE Transactions on Power Systems, vol. 28, no. 2, pp. 1617–1626, May 2013.

[40] S. Kar, G. Hug, J. Mohammadi, and J. M. F. Moura, "Distributed state estimation and energy management in smart grids: A consensus+innovations approach," IEEE Journal of Selected Topics in Signal Processing, vol. 8, no. 6, pp. 1022–1038, Dec 2014.

[41] N. Xia, H. B. Gooi, S. Chen, and W. Hu, "Decentralized state estimation for hybrid ac/dc microgrids," IEEE Systems Journal, vol. 12, no. 1, pp. 434–443, March 2018.

[42] M. Rostami and S. Lotfifard, "Distributed dynamic state estimation of power systems," IEEE Transactions on Industrial Informatics, vol. 14, no. 8, pp. 3395–3404, Aug 2018.

[43] J. Liu, A. Benigni, D. Obradovic, S. Hirche, and A. Monti, "State estimation and branch current learning using independent local kalman filter with virtual disturbance model," IEEE Transactions on Instrumentation and Measurement, vol. 60, no. 9, pp. 3026–3034, Sep. 2011.

[44] O. Vuković and G. Dán, "Security of fully distributed power system state estimation: Detection and mitigation of data integrity attacks," IEEE Journal on Selected Areas in Communications, vol. 32, no. 7, pp. 1500–1508, July 2014.

[45] H. E. Z. Farag and E. F. El-Saadany, "A novel cooperative protocol for distributed voltage control in active distribution systems," IEEE Transactions on Power Systems, vol. 28, no. 2, pp. 1645–1656, May 2013.

[46] S. A. Arefifar, Y. A. I. Mohamed, and T. El-Fouly, "Optimized multiple microgrid-based clustering of active distribution systems considering communication and control requirements," IEEE Transactions on Industrial Electronics, vol. 62, no. 2, pp. 711–723, Feb 2015.

[47] S. A. Arefifar and Y. A. I. Mohamed, "Dg mix, reactive sources and energy storage units for optimizing microgrid reliability and supply security," IEEE Transactions on Smart Grid, vol. 5, no. 4, pp. 1835–1844, July 2014.

[48] M. E. Nassar and M. M. A. Salama, "Adaptive self-adequate microgrids using dynamic boundaries," IEEE Transactions on Smart Grid, vol. 7, no. 1, pp. 105–113, Jan 2016.

[49] Q. Yang, J. Yang, W. Yu, D. An, N. Zhang, and W. Zhao, "On false data-injection attacks against power system state estimation: Modeling and countermeasures," IEEE Transactions on Parallel and Distributed Systems, vol. 25, no. 3, pp. 717–729, March 2014.

[50] M. Marzband, A. Sumper, A. Ruiz-Álvarez, J. L. Domínguez-García, and B. Tomoiagă, "Experimental evaluation of a real time energy management system for stand-alone microgrids in day-ahead markets," Applied Energy, vol. 106, pp. 365–376, Jun. 2013. [Online]. Available: http://www.sciencedirect.com/science/article/pii/S0306261913001268

[51] M. Stadler, G. Cardoso, S. Mashayekh, T. Forget, N. DeForest, A. Agarwal, and A. Schönbein, "Value streams in microgrids: A literature review," Applied Energy, vol. 162, pp. 980–989, Jan. 2016. [Online]. Available: http://www.sciencedirect.com/science/article/pii/S0306261915013082

[52] H. V. Wang, J. D. Loftis, Z. Liu, D. Forrest, and J. Zhang, "The advancement on the storm surge and street-level inundation modeling #x2014; A case study in New York City during Hurricane Sandy," in OCEANS 2014 - TAIPEI, Apr. 2014, pp. 1–8.

[53] S. Lissandron, A. Costabeber, and P. Mattavelli, "A generalized method to analyze the small-signal stability for a multi-inverter islanded grid with droop controllers," in 2013 15th European Conference on Power Electronics and Applications (EPE), Sep. 2013, pp. 1–10.

[54] J. Hare, X. Shi, S. Gupta, and A. Bazzi, "Fault diagnostics in smart micro-grids: A survey," Renewable and Sustainable Energy Reviews, vol. 60, pp. 1114–1124, Jul. 2016. [Online]. Available: http://www.sciencedirect.com/science/article/pii/S1364032116001775

[55] T. Ding, Y. Lin, Z. Bie, and C. Chen, "A resilient microgrid formation strategy for load restoration considering master-slave distributed generators and topology reconfiguration," Applied Energy, vol. 199, pp. 205–216, Aug. 2017. [Online]. Available: http://www.sciencedirect.com/science/article/pii/S0306261917305056

[56] M. Zaki El-Sharafy and H. E. Farag, "Self-healing restoration of smart micro-grids in islanded mode of operation," in Smart City 360°. Cham: Springer International Publishing, 2016, pp. 395–407.

[57] X. Feng, Y. Liang, and B. Guo, "A new islanding method for distributed generation and its application in power system restoration," in 2011 International Conference on Advanced Power System Automation and Protection (APAP), vol. 1, Oct. 2011, pp. 378–383.

[58] A. M. El-Zonkoly, "Renewable energy sources for complete optimal power system black-start restoration," Transmission Distribution IET Generation, vol. 9, no. 6, pp. 531–539, 2015.

[59] F. Cadini, G. L. Agliardi, and E. Zio, "A modeling and simulation framework for the reliability/availability assessment of a power transmission grid subject to cascading failures under extreme weather conditions," Applied

Energy, vol. 185, Part 1, pp. 267–279, Jan. 2017. [Online]. Available: http://www.sciencedirect.com/science/article/pii/S030626191631529X

[60] J. Z. Zhu, "Optimal reconfiguration of electrical distribution network using the refined genetic algorithm," Electric Power Systems Research, vol. 62, no. 1, pp. 37–42, May 2002. [Online]. Available: http://www.sciencedirect.com/science/article/pii/S037877960200041X

[61] K. P. Detroja, "Optimal autonomous microgrid operation: A holistic view," Applied Energy, vol. 173, pp. 320–330, Jul. 2016. [Online]. Available: http://www.sciencedirect.com/science/article/pii/S030626191630513X

[62] S. A. Arefifar, Y. A. R. I. Mohamed, and T. H. M. EL-Fouly, "Comprehensive Operational Planning Framework for Self-Healing Control Actions in Smart Distribution Grids," IEEE Transactions on Power Systems, vol. 28, no. 4, pp. 4192–4200, Nov. 2013.

[63] A. Elmitwally, M. Elsaid, M. Elgamal, and Z. Chen, "A Fuzzy-Multiagent Self-Healing Scheme for a Distribution System With Distributed Generations," IEEE Transactions on Power Systems, vol. 30, no. 5, pp. 2612–2622, Sep. 2015.

[64] M.-S. Tsai and Y.-T. Pan, "Application of BDI-based intelligent multi-agent systems for distribution system service restoration planning," European Transactions on Electrical Power, vol. 21, no. 5, pp. 1783–1801, Jul. 2011. [Online]. Available: http://onlinelibrary.wiley.com/doi/10.1002/etep.542/abstract

[65] J. M. Solanki, S. Khushalani, and N. N. Schulz, "A Multi-Agent Solution to Distribution Systems Restoration," IEEE Transactions on Power Systems, vol. 22, no. 3, pp. 1026–1034, Aug. 2007.

[66] A. Zidan and E. F. El-Saadany, "A Cooperative Multiagent Framework for Self-Healing Mechanisms in Distribution Systems," IEEE Transactions on Smart Grid, vol. 3, no. 3, pp. 1525–1539, Sep. 2012.

[67] F. Ren, M. Zhang, and D. Sutanto, "A Multi-Agent Solution to Distribution System Management by Considering Distributed Generators," IEEE Transactions on Power Systems, vol. 28, no. 2, pp. 1442–1451, May 2013.

[68] B. Li, R. Roche, and A. Miraoui, "Microgrid sizing with combined evolutionary algorithm and MILP unit commitment," Applied Energy, vol.

188, pp. 547–562, Feb. 2017. [Online]. Available: http://www.sciencedirect.com/science/article/pii/S0306261916318013

[69] M. Marzband, M. Ghadimi, A. Sumper, and J. L. Domínguez-García, "Experimental validation of a real-time energy management system using multi-period gravitational search algorithm for microgrids in islanded mode," Applied Energy, vol. 128, pp. 164–174, Sep. 2014. [Online]. Available: http://www.sciencedirect.com/science/article/pii/S0306261914004097

[70] G. Kyriakarakos, A. I. Dounis, S. Rozakis, K. G. Arvanitis, and G. Papadakis, "Polygeneration microgrids: A viable solution in remote areas for supplying power, potable water and hydrogen as transportation fuel," Applied Energy, vol. 88, no. 12, pp. 4517–4526, Dec. 2011. [Online]. Available: http://www.sciencedirect.com/science/article/pii/S0306261911003333

[71] Y. Xu and W. Liu, "Novel Multiagent Based Load Restoration Algorithm for Microgrids," IEEE Transactions on Smart Grid, vol. 2, no. 1, pp. 152–161, Mar. 2011.

[72] H. Li, H. Sun, J. Wen, S. Cheng, and H. He, "A Fully Decentralized Multi-Agent System for Intelligent Restoration of Power Distribution Network Incorporating Distributed Generations [Application Notes]," IEEE Computational Intelligence Magazine, vol. 7, no. 4, pp. 66–76, Nov. 2012.

[73] Z. Wang and J. Wang, "Self-Healing Resilient Distribution Systems Based on Sectionalization Into Microgrids," IEEE Transactions on Power Systems, vol. 30, no. 6, pp. 3139–3149, Nov. 2015.

[74] A. Sharma, D. Srinivasan, and A. Trivedi, "A Decentralized Multiagent System Approach for Service Restoration Using DG Islanding," IEEE Transactions on Smart Grid, vol. 6, no. 6, pp. 2784–2793, Nov. 2015.

[75] C. Chen, J. Wang, F. Qiu, and D. Zhao, "Resilient Distribution System by Microgrids Formation After Natural Disasters," IEEE Transactions on Smart Grid, vol. 7, no. 2, pp. 958–966, Mar. 2016.

[76] M. Ahmadigorji and N. Amjady, "Optimal dynamic expansion planning of distribution systems considering non-renewable distributed generation using a new heuristic double-stage optimization solution approach," Applied Energy, vol. 156, pp. 655–665, Oct. 2015. [Online]. Available: http://www.sciencedirect.com/science/article/pii/S0306261915008715

[77] N. A. El-Taweel and H. E. Z. Farag, "A distributed constraint satisfaction approach for reactive power sharing in microgrids," Electric Power Systems Research, vol. 147, pp. 42–54, Jun. 2017. [Online]. Available: http://www.sciencedirect.com/science/article/pii/S0378779617300639

[78] M. Z. El-Sharafy and H. E. Z. Farag, "Back-feed power restoration using distributed constraint optimization in smart distribution grids clustered into microgrids," Applied Energy, vol. 206, pp. 1102 – 1117, 2017.

[79] Y. Lin and Z. Bie, "Study on the resilience of the integrated energy system," Energy Procedia, vol. 103, pp. 171 – 176, 2016, renewable Energy Integration with Mini/Microgrid – Proceedings of REM2016.

[80] S. Clegg and P. Mancarella, "Storing renewables in the gas network: modelling of power-to-gas seasonal storage flexibility in low-carbon power systems," IET Generation, Transmission Distribution, vol. 10, no. 3, pp. 566–575, 2016.

[81] J. Devlin, K. Li, P. Higgins, and A. Foley, "The importance of gas infrastructure in power systems with high wind power penetrations," Applied Energy, vol. 167, pp. 294 – 304, 2016.

[82] E. Pursiheimo, H. Holttinen, and T. Koljonen, "Path toward 100 renewable energy future and feasibility of power-to-gas technology in nordic countries," IET Renewable Power Generation, vol. 11, no. 13, pp. 1695–1706, 2017.

[83] H. Khani, N. El-Taweel, and H. E. Z. Farag, "Power congestion management in integrated electricity and gas distribution grids," IEEE Systems Journal, pp. 1–12, 2018.

[84] Y. Liu, Y. Su, Y. Xiang, J. Liu, L. Wang, and W. Xu, "Operational reliability assessment for gas-electric integrated distribution feeders," IEEE Transactions on Smart Grid, vol. 10, no. 1, pp. 1091–1100, Jan 2019.

[85] G. Venkataramanan and C. Marnay, "A larger role for microgrids," IEEE Power and Energy Magazine, vol. 6, no. 3, pp. 78–82, May 2008.

[86] C. Marnay, G. Venkataramanan, M. Stadler, A. S. Siddiqui, R. Firestone, and B. Chandran, "Optimal Technology Selection and Operation of Commercial-Building Microgrids," IEEE Transactions on Power Systems, vol. 23, no. 3, pp. 975–982, Aug. 2008.

[87] M. M. A. Abdelaziz, H. E. Farag, E. F. El-Saadany, and Y. A. I. Mohamed, "A novel and generalized three-phase power flow algorithm for islanded microgrids using a newton trust region method," IEEE Transactions on Power Systems, vol. 28, no. 1, pp. 190–201, 2013.

[88] R. Huang, R. Diao, Y. Li, J. Sanchez-Gasca, Z. Huang, B. Thomas, P. Etingov, S. Kincic, S. Wang, R. Fan, G. Matthews, D. Kosterev, S. Yang, and J. Zhao, "Calibrating parameters of power system stability models using advanced ensemble kalman filter," IEEE Transactions on Power Systems, vol. 33, no. 3, pp. 2895–2905, May 2018.

[89] H. E. Z. Farag, S. Saxena, and A. Asif, "A robust dynamic state estimation for droop controlled islanded microgrids," Electric Power Systems Research, vol. 140, pp. 445–455, Nov. 2016.

[90] "Synchronized Phasor Measurements and Their Applications | A.G. Phadke | Springer." [Online]. Available: https://www.springer.com/la/book/9781441945631

[91] S. Saxena, A. Asif, and H. Farag, "Nonlinear, reduced order, distributed state estimation in microgrids," in 2015 IEEE International Conference on Acoustics, Speech and Signal Processing (ICASSP), April 2015, pp. 2874–2878.

[92] M. M. A. Abdelaziz and E. F. El-Saadany, "Maximum loadability consideration in droop-controlled islanded microgrids optimal power flow," Electric Power Systems Research, vol. 106, pp. 168 – 179, 2014.

[93] P. Malysz, S. Sirouspour, and A. Emadi, "An optimal energy storage control strategy for grid-connected microgrids," IEEE Transactions on Smart Grid, vol. 5, no. 4, pp. 1785–1796, July 2014.

[94] A. Mohammadi and A. Asif, "Distributed particle filter implementation with intermittent/irregular consensus convergence," IEEE Transactions on Signal Processing, vol. 61, no. 10, pp. 2572–2587, May 2013.

[95] B. G. Sileshi, C. Ferrer, and J. Oliver, "Particle filters and resampling techniques: Importance in computational complexity analysis," in 2013 Conference on Design and Architectures for Signal and Image Processing, Oct 2013, pp. 319–325.

[96] R. Karlsson, T. Schon, and F. Gustafsson, "Complexity analysis of the marginalized particle filter," IEEE Transactions on Signal Processing, vol. 53, no. 11, pp. 4408–4411, Nov 2005.

[97] C. Murphy and A. Keane, "Local and remote estimations using fitted polynomials in distribution systems," IEEE Transactions on Power Systems, vol. 32, no. 4, pp. 3185–3194, July 2017.

[98] H. Khazraj, F. F. da Silva, C. L. Bak, and U. Annakkage, "Addressing single and multiple bad data in the modern pmu-based power system state estimation," in 2017 52nd International Universities Power Engineering Conference (UPEC), Aug 2017, pp. 1–6.

[99] M. E. Nassar and M. M. A. Salama, "Adaptive self-adequate microgrids using dynamic boundaries," IEEE Transactions on Smart Grid, vol. 7, no. 1, pp. 105–113, Jan 2016.

[100] S. Babu, P. Hilber, E. Shayesteh, and L. E. Enarsson, "Reliability evaluation of distribution structures considering the presence of false trips," IEEE Transactions on Smart Grid, vol. 9, no. 3, pp. 2268–2275, May 2018.

[101] T. Ding, Y. Lin, Z. Bie, and C. Chen, "A resilient microgrid formation strategy for load restoration considering master-slave distributed generators and topology reconfiguration," Applied Energy, vol. 199, pp. 205 – 216, 2017.

[102] T. J. Hammons, "Artificial intelligence in power system engineering: Actual and potential applications of expert systems, knowledge-based systems, and artifical neural networks," IEEE Power Engineering Review, vol. 14, no. 2, pp. 11–, February 1994.

[103] W. P. Luan, M. R. Irving, and J. S. Daniel, "Genetic algorithm for supply restoration and optimal load shedding in power system distribution networks," IEE Proceedings - Generation, Transmission and Distribution, vol. 149, no. 2, pp. 145–151, March 2002.

[104] N. A. Fountas, N. D. Hatziargyriou, and K. P. Valavanis, "Hierarchical time-extended petri nets as a generic tool for power system restoration," IEEE Transactions on Power Systems, vol. 12, no. 2, pp. 837–843, May 1997.

[105] Y. Liu and X. Gu, "Skeleton-network reconfiguration based on topological characteristics of scale-free networks and discrete particle swarm optimization," IEEE Transactions on Power Systems, vol. 22, no. 3, pp. 1267–1274, Aug 2007.

[106] D. S. Popovic and Z. N. Popovic, “A risk management procedure for supply restoration in distribution networks,” IEEE Transactions on Power Systems, vol. 19, no. 1, pp. 221–228, Feb 2004.

[107] L. Ke, C. Archetti, and Z. Feng, “Ants can solve the team orienteering problem,” Computers and Industrial Engineering, vol. 54, no. 3, pp. 648 – 665, 2008.

[108] H. Falaghi, M. Haghifam, and C. Singh, “Ant colony optimization-based method for placement of sectionalizing switches in distribution networks using a fuzzy multiobjective approach,” IEEE Transactions on Power Delivery, vol. 24, no. 1, pp. 268–276, Jan 2009.

[109] F. Romero, P. H. Baumann, T. Milagres Miranda, D. Takahata, A. Uehara Antunes, . C. L. Alves, S. L. P. D. C. Valinho, and L. M. Azevedo, “Service prioritisation and crew dispatch in an electricity utility,” CIRED - Open Access Proceedings Journal, vol. 2017, no. 1, pp. 1454–1458, 2017.

[110] W. Deng, J. Xu, and H. Zhao, “An improved ant colony optimization algorithm based on hybrid strategies for scheduling problem,” IEEE Access, vol. 7, pp. 20 281–20 292, 2019.

[111] Z. C. S. S. Hlaing and M. A. Khine, “Solving Traveling Salesman Problem by Using Improved Ant Colony Optimization Algorithm,” International Journal of Information and Education Technology, pp. 404–409, 2011. [Online]. Available: http://www.ijiet.org/index.php?m=content&c=index&a=show&catid=26&id=57

[112] F. Shariatzadeh, N. Kumar, and A. K. Srivastava, “Optimal control algorithms for reconfiguration of shipboard microgrid distribution system using intelligent techniques,” IEEE Transactions on Industry Applications, vol. 53, no. 1, pp. 474–482, Jan 2017.

[113] M. M. A. Abdelaziz, H. E. Farag, E. F. El-Saadany, and Y. A. R. I. Mohamed, “A Novel and Generalized Three-Phase Power Flow Algorithm for Islanded Microgrids Using a Newton Trust Region Method,” IEEE Transactions on Power Systems, vol. 28, no. 1, pp. 190–201, Feb. 2013.

[114] Y. Kumar, B. Das, and J. Sharma, “Multiobjective, Multiconstraint Service Restoration of Electric Power Distribution System With Priority Customers,” IEEE Transactions on Power Delivery, vol. 23, no. 1, pp. 261–270, Jan. 2008.

[115] F. Mekic, Z. Wang, V. Donde, F. Yang, and J. Stoupis, "Disributed automation for back-feed network power restoration," in 20th International Conference and Exhibition on Electricity Distribution - Part 1, 2009. CIRED 2009, Jun. 2009, pp. 1–5.

[116] J. Stoupis, Z. Wang, F. Yang, V. Donde, F. Mekic, and W. Peterson, "Restoring confidence (Control-center- and field-based feeder restoration)," Mar. 2009. [Online]. Available: https://library.e.abb.com/public/90c72e45cc02eb3dc125762d0046bcec/17-22%203M984_ENG72dpi.pdf

[117] M. Z. El-Sharafy and H. E. Farag, "Automatic restoration in distribution systems considering DG transfer and islanded microgrids," in 2016 IEEE Electrical Power and Energy Conference (EPEC), Oct. 2016, pp. 1–6.

[118] C. Li, J. Savulak, and R. Reinmuller, "Unintentional Islanding of Distributed Generation #x2014;Operating Experiences From Naturally Occurred Events," IEEE Transactions on Power Delivery, vol. 29, no. 1, pp. 269–274, Feb. 2014.

[119] D. Das, "Reconfiguration of distribution system using fuzzy multi-objective approach," International Journal of Electrical Power & Energy Systems, vol. 28, no. 5, pp. 331–338, Jun. 2006. [Online]. Available: http://www.sciencedirect.com/science/article/pii/S0142061506000184

[120] N. El-Taweel and H. E. Z. Farag, "Voltage Regulation in Islanded Microgrids Using Distributed Constraint Satisfaction," IEEE Transactions on Smart Grid, vol. PP, no. 99, pp. 1–1, 2016.

[121] H. E. Farag, E. F. El-Saadany, and R. Seethapathy, "A Two Ways Communication-Based Distributed Control for Voltage Regulation in Smart Distribution Feeders," IEEE Transactions on Smart Grid, vol. 3, no. 1, pp. 271–281, Mar. 2012.

[122] A. Zidan and E. F. El-Saadany, "Incorporating load variation and variable wind generation in service restoration plans for distribution systems," Energy, vol. 57, pp. 682–691, Aug. 2013. [Online]. Available: http://www.sciencedirect.com/science/article/pii/S0360544213004362

[123] G. B. Dantzig and P. Wolfe, "Decomposition Principle for Linear Programs," Operations Research, vol. 8, no. 1, pp. 101–111, Feb. 1960. [Online]. Available: http://pubsonline.informs.org/doi/abs/10.1287/opre.8.1.101

[124] A. Zidan and E. F. El-Saadany, "Incorporating customers' reliability requirements and interruption characteristics in service restoration plans for distribution systems," Energy, vol. 87, pp. 192–200, Jul. 2015. [Online]. Available: http://www.sciencedirect.com/science/article/pii/S0360544215005228

[125] I. K. Song, W. W. Jung, J. Y. Kim, S. Y. Yun, J. H. Choi, and S. J. Ahn, "Operation Schemes of Smart Distribution Networks With Distributed Energy Resources for Loss Reduction and Service Restoration," IEEE Transactions on Smart Grid, vol. 4, no. 1, pp. 367–374, Mar. 2013.

[126] "On multi-area control in electric power systems (PDF Download Available)," Jun. 2017. [Online]. Available: https://www.researchgate.net/publication/228407489_On_multi-area_control_in_electric_power_systems

[127] R. Mailler and V. Lesser, "Solving distributed constraint optimization problems using cooperative mediation," in Proceedings of the Third International Joint Conference on Autonomous Agents and Multiagent Systems, 2004. AAMAS 2004, Jul. 2004, pp. 438–445.

[128] V. R. Lesser and R. Mailler, "Asynchronous Partial Overlay: A New Algorithm for Solving Distributed Constraint Satisfaction Problems," arXiv:1109.6052 [cs], Sep. 2011. [Online]. Available: http://arxiv.org/abs/1109.6052

[129] "Reasoning about Rational Agents," Oct. 2016. [Online]. Available: https://mitpress.mit.edu/books/reasoning-about-rational-agents

[130] A. Petcu and B. Faltings, "MB-DPOP: A New Memory-bounded Algorithm for Distributed Optimization," in Proceedings of the 20th International Joint Conference on Artifical Intelligence. San Francisco, CA, USA: Morgan Kaufmann Publishers Inc., 2007, pp. 1452–1457. [Online]. Available: http://dl.acm.org/citation.cfm?id=1625275.1625510

[131] S. A. Arefifar, Y. A. R. I. Mohamed, and T. El-Fouly, "Optimized Multiple Microgrid-Based Clustering of Active Distribution Systems Considering Communication and Control Requirements," IEEE Transactions on Industrial Electronics, vol. 62, no. 2, pp. 711–723, Feb. 2015.

[132] M. E. Baran and I. M. El-Markabi, "A Multiagent-Based Dispatching Scheme for Distributed Generators for Voltage Support on Distribution Feeders," IEEE Transactions on Power Systems, vol. 22, no. 1, pp. 52–59, Feb. 2007.

[133] S. A. Yin and C. N. Lu, “Distribution Feeder Scheduling Considering Variable Load Profile and Outage Costs,” IEEE Transactions on Power Systems, vol. 24, no. 2, pp. 652–660, May 2009.

[134] “The ontario independent electricity system operator (ieso),” last accessed 25 March 2019. [Online]. Available: http://www.ieso.ca/power-data/price-overview/hourly-ontario-energy-price

[135] “The department of energy hydrogen and fuel cells program plan: ‘an integrated strategic plan for the research, development, and demonstration of hydrogen and fuel cell technologies’.” [Online]. Available: https://www.hydrogen.energy.gov/pdfs/program_plan2011.pdf

[136] “The ontario independent electricity system operator (ieso),” last accessed 25 March 2019. [Online]. Available: http://www.ieso.ca/power-data/demand-overview/historical-demand

Appendix - Figures and Data of the Distribution Test Systems

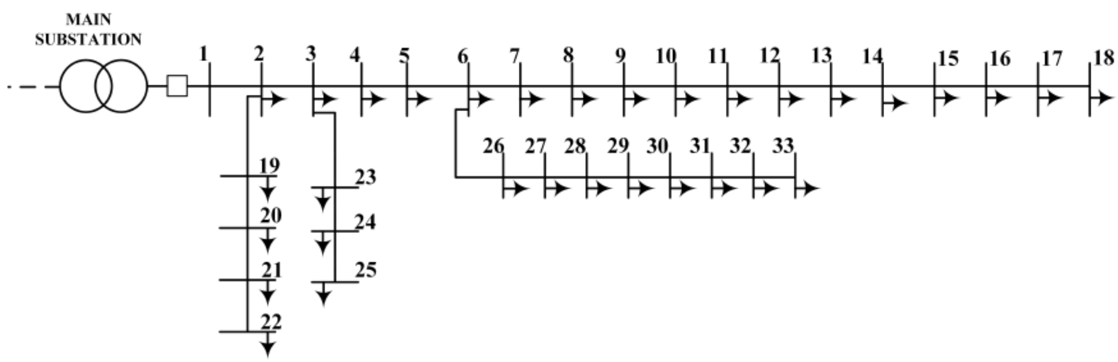

Figure 7.11: The 33-bus distribution test system.

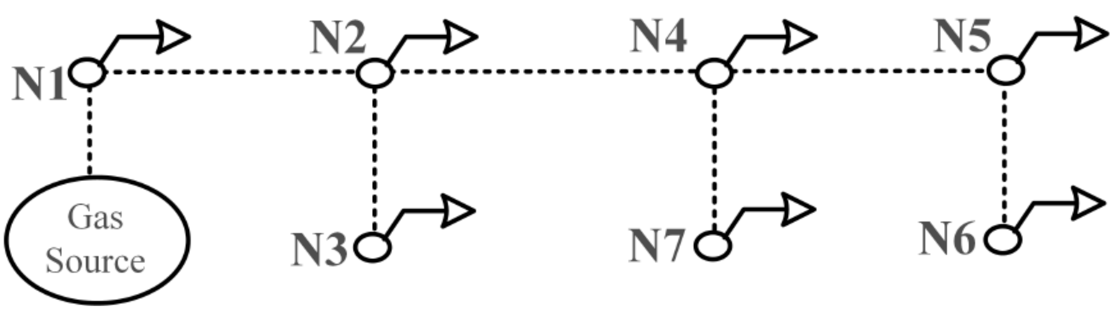

Figure 7.12: The 7-node gas distribution test system.

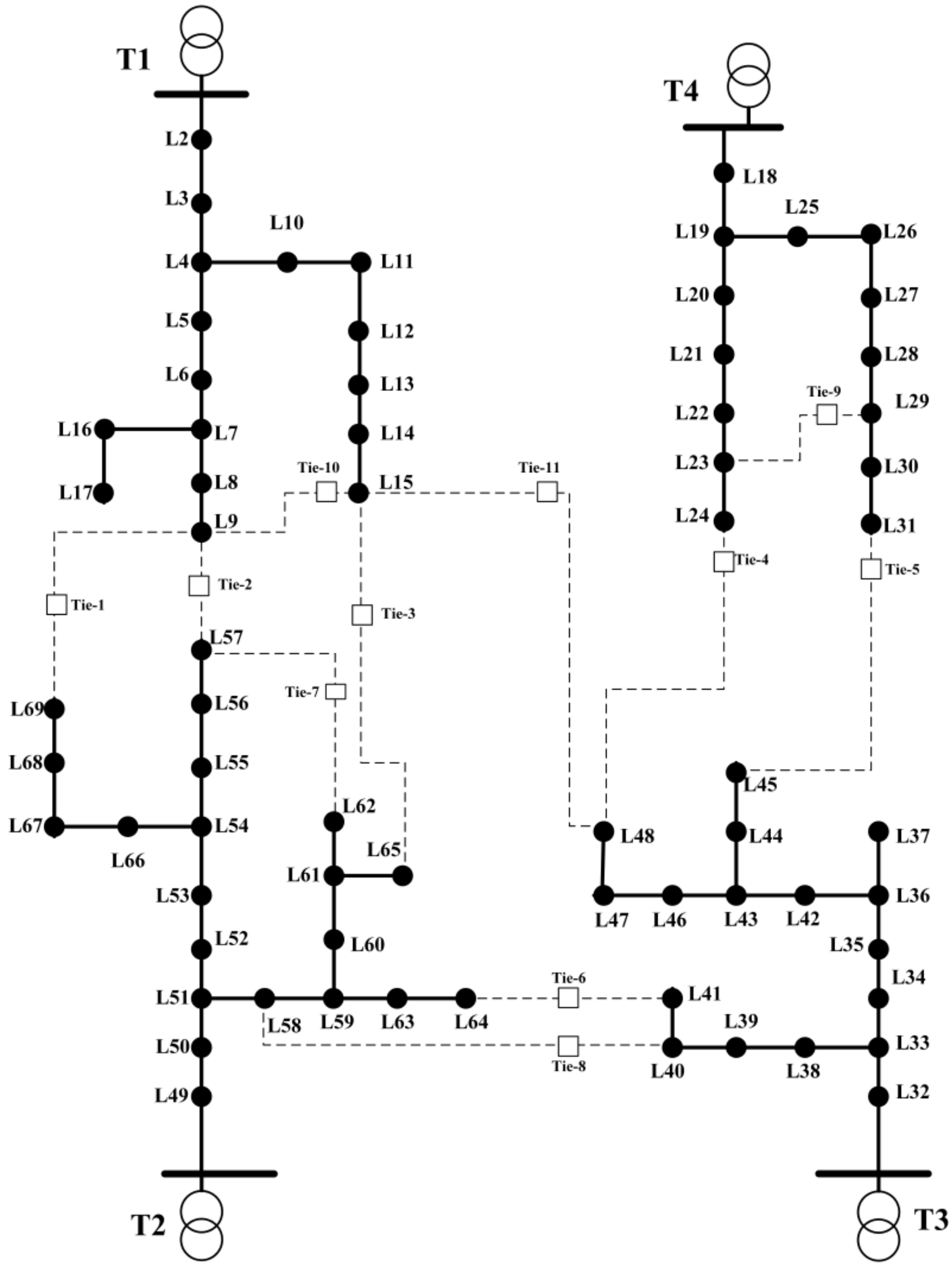

Figure 7.13: The 70-bus distribution test system.

Table 7.15: Loads and line data of the 33-bus distribution system

Branch #	From	To	R (p.u.)	X (p.u.)	PL (KW)To-node	QL (Kvar) To-node
1	1	2	0.00057	0.00029	0.1	0.06
2	2	3	0.00307	0.001564	0.09	0.04
3	3	4	0.002279	0.001161	0.12	0.08
4	4	5	0.002373	0.001209	0.06	0.03
5	5	6	0.0051	0.0044	0.06	0.02
6	6	7	0.001166	0.0038	0.2	0.1
7	7	8	0.00443	0.001464	0.2	0.1
8	8	9	0.006413	0.004608	0.06	0.02
9	9	10	0.06501	0.004608	0.06	0.02
10	10	11	0.001224	0.000405	0.045	0.03
11	11	12	0.002331	0.000771	0.06	0.035
12	12	13	0.009141	0.007192	0.06	0.035
13	13	14	0.003372	0.004439	0.12	0.08
14	14	15	0.0368	0.003275	0.06	0.01
15	15	16	0.004647	0.003394	0.06	0.02
16	16	17	0.008026	0.010716	0.06	0.02
17	17	18	0.004558	0.003574	0.09	0.04
18	2	19	0.001021	0.000974	0.09	0.04
19	19	20	0.009366	0.00844	0.09	0.04
20	20	21	0.00255	0.002979	0.09	0.04
21	21	22	0.004414	0.005836	0.09	0.04
22	3	23	0.002809	0.00192	0.09	0.05
23	23	24	0.005592	0.004415	0.42	0.2
24	24	25	0.005579	0.004366	0.42	0.2
25	6	26	0.001264	0.000644	0.06	0.025
26	26	27	0.00177	0.000901	0.06	0.025
27	27	28	0.006594	0.005814	0.06	0.02
28	28	29	0.005007	0.004362	0.12	0.07
29	29	30	0.00316	0.00161	0.2	0.6
30	30	31	0.006067	0.005996	0.15	0.07
31	31	32	0.001933	0.002253	0.21	0.1
32	32	33	0.002123	0.003301	0.06	0.04

Table 7.16: Loads and pipeline data of the 7-node gas distribution system

Pipeline #	From	To	Resistance (kPa.h/m^3)	Gas Demand To-node (m^3/h)
1	1	2	0.0003	10000
2	2	3	0.0004	12000
3	2	4	0	0
4	4	5	0.00025	20000
5	5	6	0.0002	16000
6	4	7	0.0003	0

Table 7.17: Loads and line data of the 70-node distribution system

Branch #	From	To	R (ohms)	X (ohms)	PL (KW)To-node	QL (Kvar) To-node
1	1	2	1.097	1.074	100	90
2	2	3	1.463	1.432	60	40
3	3	4	0.731	0.716	150	130
4	4	5	0.366	0.358	75	50
5	5	6	1.828	1.79	15	9
6	6	7	1.097	1.074	18	14
7	7	8	0.731	0.716	13	10
8	8	9	0.731	0.716	16	11
9	4	10	1.08	0.734	20	10
10	10	11	1.62	1.101	16	9
11	11	12	1.08	0.734	50	40
12	12	13	1.35	0.917	105	90
13	13	14	0.81	0.55	25	15
14	14	15	1.944	1.321	140	125
15	7	16	1.08	0.734	100	60
16	16	17	1.62	1.101	40	30
17	T4	18	1.097	1.074	60	30

Branch #	From	To	R (ohms)	X (ohms)	PL (KW) To-node	QL (Kvar) To-node
18	18	19	0.366	0.358	40	25
19	19	20	1.463	1.432	15	9
20	20	21	0.914	0.895	13	7
21	21	22	0.804	0.787	30	20
22	22	23	1.133	1.11	90	50
23	23	24	0.475	0.465	50	30
24	19	25	2.214	1.505	60	40
25	25	26	1.62	1.11	100	80
26	26	27	1.08	0.734	80	65
27	27	28	0.54	0.367	100	60
28	28	29	0.54	0.367	100	55
29	29	30	1.08	0.734	120	70
30	30	31	1.08	0.734	105	70
31	T3	32	0.366	0.358	60	40
32	32	33	1.463	1.432	20	11
33	33	34	1.463	1.432	80	60
34	34	35	0.914	0.895	36	24
35	35	36	1.097	1.074	130	120
36	36	37	1.097	1.074	43	30
37	33	38	0.27	0.183	80	50
38	38	39	0.27	0.183	240	120
39	39	40	0.81	0.55	125	110
40	40	41	1.296	0.881	125	110
41	36	42	1.188	0.807	10	5
42	42	43	1.188	0.807	150	130
43	43	44	0.81	0.55	50	30
44	44	45	1.62	1.101	30	20
45	43	46	1.08	0.734	130	120
46	46	47	0.54	0.367	150	130
47	47	48	1.08	0.734	25	15
48	T2	49	0.366	0.358	80	50
49	49	50	0.731	0.716	160	140
50	50	51	0.731	0.716	13	8
51	51	52	0.804	0.787	46	39

Branch #	From	To	R (ohms)	X (ohms)	PL (KW) To-node	QL (Kvar) To-node
52	52	53	1.17	1.145	150	130
53	53	54	0.768	0.752	40	28
54	54	55	0.731	0.716	60	40
55	55	56	1.097	1.074	40	30
56	56	57	1.463	1.432	30	25
57	51	58	1.08	0.734	150	100
58	58	59	0.54	0.367	60	35
59	59	60	1.08	0.734	120	70
60	60	61	1.836	1.248	90	60
61	61	62	1.296	0.881	18	10
62	59	63	1.188	0.807	16	10
63	63	64	0.54	0.367	100	50
64	61	65	1.08	0.734	60	40
65	54	66	0.54	0.367	90	70
66	66	67	1.08	0.734	85	55
67	67	68	1.08	0.734	100	70
68	68	69	1.08	0.734	140	90
69	9	69	0.908	0.726	—	—
70	9	57	0.381	0.244	—	—
71	15	65	0.681	0.544	—	—
72	24	48	0.254	0.203	—	—
73	31	45	0.254	0.203	—	—
74	64	41	0.254	0.203	—	—
75	57	62	0.454	0.363	—	—
76	58	40	0.454	0.363	—	—
77	23	29	0.454	0.363	—	—
78	9	15	0.681	0.544	—	—
79	15	48	0.454	0.363	—	—

Other Data: Current carrying capacity of all tie branches are 234.0 A. The current carrying capacity of branches 1-8, 17-23, 31-39 and 52-57 is 270 A. For branches 9 -16, 24-30, 40-51 and 58-68, it is 208 A. The ratings of the transformers of T1, T2, T3 and T4 are 2 MVA,2 MVA, 2.5 MVA and 2.5 MVA, respectively.